Impact of Tumor Microenvironment on Intratumor Distribution of Liposomes in Prostate Cancer

by

Ahmed Saad A. Alnaim

A dissertation submitted to the Graduate Faculty of
Auburn University
in partial fulfillment of the
requirements for the Degree of
Doctor of Philosophy

Auburn, Alabama
August 6, 2022

Keywords: Nanoparticles, Liposomes, Prostate Cancer, Tumor Microenvironment, Cancer-Associated Fibroblasts, Spheroids, Co-culture.

Approved by

Robert D. Arnold, Chair, Professor of Drug Discovery and Development
Jayachandra Babu Ramapuram, Professor of Drug Discovery and Development
Peter Panizzi, Professor of Drug Discovery and Development
Amit Kumar Mitra, Assistant Professor of Drug Discovery and Development
Allan David, Associate Professor of Chemical Engineering

Abstract

Extensive developments in nanocarrier formulations and their applications in cancer therapy have occurred in the last few decades. This improvement brought many FDA-approved liposome nanoparticles (LNPs) and other nanoparticle formulations. However, it has been established in many clinical studies that the efficacy of these LNPs has not met the expectations. This unsatisfactory outcome results from the poor correlation between existing *in vitro* 2D monolayer culture and that of preclinical and clinical "human" *in vivo* models. Solid tumors are made up of cancer cells with various stromal cells and factors that represent the tumor microenvironment (TME). The presence of fibroblasts, macrophages, and other stromal cells contributes to the poor distribution and efficacy of LNPs. Therefore, existing 2D models fail to recapitulate the architecture and complexity of tumor pathology and do not capture the challenges associated with the distribution and deposition of nanoparticles and their payloads. Our study uses metastatic castration-resistant prostate cancer (mCRPC) cells (PC3) that show neuroendocrine differentiation, which is associated with poor prognosis and survival. Accordingly, our goal was to develop a 3D multicellular platform that permits the examination of the impact of the TME on the performance of nanomedicines.

Furthermore, we hypothesize that stromal cells can alter the barrier properties within the TME and the distribution or uptake of LNPs, specifically cancer-associated fibroblasts (CAFs). To achieve that, we established a 3D model of prostate cancer with CAFs that allows visualization of drug distribution and uses flow cytometry to measure drug uptake. To examine the impact of TME, we developed model conventional and stealth liposomes similar to clinically approved formulations and stably entrap propidium

iodide over 72 hours under physiological conditions (37 ºC with serum). Moreover, we have demonstrated that free propidium iodide can be taken up by live cells with prolonged exposure (≥6 hours). In addition, we have determined the effect of CAFs on distribution and uptake between conventional and PEGylated liposomes in our 3D co-culture model using flow cytometry. We also acquired scanning fluorescence confocal microscopy images to confirm our findings in flow results and gain insights into the spatial distribution throughout different 3D co-cultures. We are using RNA-seq and immunoblotting to determine the effect of stromal cells, such as fibroblasts, on gene expression and protein changes in 3D spheroids. Preliminary data suggest that the inclusion of CAF results in genes associated with the malignant phenotype. In conclusion, insights into the interplay between LNPs and solid tumors and their microenvironment can be exploited to optimize and individualize the treatment of aggressive primary cancers and metastatic disease.

Acknowledgments

At this special moment, when I have reached the concluding stages of my Doctoral research and am ready to embark upon another voyage in my scientific career, I would like to take the opportunity to acknowledge the contributions of the people who have shaped my life and career.

First, I thank Allah for giving me the strength to overcome all the challenges, and for giving me the motivation to learn and acquire knowledge.

I am overwhelmed with my father and mother believing in me and supporting me to achieve this success. I am speechless and wordless to express my feeling toward my wife and kids that they never stop supporting me and encouraging me to achieve this success. My brothers and sisters and all my family, you have always been heartening and cheering me to achieve this success. I am grateful to all your prayers day and night, and I am hopeful to make you proud and delighted.

I would like to thank Dr. Robert Arnold, my adviser. I have learned a lot from him and am extremely thankful to him. He has helped me develop my scientific temper and inquisitive thinking. I appreciate his patience, motivation, and knowledge. I would like to express my sincere gratitude towards my committee members. Dr. Jay Ramapuram has given me invaluable suggestions and helpful guidance. I would like to thank Dr. Peter Panizzi for his continuous strong support, guidance, and continuous lighthearted attitude. Also, I would like to thank Dr. Amit Mitra for his enormous help day and night without hesitating to explain and help to resolve simple to complicated

problems. I also would like to thank Dr. Allan David for his support and great discussions. He gave me a course, and he was respectful and listened to every idea I had in my mind and discussed all the strengths and weakness points of those ideas.

I am grateful to our lab post-doc, Dr. Taraswi Mitra Ghosh. She encouraged me when I felt terrible, guided me when I needed help, and followed-up with me to ensure I make it to the end. I am also grateful to have amazing lab mates, Matthew Eggert took my hand and guided me with all the liposome's calculations and preparations. Lani Jasper was always there brainstorming to solve my experiment challenges. Joshua Davis was always ready to discuss the challenges and help finding out the solution. Mohammed Almoslem was my best study mate in the first two years and he is one of my best friends since that time. Chu Zhang was the great help when I needed to do many experiments.

I am extremely thankful to all Allison Church Bird who helped me with running the flow cytometry samples. She was delighted, humble, and she never hesitated to explain and help to achieve the best results. I also thank Sabrina Van Ginkel for her help with getting the confocal images and for her patience with me. I am thankful to Sangeet Makhija for helping me with analyzing the flow data.

I would like to thank everyone in the department of drug discovery and development. Jennifer Johnston, Christopher Smith, Kaylen Anderson, and Alexis Ramos. I also appreciate Dr. Rajesh Amin continuous support and help with his knowledge. He has been always there and happily to help in the week days and the weekends too.

Finally, I appreciate and grateful to Saudi government and the King Faisal University for their financial support through my scholarship assistance.

Table of Contents

List of Tables

List of Figures

List of Abbreviations

ADT	Androgen Deprivation Therapy
AHNAK2	AHNAK Nucleoprotein 2
ANXA2	Annexin A2
ANXA2P2	Annexin A2 Pseudogene-2
ANXA3	Annexin A3
AR	Androgen Receptor
BF	Bright Field
BPH	Benign Prostatic Hyperplasia
BSA	Bovine Serum Albumin
CAFs	Cancer-Associated Fibroblasts
CBZ	Cabazitaxel
CCM	Conditioned Culture Media
CDKNA1	Cyclin Dependent Kinase Inhibitor 1A
CR	Castration Resistant
CV	Coefficient Variation
DE	Differential Expression
DEGs	Differentially Expressed Genes
DLS	Dynamic Light Scattering
DMEM	Dulbecco's Modified Eagle's Medium
DMSO	Dimethyl Sulfoxide

DSPC	Distearoylphosphatidylcholine
DSPE-PEG-2,000	1,2-distearoyl-sn-glycero-3-phosphoethanolamine-N-[methoxy(polyethyleneglycol)-2,000]
DTX	Docetaxel
ECM	Extra Cellular Matrix
ECs	Endothelial Cells
EE	Encapsulation Efficiency
eGFP	Enhanced Green Fluorescent Protein
em	Emission
EMT	Epithelial Mesenchymal Transition
EpCAM	Epithelial Cell Adhesion Molecule
EPR	Enhanced Permeability and Retention
ex	Excitation
FBS	Fetal Bovine Serum
FOS	AP-1 Transcription Factor Subunit
FSCN1	Fascin Actin-Bundling Protein-1
GD	Ghost Dye
GSA	Gene-Specific Analysis
HA	Hyaluronic Acid
HAS3	Hyaluronan Synthase-3
HC	Hierarchical Clustering
HS-5	Normal Human Fibroblast
LNPs	Liposome Nanoparticles

LOD	Limit of Detection
LOQ	Limit of Quantification
LOXL2	Lysyl Oxidase Like 2
M1	Usually Activated Macrophages
M2	Alternatively Activated Macrophages
mCRPC	Metastatic Castration Resistant Prostate Cancer
MFBs	Myofibroblasts
MMPs	Matrix Metalloproteinases
mRNA	Messenger RNA
MTT	3-(4,5-dimethylthiazol-2-yl)-2,5-diphenyltetrazolium bromide
mV	Millivolt
NED	Neuroendocrine Differentiation
NEPC	Neuroendocrine Prostate Cancer
nmPC	Non-Metastatic Prostate Cancer
NPs	Nanoparticles
PBS	Phosphate Buffer Saline
PC-3	Prostate Cancer Cells
PCa	Prostate Cancer
PDA	Prostatic Ductal Adenocarcinoma
PDI	Polydispersity Index
PEG	Polyethylene Glycol
pHEMA	Poly(2-hydroxyethyl methacrylate)
PI	Propidium Iodide

PIN	Prostatic Intraepithelial Neoplasia
PLAU	Plasminogen Activator, Urokinase
PSA	Prostate-Specific Antigen
QC	Quality Control
r^2	Coefficient of Determination
rcf	Relative Centrifugal Force
RNAseq	Ribonucleic Acid Sequence
rRNA	Ribosomal Ribonucleic Acid
S100A6	S100 Calcium Binding Protein A6
SD	Standard Deviation
siRNA	Short Interfering Ribonucleic Acid
SSLs	Sterically Stabilized Liposomes
TAMs	Tumor-Associated Macrophages
TGFB1	Transforming Growth Factor Beta 1
TGFBR2	Transforming Growth Factor Beta Receptor 2
TME	Tumor Microenvironment
TR	Texas Red
tRNA	Transfer Ribonucleic Acid
UCHL1	Ubiquitin C-Terminal Hydrolase L1
VEGF	Vascular Endothelial Growth Factor
VEGFA	Vascular Endothelial Growth Factor A
VIM	Vimentin

CHAPTER 1

INTRODUCTION

1.1. Introduction

Prostate cancer (PCa) is the second leading cause of cancer morbidity and mortality in the U.S.[1]. The prostate gland is a walnut-sized organ that surrounds the urethra and sits below the bladder. The prostate gland is a male reproductive system responsible for producing seminal fluid (Figure 1.1)[2,3]. Benign prostatic hyperplasia (BPH) is an enlarged prostate gland, and it is common in men over the age of 40. BPH is not cancerous, but it shows similar symptoms associated with PCa. PCa is often diagnosed by prostate-specific antigen (PSA) blood test by using prostate biopsy or CT scan. Inflammation of the prostate gland (prostatitis) is another condition that is not cancerous but may increase the levels of PSA in the blood. A condition where cells of the prostate gland look abnormal is called prostatic intraepithelial neoplasia (PIN). The PIN is one of the symptoms that may indicate PCa[4].

There are different types of prostate adenocarcinoma, such as acinar adenocarcinoma, where the cells line the prostate's fluid-secreting glands. The acinar adenocarcinoma starts growing in the periphery of the prostate and may be felt during a digital rectal exam. This type of cancer increases the levels of the PSA. Another prostate adenocarcinoma type is prostatic ductal adenocarcinoma (PDA), and this type is rare but more aggressive than the acinar type. PDA is developed in the cells lining prostate gland tubes and ducts, and it does not necessarily increase the levels of the PSA. One of the aggressive types is the neuroendocrine tumor, which does not produce PSA. It develops in the nerve and gland cells that produce and release hormones into the bloodstream[5].

Prostate cancer's growth is initially hormone-dependent and uses the body's androgens. Physiologically, androgen receptors (AR) play a crucial role in maintaining

normal prostate development and homeostasis[6]. However, in advanced stages, PCa can survive and develop without needing the body's androgens, castrate-resistant. At that stage, developing metastatic castration-resistant PCa (mCRPC) is observed in ~15% of patients with a poor prognosis with an anticipated mortality rate of 19.5%[7]. Tumor metastasis creates a secondary tumor in a different region from the primary tumor, and a new tumor microenvironment (TME) is developed with various factors. These factors include immune cells, cancer-associated fibroblasts (CAFs), extracellular matrix (ECM), and many others, that contribute to the development of tumor growth, resistance, and spread[8]. Consequently, there are many gaps in our current understanding of how the TME affects tumor chemotherapy response.

Treatment strategies for non-metastatic (nm) localized and regional tumors include active surveillance, also called watchful waiting[9]. Patients with nmPC can also be treated with surgical resection (radical prostatectomy), sterilizing radiation, and first-line androgen deprivation therapy (ADT), such as abiraterone with prednisone with almost a >99% good prognosis[10]. Metastatic (m) tumors that are castration-sensitive (mCSPC) can be treated with ADT or ADT and chemotherapy. Conventional chemotherapy using anticancer agents such as docetaxel (DTX) or cabazitaxel (CBZ) is effective in treating PCa[11]. However, despite the effectiveness of the therapeutic intervention, it is anticipated that ~15% of nmCSPC and mCSPC will develop castration-resistance (CR) and mCRPC[7]; then, 2nd generation androgen receptor (AR) blocking hormone therapy is used (e.g., enzalutamide). However, treatment of castration-resistant and metastatic diseases with 2nd generation hormones and chemotherapies eventually leads to drug resistance and death. At the advanced stage, existing treatment options slightly increase survival (≤1

year)[10].

Treatment failure using conventional chemotherapy is primarily associated with high toxicity, drug resistance, or other pharmacological reasons[12]. In contrast, nanoparticles (NPs) are desired to provide a better delivery system for anticancer drugs. Nanotechnology is largely attributed to providing advantages in therapeutic applications such as drug delivery, vaccine development, imaging, and diagnosis. In this review, we will focus on how NPs contribute to drug delivery in solid tumors. For example, NPs can improve the efficacy and/or reduce the toxicity of the anticancer agent by improving its therapeutic index. Simon T. Barry, et. al., showed that Accurin polymeric NPs that encapsulated an Aurora B kinase inhibitor increased the therapeutic index *in-vivo* for up to 96 h after a single dose, which resulted lower toxicity and increased efficacy at half the dose intensity of the Aurora B kinase inhibitor[13]. NPs can also provide targeted delivery of anticancer drugs in tissue. MM-302 is a HER2-targeted antibody-liposome that encapsulates doxorubicin, and it is used concomitantly with trastuzumab or trastuzumab with cyclophosphamide to treat patients with advanced HER2-positive metastatic breast cancers. This regimen shows promising efficacy and is in phase II of clinical trials[14,15].

Moreover, NPs can enhance stability, circulation half-life, and tumor accumulation of anticancer agents. Doxil® is a good example, a 'stealth liposome' that encapsulates and precipitates doxorubicin, providing high stability of the doxorubicin and a circulation half-life of approximately two days[16]. Additionally, NPs can deliver gene therapy. For example, Atu027 is a liposome conjugated with short interfering RNAs (siRNAs) targeting endothelia-specifically expressed genes. This formulation is in phase II of

clinical trials and shows significant prolongation of survival in patients with pancreatic adenocarcinoma[17–19].

It has been described that when NPs circulate for a long time, it allows these particles to accumulate passively in the tumor due to permeable tumor vasculature and lack of efficient lymphatic drainage. This phenomenon is called the enhanced permeability and retention (EPR) effect[20]. However, studies showed that deposition of NPs in the tumor was limited when they were administered intravenously[21]. Even with all their advantages, the clinical benefit from NPs has not been observed widely in the clinic[22]. One of the challenges in optimizing NPs for human clinical use is the lack of clinically relevant models. Specifically, *in vitro* and small *in vivo* human cancer models do not effectively recapitulate physiological and pharmacological barriers[23].

In this dissertation, we sought to overcome the limitations associated with conventional 2D cell culture systems. Most *in-vitro* dose-response or chemo activity studies are conducted in 2D monolayer cell culture of a single cell type and lack architectural and physiological barriers as in 3D cell culture[24]. For example, cell shape is more natural in 3D cell culture than flat and elongated shape observed in 2D cell culture systems, and the 3D cell culture contains multiple layers compared to the 2D cell culture that grow as a monolayer on culture plates[25]. Moreover, gradient exposure to drugs, nutrients, and oxygen in 3D cell culture, whereas 2D cell culture exposure is uniform[26]. 3D cell culture provides other advantages, such as providing well cell differentiation because of the high cell junctions that allow cell-to-cell communication through exchange ions, small molecules, and electrical currents, whereas 2D cell culture has fewer cell junctions[27]. Gene and protein expression are also different between 2D and

3D cell cultures. 3D cell cultures have gene and protein levels more similar to those found in cells *in-vivo*[28]. 3D cell culture, such as spheroids, has an added advantage in that they can be easily manipulated and have either a simple or complex system such as incorporating multiple cell types, called the co-culture model[29].

A 3D cell culture is a representative tumor model that can better mimic more of the *in-vivo* characteristics of the tumor and tumor microenvironment (TME) and provides the ability to manipulate the tumor composition. We hypothesized that this system would be better at determining the impact of different factors on NPs, their distribution, drug release, or their uptake. Therefore, studying each TME factor and establishing their influence on NPs and payload is essential to optimizing and individualizing the treatment of aggressive primary cancers and metastatic diseases. In this chapter, we focus on the need to develop 3D co-culture models that can be used to establish and identify how TME factors affect NPs uptake and distribution in mCRPC.

1.2. Prostate Cancer (PCa)

Prostate cancer (PCa) is the 2nd leading cause of non-cutaneous cancer deaths among men in the U.S.[1,30]. Although in the early stages of PCa, where it is localized, there is a curative therapy, advanced stages, where it is metastasized, consider life-threatening disease[31]. Metastatic spread in PCa is different than other tumors, particularly when it becomes hormone-independent or castrate-resistant. Androgen receptors (ARs) are usually the main target when treating metastatic PCa clinically. Since PCa cells are like normal prostate cells that develop and survive depending on AR signaling; therefore, AR sensitivity is a significant factor for therapeutic outcomes[32]. However, ~15% of the

patients who receive ADT will develop castration-resistance (CR), which means PCa cells can still grow and survive even when hormone levels are low. Patients who develop metastatic castration-resistant PCa (mCRPC) have a poorer prognosis with an estimated mortality rate of 19.5%[33].

Moreover, <2% of PCa are de novo neuroendocrine prostate cancers (NEPC); however, 25% of mCRPC exhibit neuroendocrine differentiation (NED)[34]. There are many different cell lines for PCa (Table 1.1). PC-3 is a mCRPC cell line derived from bone metastasis, and it is one of the aggressive cell lines that neither responds to hormone therapy, nor expresses androgen receptors (AR-)[35]. PC-3 cell line also shows NED, which is associated with poor prognosis and survival[34]. Therefore, PC-3 is a good candidate for building a 3D model and identifying how TME factors affect NPs uptake and distribution in an aggressive mCRPC. Further description of TME and NPs in PCa will be described in this review.

1.3. Tumor Microenvironment (TME)

Solid tumors consist of parenchyma (cancer cells) and various stromal cells that contribute to tumor growth, resistance, and metastases. Stromal cells, such as fibroblasts, endothelial, immune cells, and other cells, play an essential role in affecting treatment efficacy and outcome[36]. Additionally, the presence of different stromal cells has been shown to contribute to the poor distribution and efficacy of NPs[37,38]. However, most studies focus on determining drug potency and infrequently consider how the TME factors affect the drug distribution[39–41]. Therefore, further investigations are needed to identify their impact on NPs uptake and distribution.

1.3.A. Cancer-Associated Fibroblasts (CAFs)

Normal fibroblasts work as producers of connective tissue such as extracellular matrix (ECM)[42]. Following tissue damage, normal fibroblast can be activated and produce a variety of tissue repair factors[43]. Fibroblasts participate in crosstalk with adjacent epithelial stem cells in normal homeostasis following injury to influence their behavior[44]. Following fibroblasts' participation in tissue damage by secreting ECM, fibronectin, and transforming growth factor-β, fibroblasts transition into myofibroblasts (MFBs), which are highly contractile and induce contraction of the damaged tissue to facilitate wound closure. After that, they undergo apoptosis[45]. Two major proteins secreted by normal and CAFs are vascular endothelial growth factor (VEGF) and matrix metalloproteinases (MMPs). These proteins function in the continuous production and remodeling of ECM. However, one of the distinctions between normal and CAFs is that CAFs are perpetually activated and do not undergo apoptosis[46]. Therefore, as CAFs do not undergo apoptosis, they continuously produce these proteins and support tumor invasion and progression [47]; and for this reason, they call tumors ‘wounds that do not heal’[48]. CAFs consider the most effective stromal cells within TME at ECM depositing and remodeling[49], and there are many gene expression changes and involvement in this process (Figure 1.2)[3].

Many studies have demonstrated that CAFs originated from local fibroblasts that have been experienced with tumor[50], and this process is called “stromagenesis”[51]. However, the primary origin of these fibroblasts can be different, such as bone marrow-derived mesenchymal stem cells or adipocytes. Studies identified distinct subtypes of CAFs depending on their marker protein expression[52]. Accordingly, this makes CAFs difficult

to define[53]. Nevertheless, CAFs do not express makers associated with epithelial, endothelial, and leukocyte cells; and have a different elongated morphology[54]. Table.1.2. shows some marker changes associated with normal and cancer-associated fibroblasts in PCa.

Several studies determined that CAFs play a significant role in affecting chemotherapy outcomes. Chen, et. al., demonstrated that CAFs in liver cancer deter intra-tumoral drug delivery[55]. Qin He, et. al., also showed that liposomes got higher uptake in a pancreatic tumor by targeting autophagy inhibitor hydroxychloroquine, which is responsible for activating CAFs mediated collagen generation and promotes dense stroma formation (Figure 1.3)[56]. However, CAFs are complex and widely known for their highly heterogeneous nature. Many factors affect the role of CAFs, including the stage of cancer[57]. Therefore, more exploration is vital to determine the CAFs' effect on LNPs distribution and uptake in mCRPC.

1.3.B. Endothelial cells (ECs)

In normal condition, endothelial cells (ECs) create a vasculature layer that controls and maintain nutrient, blood flow, and leukocyte. In tumor conditions, endothelial dysfunction results from chronic growth factor stimulation and hypoxia; consequently, tumor blood vessels are irregularly shaped and leaky, and blood flow is abnormal[58]. Studies have demonstrated that these abnormalities cause increased tumor growth and metastasis[59]. Therefore, understanding the role of ECs in cancer is critical to facilitating the design and development of effective therapies. Shouheng Sun, et. al., formed a 3D co-culture spheroids of ECs-glioblastoma to investigate iron oxide NPs encapsulating

tumstatin peptides that target tumor vasculatures. Interestingly, the ECs coated the co-culture spheroids' outer layer, mimicking the *in-vivo* environment with leaky vasculature. They also showed that NPs targeted the ECs in the co-culture system, which proves the targeting ability of the NPs[60].

Another aspect of ECs in cancer is identifying the uptake difference between free and encapsulated drugs when ECs are co-culture with cancer cells. Agarwal, et. al., designed a co-culture model of vascularized tumor of MCF-7 cells (human mammary cancer cells) with ECs and adipose-derived stem cells. They aimed to evaluate the effect of vascularization on the cancer resistance between free and NP-encapsulated doxorubicin, and the doxorubicin-encapsulated NPs showed a significant drop in the cancer cells IC-50 compared to the free doxorubicin[61]. The scientific output associated with TME is limited, indicating that the need for more knowledge about their influence is still highly challenging.

1.3.C. Immune cells

Solid and metastatic tumors are neoplastic cells, ECM, and other stromal cells, including infiltrated inflammatory immune cells. Cancer-associated inflammation resulting from stromal cells interactions with cancer cells promotes tumor development, genomic instability, and improved cancer cell survival. Therefore, chronic inflammation has been determined as a critical hallmark of cancer[62]. For example, 90 - 100% of all cervical cancers are caused by human papillomaviruses that cause chronic inflammation[63]. Many vital immune cells in cancer include tumor-associated macrophages (TAMs), natural killer cells, dendritic cells, effector and regulatory T cells,

and myeloid-derived suppressor cells. TAMs are one of the significant factors in TME that are initially differentiated from monocytes[64]. Macrophages are heterogeneous cell populations categorized into two subtypes: M1 (usually activated macrophages) and M2 (alternatively activated macrophages)[65]. M1 macrophages are considered antitumorigenic, and they produce proinflammatory cytokines such as interferon γ (IFN-γ) and interleukin-12 (IL-12), as well as chemokines such as C-X-C motif chemokine ligands 9 (CXCL9), which they function as killing tumor cells[66]. While, M2 macrophages are considered pro-tumor macrophages, and they produce cytokines, (*e.g.,* IL-6 and IL-10), chemokines, (*e.g.,* CXCL8), growth factors (*e.g.,* VEGF), and signaling mediators, (*e.g.,* cyclooxygenase type 2; COX-2), which function as immunosuppressive agents and promote tumorgensis and metastasis[67].

TAMs' presence in the cancer tissue is mainly linked with poor prognosis[68]. Different strategies have been applied to tackle TAMs, such as recruitment inhibition of TAMs to the tumor, reprogramming M2 and converting into M1 macrophages, M2 macrophage depletion, and CD47-signal-regulatory protein alpha pathway blocking[69–71]. Bruno Sarmento, et. al., demonstrated a 3D multicellular model using a colorectal cancer cell line with human intestinal fibroblasts and monocytes differentiated into M2 macrophages. This project used NPs loaded with chemotherapeutic Nutlin-3a and granulocyte-macrophage colony-stimulating factor (GM-CSF). GM-CSF converts M2 into M1 macrophages, which are known as antitumor phenotype[72]. Insights into the interaction between TME factors and tumor cells broaden the field rationale and allow higher intelligence to tackle these barriers.

1.3.D. Extracellular matrix (ECM)

One of the significant factors in PCa TME is the extracellular matrix (ECM). It comprises distinct components, including collagenous and non-collagenous proteins such as fibronectins, osteonectins, vitronectins, bone sialoproteins, and other proteins[73]. It has been proven that ECM plays an essential role in metastatic progression by forming a breach to the barrier[74]. Cancer cells produce multiple proteases and degrading proteins to facilitate invasion and metastasis[75]. Cancer cells experience molecular changes that regulate their morphology and functionality, epithelial-mesenchymal transition (EMT). EMT allows the degradation of the intracellular relationship, ECM breakdown, and loss of adhesive connection by matrix metalloproteinases (MMPs) activity[76,77]. MMPs are zinc-dependent peptidases with a broad affinity to ECM that are responsible for the degradation of ECMs and promote tumor growth and spread[78]. In the delivery system, Ian F. Tannock, et. al., showed lower drug penetration in a reduced volume of ECM[79]. On the other hand, other studies showed that a higher volume of ECM glycoproteins causes high interstitial fluid pressure, preventing drug penetration into the tumor[80,81]. Therefore, understanding the complex role of ECM in TME would widen the knowledge to provide the optimum treatment efficacy.

1.4. Nanoparticles (NPs)

In the last decades, there has been a substantial development in nanotechnology that led to the development of different NP types with various investigational and clinical applications. Their size range from 1 to 500 nm, and this wide range is a consequence of their variety of applications[82]. Therefore, NPs can show different properties depending on

their size and surface modifications[83]. The main advantage of nanotechnology is its small size and large surface area[84]. As a drug delivery system, NPs emerged in the pharmaceutical applications for diagnostic and therapeutic directions. Many examples include liposomes, solid NPs, nanoemulsions, and polymeric NPs. These pharmaceutical NPs have different physical and chemical properties, drug loading efficiency, drug release rate, pharmacokinetics, and toxicity.

Improvement in the application of liposome nanoparticles (LNPs) and other nanocarriers for cancer therapy has occurred over the last few decades. This advancement brought many FDA-approved LNPs such as Doxil®, Myocet®, DaunoXome®, Onivyde®, and many other NPs formulations. In addition to the multiple FDA-approved liposome formulations, LNPs are clinically relevant, and they have the flexibility to manipulate and make composite systems which is a promising future[85–88]. Being one of the oldest NPs[89] and providing an abundance of promising future, liposomes are a suitable model system to determine the interplay between LNPs and solid tumors and their microenvironment to optimize and individualize treatment of aggressive primary cancers and metastatic diseases such as mCRPC.

Liposomes are vesicular lipid carriers composed of a phospholipid bilayer that can encapsulate hydrophilic (aqueous core) and lipophilic (lipid bilayer) therapeutic or diagnostic agents. Liposomes typically include different lipids, cholesterol, and hydrophilic polymers such as polyethylene glycol (PEG). Until now, liposomes have been the most successful delivery system due to the ability to manipulate their contents. Not only that but also their preparation methods depend on many factors such as the liposome content, the materials' physicochemical properties, encapsulation efficiency,

release rate, desired volume, stability, and shelf-life[90]. Generally, preparation methods start by evaporating the organic solvent to acquire the lipids; after that, aqueous media is added to get lipid dispersion. Finally, the purification of the final product[91].

There are many methods for preparing liposomes, such as hydration of a thin lipid film methods (Bangham method)[92], reverse-phase evaporation method[93], ethanol injection methods[94], and many other ones[95–98]. The Bangham method is one of the simplest methods for liposome formation. It involves producing lipid solution (the lipid dissolved in an organic solvent), followed by the organic solvent removal to form a lipid film, usually using a rotary evaporator under pressure. Aqueous media, then dispersed over the lipid film along with agitation to detach the lipids and form the liposome vesicles[96]. The reverse-phase evaporation method is referred to as inverted micelles. It involves creating water drops that are surrounded by lipid solutions. The technique is carried out by adding a small amount of the aqueous media followed by sonication to form inverted micelles. A rotary evaporator is then used to remove the organic solvent and produce a viscous gel. Finally, more aqueous media is added, and liposome vesicles will form[99]. The ethanol injection method involved using a fine needle to inject lipid that has been dissolved in ethanol into an aqueous media to form liposome vesicles. This method is simple; however, some lipids have limited solubility in ethanol, which is inadequate to produce heterogenous liposomes[96].

One of the recent methods that received considerable attention is microfluidic devices. In general, microfluidic devices can produce small liposomes by mixing the lipids dissolved in an organic solvent and an aqueous solution under a specific flow rate ratio of the aqueous phase to the organic solvent phase[100]. This method has no extrusion through

polycarbonate membranes, sonication, or repetitive freeze and thaw steps; however, flow condition and diffusive mass transfer control the size and unilamellar vesicles[101,102]. In 2021, the FDA approved BNT16b2 and mRNA-1273 produced by Pfizer-BioNTech and Moderna to prevent severe cases of COVID-19 worldwide. All these vaccines were produced using the microfluidic devices[103].

There are various liposome classifications; however, the broadest classification is conventional, PEGylated, and targeted liposomes. Conventional LNPs represent the first generation which consists of the lipid bilayer and cholesterol such as Myocet®. Myocet is a liposome formulation encapsulating doxorubicin, and it has shown better antitumor efficacy in some clinical trials than the free form of doxorubicin. However, it presented moderate cardiac toxicity[104,105]. On the other hand, Doxil® showed significantly reduced cardiotoxicity[106]. PEGylated LNPs are adding hydrophilic polymer polyethylene glycol (PEG), which serves as a coating over the surface of the liposomes such as Doxil®. PEG coat provides more advantages such as higher stability and longer circulation half-life. These advantages are acquired by adding cholesterol and using saturated high-phase transition lipids. These stable formulations have been called Stealth™ or sterically stabilized liposomes (SSLs)[107]. Payaningal R. Somanath et al. showed an effective decrease in the growth of human prostate cells *in-vitro* and tumor (PC-3) xenograft *in-vivo* without toxicity when they used SSLs that encapsulated the p21 activated kinase inhibitor IPA-3[108]. Robert D. Arnold, et. al., investigated the effect of repetitive dosing of *i.v.* injections in an orthotopic 9L rat brain tumor model of SSL-doxorubicin on plasma pharmacokinetics and drug distribution, and they found that SSL-doxorubicin increased deposition in tumor compared to free doxorubicin[109]. Targeted LNPs are designed to

offer higher potential for site-specific delivery by conjugating ligands such as antibodies and proteins expressed at the site of disease[88]. However, there have been no targeted LNPs approved by the FDA until this day. There is limited *in-vivo* performance, and they cannot achieve their potential as targeted delivery carriers due to the poor knowledge about their pharmacokinetics and immunogenicity[88]. One of the actively targeted liposomes is MM-302, a doxorubicin-loaded immunoliposome (antibody conjugated liposomes are called immunoliposomes). MM-302 is being tested in Phase I clinical trials, and it is targeting human epithermal growth factor receptor-2 (HER-2)[110]. The application of liposomes as a drug delivery system has been applied in cancer therapy and still promising to overcome the undesired effects and toxicities caused by conventional chemotherapy.

Conventional cytotoxic chemotherapy, the administration of a free drug in an inactive vehicle, has commonly accompanied with undesired effects and toxicity because of its low specificity and high potency. Therefore, NPs are developed to overcome these problems by reducing the undesired effects and toxicity and providing higher efficacy outcomes. C. Tendler, et. al., reported that Doxil® reduced doxorubicin-mediated cardiotoxicity; this is believed to be a result of doxorubicin's stable entrapment and limited distribution in cardiac tissue[111]. LNPs can stably entrap therapeutic agents and provide long circulation time in the bloodstream. Long circulation time can cause the particles to extravasate in the leaky vasculature and accumulate into tumor vasculature. This process follows a specific phenomenon called the enhanced permeability and retention (EPR) effect[112]. However, it has been established in many clinical studies that the EPR effect in humans does not appear to be as robust as in small animal xenograft

and orthotopic models[104,111,113]. Deposition of LNPs administered intravenously at the primary tumor is limited and depends on the tumor location and how it is vascularized[114]. This poor deposition of LNPs results from using inappropriate models that cannot provide appropriate explanations.

Additionally, as solids tumors composed of different stromal cells that contribute to tumor development, growth, and metastases, they play an essential role in preventing NPs from delivering their payload to cancer cells[115]. Identifying NPs uptake and efficacy within 2D monolayer models has not been predictive of *in-vivo* response in animal models of human cancer and the translation to human clinical studies. Therefore, existing models fail to provide a platform to examine the mechanisms associated with the distribution, release, and uptake kinetics of NPs and their payloads. To address these issues, there has been increased research and development of 3D spheroid models that better represent the complexity of solid tumors.

1.5. 3D Spheroids Model

Solid tumors are composed of cancer cells and immersed in a complex of different stromal cells and factors that create a unique TME. Using a 2D cell culture model is incapable of achieving *in-vivo* structural and organization connectivity, which limits mimicking many critical properties in cells' behavior, such as their morphology, differentiation, proliferation, and gene and protein expression[115]. One of the significant limitations of the 2D cell culture model is the rapid confluence of the cells, which restricts more prolonged drug exposure. Additionally, most *in-vitro* dose-response or chemo activity studies are conducted in 2D monolayer cell culture of a single cell type

and lack architectural and physiological barriers in 3D tumors[116]. For those reasons, preclinical studies are being poorly translated. Statistics show that >90% of passed *in-vitro* drugs fail to provide desired outcomes in clinical trials, especially those meant for cancer treatment because the 2D cell culture model insufficiently represents tumor biology[117]. Moreover, that extensive failure also suggests that animal models cannot provide representative assessment for drugs meant for clinical application[118]. The impact of 3D architecture on the response of human epidermal growth factor receptor type 2 (HER2) targeting agents (i.e., Trastuzumab, Pertuzumab, and Lapatinib) was determined by Mina, et. al., using conventional 2D and 3D spheroids[119]. They found that a 3D environment presented higher sensitivity to those agents due to the inhibition of β1 integrin, a critical mediator of cell–ECM interactions[119].

3D cell culture can be obtained by different methods depending on cell type and applications. Nevertheless, there have been some methodologies that have broader applications than the other ones. For example, Corning's Matrigel® matrix and collagen (natural ECM-based hydrogels) are using a method known as hydrogels-based (soft-based) 3D scaffold. Due to hydrogels' highly porous and hydrated nature, they can provide higher representative physiology of different cell types, which can apply a wide range of studies about tumorigenicity and drug discovery and development[120]. Hydrogel-based 3D scaffold method can be obtained using natural or synthetic hydrogels. Corning Matrigel® matrix is one of the extensive ECM-based natural hydrogels that have been used in 3D cell culture *in-vitro* and *in-vivo* studies. Matrigel matrix basement has been used in different studies to identify drug sensitivity, cancer cell motility, and signaling pathways. M J Bissel, et. al., demonstrated how utilizing the Matrigel matrix enables

creating an *in-vivo* like model system using mammary epithelial cells and breast cancer[121]. Another example of natural hydrogel is Collagen type I, which is found in stromal compartments and bones. Collagen I basement also provides many exploitable studies similar to what Matrigel matrix offers[122]. Additionally, hyaluronic acid (HA) is a popular natural hydrogel used to form 3D cell culture. It can be used with additional ECM components to improve cell attachment and growth[123].

Synthetic hydrogels are biologically inert and are usually used when natural hydrogels are unsuitable[124]. One of the synthetic hydrogels examples is Corning PuraMatrix™. PuraMatrix is a peptide hydrogel that exhibits nanometer-scale fibers and pores, which is preferable to provide a suitable environment for the cells in the 3D structure. However, it is necessary to determine the appropriate mixture of bioactive molecules (e.g., growth factors and ECM proteins) to achieve optimal cell growth and differentiation[125]. Another basement to obtain a 3D cell culture model is the hard-based polymers. Alvetex® is a non-degradable inert hard-based polymer that can provide large internal volume space. Alvetex is polystyrene or polycaprolactone PCL. It is known to be used in 3D cell culture studies; however, due to some of the challenges, such as not being affected by cytotoxic compounds, not having biomechanical properties as in soft-based spheroids, and being highly rigid, a limited number developed into a commercially successful models[126]. After choosing the suitable basement for the 3D scaffold model, there are different techniques to form the spheroids.

Technical methods of spheroid formation include pellet culture, hanging drop, cultivation of molded lozenges, liquid overlay, and spinner culture. Every method provides a variety of advantages and disadvantages. Pellet culture is meant to use a

centrifugal force to obtain the cells in the bottom of a conical tube. This technique is suitable for maximizing cell-to-cell adhesion and studying cell differentiation, though centrifugation might cause shear stress that can damage the cells[127]. Hanging drops is one of the commonly used techniques that form spheroids using surface tension and gravitational force, and the drop volume and suspension density can control the size of the spheroids. Hanging drops is preferred for its low cost and the ability to produce a large number of spheroids[128]. The cultivation of molded lozenges is a technique that uses non-adhesive gel prepared in molds, and it forces cells to aggregate by continuous agitation. In this technique, spheroids size can increase without restrictions as in the hanging drops technique[129]. Liquid overlay follows the static suspension technique, which is cells spontaneously form spheroids by preventing cells from attaching to the surfaces coated with agarose gel or pHEMA. Static suspension is a simple method that provides heterogeneous spheroids in size and shape and allows easy monitoring of spheroids growing in 96-well plate[130]. The spinner culture technique uses a stirring bar in centrifugal flask bioreactor containers. This technique has many disadvantages, such as the speed of the stirring has to be controlled as high-speed affects spheroids and might dissociate them if the cells are not highly adhesive, and low speed would make the cells sink in the bottom. Spheroids' size also depends on the container size, and it is not easy to monitor the spheroids' formation as in other techniques[131]. Spheroids can be made with different basement structures and can be formed by various techniques; therefore, studying tumors, TME, drug activities, and all the other related studies are accessible and achievable.

3D cell culture is a representative tumor model that can mimic the *in-vivo* tumors and provide the ability to manipulate the tumor contents to determine each TME factors impact on the NPs and their payload uptake and distribution[132]. Therefore, studying each of the TME factors to establish their influence on NPs and payload is essential to optimize and individualize the treatment of aggressive primary cancers and metastatic diseases. In this review, we focused on the need for developing a 3D cell culture model that can establish and identify how TME factors, especially cancer-associated fibroblasts (CAFs), affect NPs uptake and distribution.

PCa cell lines	Source	Androgen sensitivity	References
LNCap	Metastatic lymph node lesion of human prostate cancer	Yes	[133]
VCAP	Vertebral bone metastasis from a patient with hormone-refractory prostate cancer	Yes	[134]
22Rv1	Human PCa that was serially propagated in xenograft mice	Yes	[135]
MDA-PCa-2b	Bone metastasis	Yes	[136]
RC77T/E	Radical prostatectomy specimen	Yes	[137]
C4-2B	Derivative subline of LNCap, which is isolated from the supraclavicular lymph node of a 50-year-old Caucasian male	Yes	[138]
DU145	Brain metastasis	No	[139]
PC3	Bone metastasis	No	[35]
PC3-M	Bone metastasis	No	[140]

Table 1.1. Prostate cancer (PCa) cell lines, source, and androgen sensitivity.

Protein Name	Expression in CAFs vs. Normal Fibroblasts	Reference
α-smooth actin	Upregulated	[141]
Asporin	Upregulated	[142]
Caveolin-1	Downregulated	[143]
Collagen Type-I	Upregulated	[144]
Fibronectin	Upregulated	[143]
Integrin-α1	Upregulated	[145]
Tenascin	Upregulated	[141]
Vimentin	Upregulated	[145]

Table 1.2. The table report some of the gene expression changes between CAFs and Normal fibroblasts in prostate cancer.

1.6 Figure Legends

Figure 1.1 Prostate gland anatomy. Anterior-posterior body axis representation of prostate gland Anatomy. Different colors of highlighted zones. Histology (Hematoxylin and Eosin (H&E) staining) of normal (left) and PCa (right). Scale bars: 50 μm.

Figure 1.2 PCa progression and tumor-stroma interactions. In normal conditions, prostate epithelial cells are organized, the underlying stroma is separated by the basement membrane from the basal and luminal cells, and the stroma has fibroblasts (expressing vimentin) and smooth muscle cells (expressing α-SMA, calponin, and desmin) that interact with epithelial to maintain tissue homeostasis, smooth muscle differentiation and inhibit epithelial cell proliferation. Increased luminal cell proliferation might consider a tumor-initiating event and potentially lead to the development of high-grade prostatic intraepithelial neoplasia (PIN). In this condition, smooth muscle cells are lower, and myofibroblasts (MFBs) are increased in presence. MFBs, extracellular matrix (ECM) component deposition, and TNC secretion increase by epithelial cells' release of TGFβ ligands, Kallikrein-related peptidase-4 (KLK4), extracellular vesicles (EVs), and other factors. When the basal cell layer is disrupted, PCa is ready for invasiveness. When fibroblasts and MFBs acquire pro-tumorigenic properties in primary PCa, they are defined as cancer-associated fibroblasts (CAFs). Marker expression is explained between normal and reactive stroma. CAFs communication with the PCa cells through the release of factors such as IL-6, IL-8, TGF, VEGF, and GDF15, stimulate tumor growth, angiogenesis, and progression. CAFs' interaction with PCa cells promotes their invasion by inducing epithelial-to-mesenchymal transition (EMT).

Figure 1.3 Targeting Evaluation in *in-vitro* pancreatic 3D spheroids. CFPE-labeled liposome nanoparticles uptake in BxPC-3/NIH 3T3 tumor spheroids. PEG-Lip is PEGylated liposomes. TR-Lip is a targeting peptide liposomes. Scale bar: 100 μm.

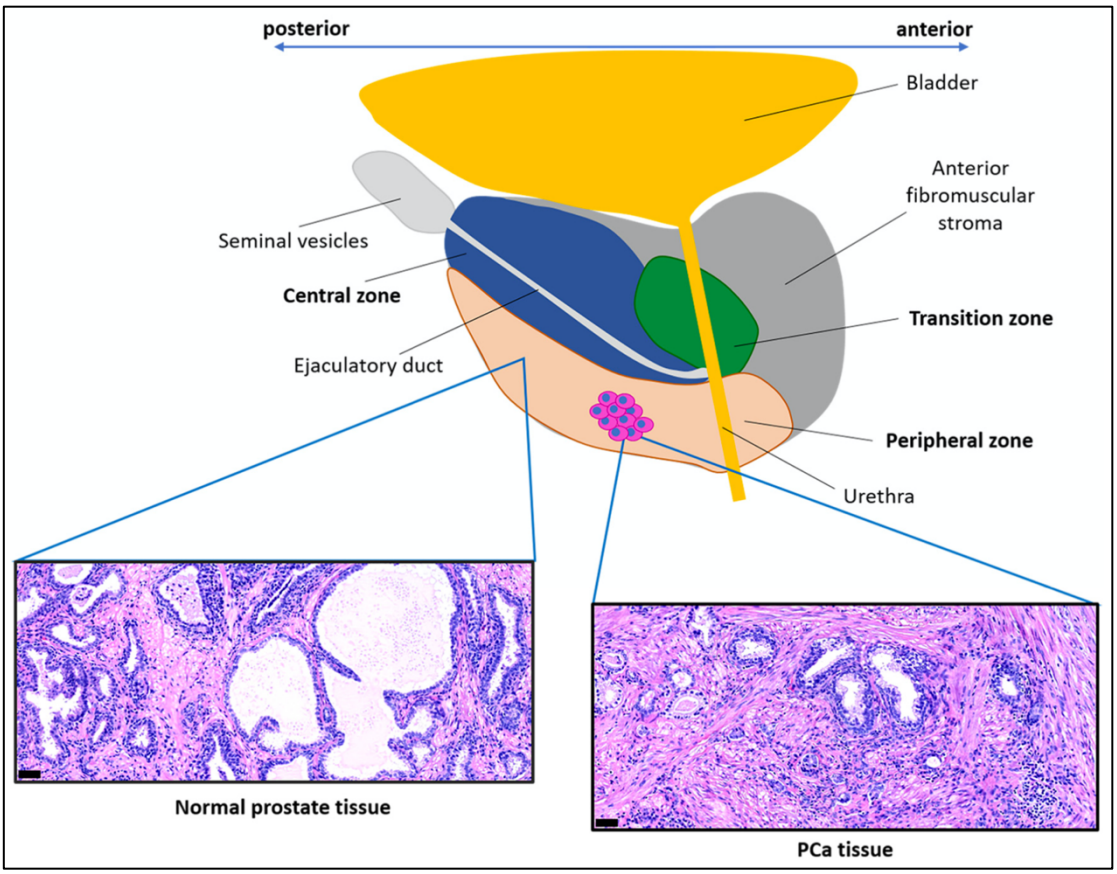

Figure 1.1
(this image is used with reprint a copyrighted permission from Creative Commons Attribution. Sofia Karkampouna *et al.*[3])

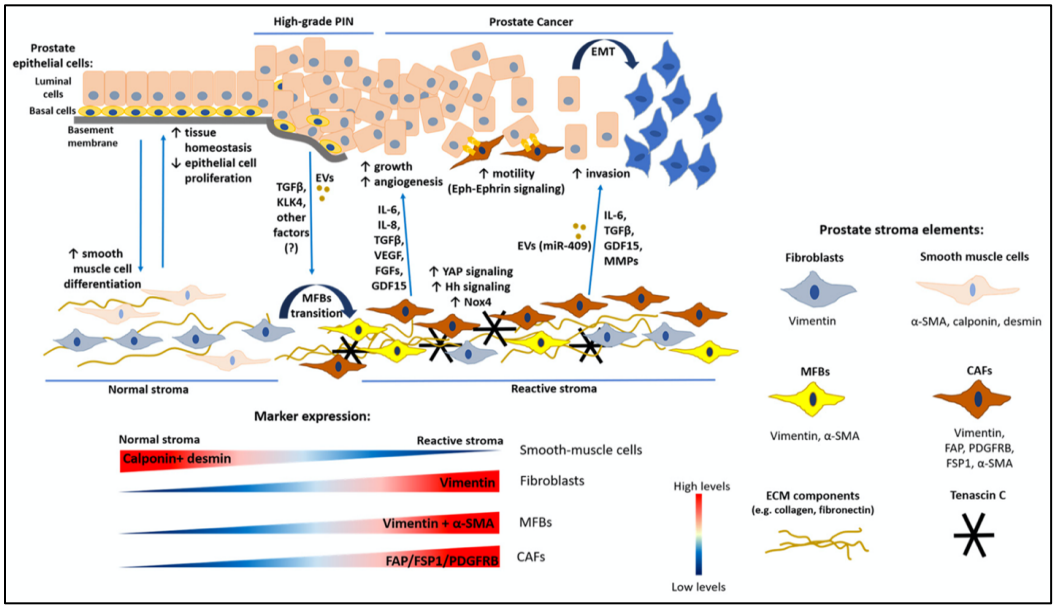

Figure 1.2
(this image is used with reprint a copyrighted permission from Creative Commons Attribution. Sofia Karkampouna *et al.*[3])

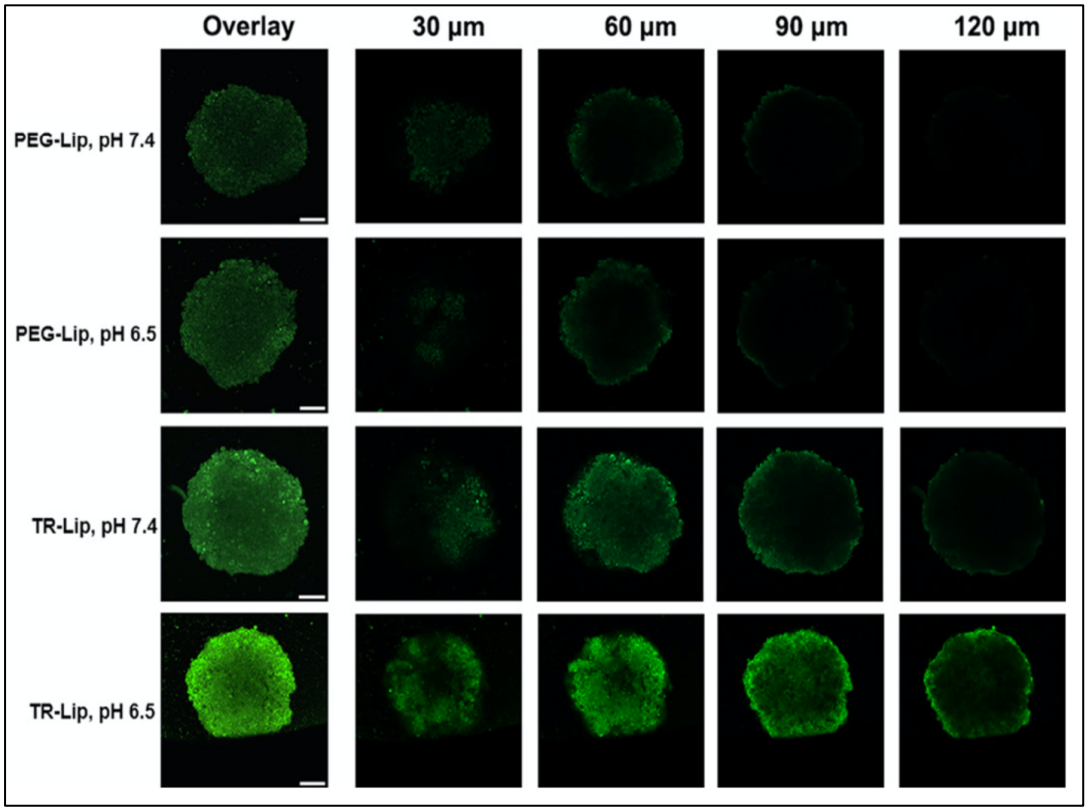

Figure 1.3
(this image is used with reprint a copyrighted permission from Elsevier, Acta Biomaterialia, LICENSE #: 5333211340125. Qin He *et al.* [56])

1.7 References

1. Siegel RL, Miller KD, Fuchs HE, Jemal A. Cancer Statistics , 2021. doi:10.3322/caac.21654
2. Hartmann D, Friess HBT-RM in LS. Adenocarcinomas☆. In: Elsevier; 2017. doi:https://doi.org/10.1016/B978-0-12-809633-8.06013-1
3. Bonollo F, Thalmann GN, Julio MK, Karkampouna S. The Role of Cancer-Associated Fibroblasts in Prostate Cancer Tumorigenesis. 2020:1-28.
4. Cheng L, Mazzucchelli R, Jones TD, Lopez-Beltran A, Montironi R. Chapter 3 - The Pathology of Prostate Cancer. In: Su L-MBT-ED and T of CSPC, ed. Philadelphia: W.B. Saunders; 2010:45-83. doi:https://doi.org/10.1016/B978-1-4160-4575-5.50009-8
5. BOSTWICK DG, MEIERS I. CHAPTER 32 - Prostate. In: Weidner N, Cote RJ, Suster S, Weiss LMBT-MSP (Second E, eds. Philadelphia: W.B. Saunders; 2009:1121-1180. doi:https://doi.org/10.1016/B978-1-4160-3966-2.00032-1
6. Wen S, Niu Y, Lee SO, Chang C. Androgen receptor (AR) positive vs negative roles in prostate cancer cell deaths including apoptosis, anoikis, entosis, necrosis and autophagic cell death. *Cancer Treat Rev*. 2014;40(1):31-40. doi:10.1016/j.ctrv.2013.07.008
7. Scher HI, Solo K, Valant J, Todd MB, Mehra M. Prevalence of Prostate Cancer Clinical States and Mortality in the United States: Estimates Using a Dynamic Progression Model. *PLoS One*. 2015;10(10):e0139440. doi:10.1371/journal.pone.0139440
8. Hernández-Camarero P, López-Ruiz E, Marchal JA, Perán M. Cancer: a mirrored

room between tumor bulk and tumor microenvironment. *J Exp Clin Cancer Res*. 2021;40(1):1-12. doi:10.1186/s13046-021-02022-5

9. Bekelman JE, Rumble RB, Chen RC, et al. Clinically Localized Prostate Cancer: ASCO Clinical Practice Guideline Endorsement of an American Urological Association/American Society for Radiation Oncology/Society of Urologic Oncology Guideline. *J Clin Oncol Off J Am Soc Clin Oncol*. 2018;36(32):3251-3258. doi:10.1200/JCO.18.00606

10. Beger HG, Rau B, Gansauge F, Leder G, Schwarz M, Poch B. Prostate Cancer – Low Survival Rates. *Dtsch Arztebl Int*. 2008. doi:10.3238/arztebl.2008.0255

11. Heidenreich A, Bastian PJ, Bellmunt J, et al. EAU guidelines on prostate cancer. Part II: Treatment of advanced, relapsing, and castration-resistant prostate cancer. *Eur Urol*. 2014;65(2):467-479. doi:10.1016/j.eururo.2013.11.002

12. Kongsted P, Svane IM, Lindberg H, Sengeløv L. Predictors of Chemotherapy-Induced Toxicity and Treatment Outcomes in Elderly Versus Younger Patients With Metastatic Castration-Resistant Prostate Cancer. *Clin Genitourin Cancer*. 2016;14(6):e559-e568. doi:10.1016/j.clgc.2016.03.018

13. Ashton S, Song YH, Nolan J, et al. Aurora kinase inhibitor nanoparticles target tumors with favorable therapeutic index in vivo. *Sci Transl Med*. 2016;8(325):1-11. doi:10.1126/scitranslmed.aad2355

14. Miller K, Cortes J, Hurvitz SA, et al. HERMIONE: A randomized Phase 2 trial of MM-302 plus trastuzumab versus chemotherapy of physician's choice plus trastuzumab in patients with previously treated, anthracycline-naïve, HER2-positive, locally advanced/metastatic breast cancer. *BMC Cancer*. 2016;16(1):1-

11. doi:10.1186/s12885-016-2385-z

15. Munster P, Krop IE, LoRusso P, et al. Safety and pharmacokinetics of MM-302, a HER2-targeted antibody–liposomal doxorubicin conjugate, in patients with advanced HER2-positive breast cancer: a phase 1 dose-escalation study. *Br J Cancer*. 2018;119(9):1086-1093. doi:10.1038/s41416-018-0235-2

16. Gabizon A., Shmeeda H., Barenholz Y. Pharmacokinetics of Pegylated Liposomal Doxorubicin: Review of Animal and Human Studies. *Clin Pharmacokinet*. 2003;5(5):419-436. http://www.ingentaconnect.com/content/adis/cpk/2003/00000042/00000005/art00002.

17. Schultheis B, Strumberg D, Kuhlmann J, et al. Safety, efficacy and pharcacokinetics of targeted therapy with the liposomal RNA interference therapeutic atu027 combined with gemcitabine in patients with pancreatic adenocarcinoma. A randomized phase Ib/IIa study. *Cancers (Basel)*. 2020;12(11):1-13. doi:10.3390/cancers12113130

18. Santel A, Aleku M, Keil O, et al. A novel siRNA-lipoplex technology for RNA interference in the mouse vascular endothelium. *Gene Ther*. 2006;13(16):1222-1234. doi:10.1038/sj.gt.3302777

19. Aleku M, Schulz P, Keil O, et al. Atu027, a liposomal small interfering RNA formulation targeting protein kinase N3, inhibits cancer progression. *Cancer Res*. 2008;68(23):9788-9798. doi:10.1158/0008-5472.CAN-08-2428

20. Kalyane D, Raval N, Maheshwari R, Tambe V, Kalia K, Tekade RK. Employment of enhanced permeability and retention effect (EPR): Nanoparticle-based precision

tools for targeting of therapeutic and diagnostic agent in cancer. *Mater Sci Eng C*. 2019;98(August 2018):1252-1276. doi:10.1016/j.msec.2019.01.066

21. Lee MK. Clinical usefulness of liposomal formulations in cancer therapy : lessons from the experiences of doxorubicin. *J Pharm Investig*. 2019;49(2):203-214. doi:10.1007/s40005-018-0398-0

22. Belfiore L, Saunders DN, Ranson M, Thurecht KJ, Storm G, Vine KL. Towards clinical translation of ligand-functionalized liposomes in targeted cancer therapy: Challenges and opportunities. *J Control Release*. 2018;277(February):1-13. doi:10.1016/j.jconrel.2018.02.040

23. Herrmann D, Conway JRW, Vennin C, et al. Three-dimensional cancer models mimic cell-matrix interactions in the tumour microenvironment. *Carcinogenesis*. 2014;35(8):1671-1679. doi:10.1093/carcin/bgu108

24. Barbosa MAG, Xavier CPR, Pereira RF, Petrikaitė V, Vasconcelos MH. 3D Cell Culture Models as Recapitulators of the Tumor Microenvironment for the Screening of Anti-Cancer Drugs. *Cancers (Basel)*. 2022;14(1):1-30. doi:10.3390/cancers14010190

25. Costa EC, Moreira AF, de Melo-Diogo D, Gaspar VM, Carvalho MP, Correia IJ. 3D tumor spheroids: an overview on the tools and techniques used for their analysis. *Biotechnol Adv*. 2016;34(8):1427-1441. doi:10.1016/j.biotechadv.2016.11.002

26. Dhaliwal A. 3D Cell Culture: A Review. *Mater Methods*. 2012:1-22. http://www.labome.com/method/3D-Cell-Culture-A-Review.html.

27. Langhans SA. Three-dimensional in vitro cell culture models in drug discovery

and drug repositioning. *Front Pharmacol*. 2018;9(JAN):1-14. doi:10.3389/fphar.2018.00006

28. Fontoura JC, Viezzer C, dos Santos FG, et al. Comparison of 2D and 3D cell culture models for cell growth, gene expression and drug resistance. *Mater Sci Eng C*. 2020;107(September 2019):110264. doi:10.1016/j.msec.2019.110264
29. Suparna S. 3D culture: Culture and Assay Systems Used for 3D Cell Culture. *Corning*. 2014;9:1-18.
30. Ghosh TM, Kansom T, Mazumder S, et al. The Andrographolide analogue 3A.1 synergizes with Taxane derivatives in aggressive metastatic prostate cancers by upregulation of Heat Shock proteins and downregulation of MAT2A-mediated cell migration and invasion. 2021;(334). doi:10.1124/jpet.121.000898
31. Powles T, Yuen KC, Gillessen S, et al. enzalutamide alone in metastatic. 2022;28(January). doi:10.1038/s41591-021-01600-6
32. Thomas C, Baunacke M, Erb HHH, et al. Systemic Triple Therapy in Metastatic Hormone-Sensitive Prostate Cancer (mHSPC): Ready for Prime Time or Still to Be Explored ? 2022:1-10.
33. Kang J, La F, Bonollo F, et al. Tumor microenvironment mechanisms and bone metastatic disease progression of prostate cancer. *Cancer Lett*. 2022;530(May 2021):156-169. doi:10.1016/j.canlet.2022.01.015
34. Yadav SS, Li J, Stockert JA, et al. Induction of Neuroendocrine Differentiation in Prostate Cancer Cells by Dovitinib (TKI-258) and its Therapeutic Implications. *Transl Oncol*. 2017;10(3):357-366. doi:10.1016/j.tranon.2017.01.011
35. Tai S, Sun Y, Squires JM, et al. PC3 is a cell line characteristic of prostatic small

cell carcinoma. *Prostate*. 2011;71(15):1668-1679. doi:10.1002/pros.21383

36. Li H, Fan X, Houghton JM. Tumor microenvironment: The role of the tumor stroma in cancer. *J Cell Biochem*. 2007;101(4):805-815. doi:10.1002/jcb.21159

37. Rajendrakumar SK, Uthaman S, Cho CS, Park IK. Nanoparticle-Based Phototriggered Cancer Immunotherapy and Its Domino Effect in the Tumor Microenvironment. *Biomacromolecules*. 2018;19(6):1869-1887. doi:10.1021/acs.biomac.8b00460

38. Musetti S, Huang L. Nanoparticle-Mediated Remodeling of the Tumor Microenvironment to Enhance Immunotherapy. *ACS Nano*. 2018;12(12):11740-11755. doi:10.1021/acsnano.8b05893

39. Song Y yuan, Yuan Y, Shi X, Che Y yuan. Improved drug delivery and anti-tumor efficacy of combinatorial liposomal formulation of genistein and plumbagin by targeting Glut1 and Akt3 proteins in mice bearing prostate tumor. *Colloids Surfaces B Biointerfaces*. 2020;190(1):110966. doi:10.1016/j.colsurfb.2020.110966

40. Ranjan A, Benjamin CJ, Negussie AH, et al. Biodistribution and Efficacy of Low Temperature-Sensitive Liposome Encapsulated Docetaxel Combined with Mild Hyperthermia in a Mouse Model of Prostate Cancer. *Pharm Res*. 2016;33(10):2459-2469. doi:10.1007/s11095-016-1971-8

41. Wang F, Chen L, Zhang R, Chen Z, Zhu L. RGD peptide conjugated liposomal drug delivery system for enhance therapeutic efficacy in treating bone metastasis from prostate cancer. *J Control Release*. 2014;196:222-233. doi:10.1016/j.jconrel.2014.10.012

42. Dick MK, Miao JH, Limaiem F. Histology, Fibroblast. In: Treasure Island (FL); 2022.

43. Gobin AS, Taylor DA, Chau E, Sampaio LC. Organogenesis. *Stem Cell Gene Ther Cardiovasc Dis*. 2015;(December):349-373. doi:10.1016/B978-0-12-801888-0.00028-X

44. Ushakumary MG, Riccetti M, Perl AKT. Resident interstitial lung fibroblasts and their role in alveolar stem cell niche development, homeostasis, injury, and regeneration. *Stem Cells Transl Med*. 2021;10(7):1021-1032. doi:10.1002/sctm.20-0526

45. Gabbiani G. The myofibroblast in wound healing and fibrocontractive diseases. *J Pathol*. 2003;200(4):500-503. doi:10.1002/path.1427

46. Itoh G, Chida S, Yanagihara K, Yashiro M, Aiba N, Tanaka M. Cancer-associated fibroblasts induce cancer cell apoptosis that regulates invasion mode of tumours. *Oncogene*. 2017;36(31):4434-4444. doi:10.1038/onc.2017.49

47. Glentis A, Oertle P, Mariani P, et al. Cancer-associated fibroblasts induce metalloprotease-independent cancer cell invasion of the basement membrane. *Nat Commun*. 2017;8(1):1-13. doi:10.1038/s41467-017-00985-8

48. Dvorak HF. Tumors: wounds that do not heal. Similarities between tumor stroma generation and wound healing. *N Engl J Med*. 1986;315(26):1650-1659. doi:10.1056/NEJM198612253152606

49. Gaggioli C, Hooper S, Hidalgo-Carcedo C, et al. Fibroblast-led collective invasion of carcinoma cells with differing roles for RhoGTPases in leading and following cells. *Nat Cell Biol*. 2007;9(12):1392-1400. doi:10.1038/ncb1658

50. Öhlund D, Handly-Santana A, Biffi G, et al. Distinct populations of inflammatory fibroblasts and myofibroblasts in pancreatic cancer. *J Exp Med*. 2017;214(3):579-596. doi:10.1084/jem.20162024

51. Beacham DA, Cukierman E. Stromagenesis: the changing face of fibroblastic microenvironments during tumor progression. *Semin Cancer Biol*. 2005;15(5):329-341. doi:10.1016/j.semcancer.2005.05.003

52. Li H, Courtois ET, Sengupta D, et al. Reference component analysis of single-cell transcriptomes elucidates cellular heterogeneity in human colorectal tumors. *Nat Genet*. 2017;49(5):708-718. doi:10.1038/ng.3818

53. Öhlund D, Elyada E, Tuveson D. Fibroblast heterogeneity in the cancer wound. *J Exp Med*. 2014;211(8):1503-1523. doi:10.1084/jem.20140692

54. Sahai E, Astsaturov I, Cukierman E, et al. A framework for advancing our understanding of cancer-associated fibroblasts. *Nat Rev Cancer*. 2020;20(3):174-186. doi:10.1038/s41568-019-0238-1

55. Guo J, Zeng H, Shi X, et al. A CFH peptide-decorated liposomal oxymatrine inactivates cancer-associated fibroblasts of hepatocellular carcinoma through epithelial–mesenchymal transition reversion. *J Nanobiotechnology*. 2022;20(1):1-19. doi:10.1186/s12951-022-01311-1

56. Chen X, Yu Q, Liu Y, et al. Synergistic cytotoxicity and co-autophagy inhibition in pancreatic tumor cells and cancer-associated fibroblasts by dual functional peptide-modified liposomes. *Acta Biomater*. 2019;99:339-349. doi:10.1016/j.actbio.2019.09.003

57. Todaro M, Gaggianesi M, Catalano V, et al. CD44v6 is a marker of constitutive

and reprogrammed cancer stem cells driving colon cancer metastasis. *Cell Stem Cell*. 2014;14(3):342-356. doi:10.1016/j.stem.2014.01.009

58. Dudley AC. Tumor endothelial cells. *Cold Spring Harb Perspect Med*. 2012;2(3):1-18. doi:10.1101/cshperspect.a006536

59. Shoval H, Karsch-Bluman A, Brill-Karniely Y, et al. Tumor cells and their crosstalk with endothelial cells in 3D spheroids. *Sci Rep*. 2017;7(1):1-11. doi:10.1038/s41598-017-10699-y

60. Ho DN, Kohler N, Sigdel A, et al. Penetration of endothelial cell coated multicellular tumor spheroids by iron oxide nanoparticles. *Theranostics*. 2012;2(1):66-75. doi:10.7150/thno.3568

61. Agarwal P, Wang H, Sun M, et al. Microfluidics Enabled Bottom-Up Engineering of 3D Vascularized Tumor for Drug Discovery. *ACS Nano*. 2017;11(7):6691-6702. doi:10.1021/acsnano.7b00824

62. Hussain SP, Amstad P, Raja K, et al. Increased p53 mutation load in noncancerous colon tissue from ulcerative colitis: a cancer-prone chronic inflammatory disease. *Cancer Res*. 2000;60(13):3333-3337.

63. Bosch FX, Lorincz A, Muñoz N, Meijer CJLM, Shah K V. The causal relation between human papillomavirus and cervical cancer. *J Clin Pathol*. 2002;55(4):244-265. doi:10.1136/jcp.55.4.244

64. Cheng H, Zheng Z, Cheng T. New paradigms on hematopoietic stem cell differentiation. *Protein Cell*. 2020;11(1):34-44. doi:10.1007/s13238-019-0633-0

65. Guerriero JL. Macrophages: The Road Less Traveled, Changing Anticancer Therapy. *Trends Mol Med*. 2018;24(5):472-489.

doi:10.1016/j.molmed.2018.03.006

66. Biswas SK, Mantovani A. Macrophage plasticity and interaction with lymphocyte subsets: Cancer as a paradigm. *Nat Immunol*. 2010;11(10):889-896. doi:10.1038/ni.1937

67. Pathria P, Louis TL, Varner JA. Targeting Tumor-Associated Macrophages in Cancer. *Trends Immunol*. 2019;40(4):310-327. doi:10.1016/j.it.2019.02.003

68. Braun MS, Seymour MT. Balancing the efficacy and toxicity of chemotherapy in colorectal cancer. *Ther Adv Med Oncol*. 2011;3(1):43-52. doi:10.1177/1758834010388342

69. Hu G, Guo M, Xu J, et al. Nanoparticles targeting macrophages as potential clinical therapeutic agents against cancer and inflammation. *Front Immunol*. 2019;10(AUG):1-14. doi:10.3389/fimmu.2019.01998

70. Song C, Phuengkham H, Kim YS, et al. Syringeable immunotherapeutic nanogel reshapes tumor microenvironment and prevents tumor metastasis and recurrence. *Nat Commun*. 2019;10(1). doi:10.1038/s41467-019-11730-8

71. Nie W, Wu G, Zhang J, et al. Responsive Exosome Nano-bioconjugates for Synergistic Cancer Therapy. *Angew Chemie - Int Ed*. 2020;59(5):2018-2022. doi:10.1002/anie.201912524

72. Bauleth-Ramos T, Feijão T, Gonçalves A, et al. Colorectal cancer triple co-culture spheroid model to assess the biocompatibility and anticancer properties of polymeric nanoparticles. *J Control Release*. 2020;323(April):398-411. doi:10.1016/j.jconrel.2020.04.025

73. Nallanthighal S, Heiserman JP, Cheon DJ. The Role of the Extracellular Matrix in

Cancer Stemness. *Front Cell Dev Biol*. 2019;7(July):1-14. doi:10.3389/fcell.2019.00086

74. Kiefer JA, Farach-Carson MC. Type I collagen-mediated proliferation of PC3 prostate carcinoma cell line: implications for enhanced growth in the bone microenvironment. *Matrix Biol*. 2001;20(7):429-437. doi:10.1016/s0945-053x(01)00159-7

75. Stamenkovic I. Matrix metalloproteinases in tumor invasion and metastasis. *Semin Cancer Biol*. 2000;10(6):415-433. doi:10.1006/scbi.2000.0379

76. Yu D, Ye T, Xiang Y, et al. Quercetin inhibits epithelial-mesenchymal transition, decreases invasiveness and metastasis, and reverses IL-6 induced epithelial-mesenchymal transition, expression of MMP by inhibiting STAT3 signaling in pancreatic cancer cells. *Onco Targets Ther*. 2017;10:4719-4729. doi:10.2147/OTT.S136840

77. Thiery JP. Epithelial-mesenchymal transitions in tumour progression. *Nat Rev Cancer*. 2002;2(6):442-454. doi:10.1038/nrc822

78. Nagase H, Visse R, Murphy G. Structure and function of matrix metalloproteinases and TIMPs. *Cardiovasc Res*. 2006;69(3):562-573. doi:10.1016/j.cardiores.2005.12.002

79. Grantab R, Sivananthan S, Tannock IF. The penetration of anticancer drugs through tumor tissue as a function of cellular adhesion and packing density of tumor cells. *Cancer Res*. 2006;66(2):1033-1039. doi:10.1158/0008-5472.CAN-05-3077

80. Jacobetz MA, Chan DS, Neesse A, et al. Hyaluronan impairs vascular function and

drug delivery in a mouse model of pancreatic cancer. *Gut*. 2013;62(1):112-120. doi:10.1136/gutjnl-2012-302529

81. Olive KP, Jacobetz MA, Davidson CJ, et al. Inhibition of Hedgehog signaling enhances delivery of chemotherapy in a mouse model of pancreatic cancer. *Science*. 2009;324(5933):1457-1461. doi:10.1126/science.1171362

82. Ullah MS, Zhivonitko V V., Samoylenko A, et al. Identification of extracellular nanoparticle subsets by nuclear magnetic resonance. *Chem Sci*. 2021;12(24):8311-8319. doi:10.1039/d1sc01402a

83. Najahi-Missaoui W, Arnold RD, Cummings BS. Safe nanoparticles: Are we there yet? *Int J Mol Sci*. 2021;22(1):1-22. doi:10.3390/ijms22010385

84. Nazanin Hoshyar; Samantha Gray; Hongbin Han; Gang BaoHan H. The effect of nanoparticle size on in vivo pharmacokinetics and cellular interaction. 2016;11:673-692.

85. Dey S, Hasnain MS, Nayak AK. Chitosan nanocomposites for biomedical applications. *Chitosan Biomed Appl*. 2022;1:111-138. doi:10.1016/b978-0-12-821058-1.00011-3

86. Lamichhane N, Sharma S, Parul, Verma AK, Roy I, Sen T. Iron oxide-based magneto-optical nanocomposites for in vivo biomedical applications. *Biomedicines*. 2021;9(3):1-28. doi:10.3390/biomedicines9030288

87. Mitchell MJ, Jain RK, Langer R. Engineering and physical sciences in oncology: challenges and opportunities. *Nat Rev Cancer*. 2017;17(11):659-675. doi:10.1038/nrc.2017.83

88. Sercombe L, Veerati T, Moheimani F, Wu SY, Sood AK, Hua S. Advances and

challenges of liposome assisted drug delivery. *Front Pharmacol*. 2015;6(DEC):1-13. doi:10.3389/fphar.2015.00286

89. Bangham AD, Standish MM, Watkins JC. Diffusion of univalent ions across the lamellae of swollen phospholipids. *J Mol Biol*. 1965;13(1):238-252. doi:10.1016/S0022-2836(65)80093-6

90. Elder P, Franklin B. Chapter 1 Liposomes Came First : The Early History of Liposomology. 2017;1522. doi:10.1007/978-1-4939-6591-5

91. Missaoui WN, Arnold RD, Cummings BS. Toxicological status of nanoparticles: What we know and what we don't know. *Chem Biol Interact*. 2018;295(xxxx):1-12. doi:10.1016/j.cbi.2018.07.015

92. Deamer D, Bangham AD. Large volume liposomes by an ether vaporization method. *Biochim Biophys Acta*. 1976;443(3):629-634. doi:10.1016/0005-2736(76)90483-1

93. Szoka F, Papahadjopoulos D. Procedure for preparation of liposomes with large internal aqueous space and high capture by reverse-phase evaporation. *Proc Natl Acad Sci U S A*. 1978;75(9):4194-4198. doi:10.1073/pnas.75.9.4194

94. Batzri S, Korn ED. Single bilayer liposomes prepared without sonication. *Biochim Biophys Acta*. 1973;298(4):1015-1019. doi:10.1016/0005-2736(73)90408-2

95. Brunner J, Skrabal P, Hauser H. Single bilayer vesicles prepared without sonication. Physico-chemical properties. *Biochim Biophys Acta*. 1976;455(2):322-331. doi:10.1016/0005-2736(76)90308-4

96. Meure LA, Foster NR, Dehghani F. Conventional and dense gas techniques for the production of liposomes: A review. *AAPS PharmSciTech*. 2008;9(3):798-809.

doi:10.1208/s12249-008-9097-x

97. Mozafari MR. Liposomes: an overview of manufacturing techniques. *Cell Mol Biol Lett*. 2005;10(4):711-719.

98. Li C, Deng Y. A novel method for the preparation of liposomes: freeze drying of monophase solutions. *J Pharm Sci*. 2004;93(6):1403-1414. doi:10.1002/jps.20055

99. Shi N-Q, Qi X-R. Preparation of Drug Liposomes by Reverse-Phase Evaporation. 2021;(January):37-46. doi:10.1007/978-3-662-49320-5_3

100. Matsuura-sawada Y, Maeki M, Nishioka T, et al. Micro fl uidic Device-Enabled Mass Production of Lipid-Based Nanoparticles for Applications in Nanomedicine and Cosmetics. 2022. doi:10.1021/acsanm.2c00886

101. Carugo D, Bottaro E, Owen J, Stride E, Nastruzzi C. Liposome production by microfluidics: Potential and limiting factors. *Sci Rep*. 2016;6:1-15. doi:10.1038/srep25876

102. Van Swaay D, Demello A. Microfluidic methods for forming liposomes. *Lab Chip*. 2013;13(5):752-767. doi:10.1039/c2lc41121k

103. Schoenmaker L, Witzigmann D, Kulkarni JA, et al. mRNA-lipid nanoparticle COVID-19 vaccines: Structure and stability. *Int J Pharm*. 2021;601(March):120586. doi:10.1016/j.ijpharm.2021.120586

104. Batist G, Ramakrishnan G, Rao CS, et al. Reduced cardiotoxicity and preserved antitumor efficacy of liposome-encapsulated doxorubicin and cyclophosphamide compared with conventional doxorubicin and cyclophosphamide in a randomized, multicenter trial of metastatic breast cancer. *J Clin Oncol Off J Am Soc Clin Oncol*. 2001;19(5):1444-1454. doi:10.1200/JCO.2001.19.5.1444

105. Cortes J, Di Cosimo S, Climent MA, et al. Nonpegylated liposomal doxorubicin (TLC-D99), paclitaxel, and trastuzumab in HER-2-overexpressing breast cancer: a multicenter phase I/II study. *Clin cancer Res an Off J Am Assoc Cancer Res*. 2009;15(1):307-314. doi:10.1158/1078-0432.CCR-08-1113

106. O'Brien MER, Wigler N, Inbar M, et al. Reduced cardiotoxicity and comparable efficacy in a phase III trial of pegylated liposomal doxorubicin HCl (CAELYX™/Doxil®) versus conventional doxorubicin for first-line treatment of metastatic breast cancer. *Ann Oncol*. 2004;15(3):440-449. doi:10.1093/annonc/mdh097

107. Martin M, Wei H, Lu T. Targeting microenvironment in cancer therapeutics. *Oncotarget*. 2016;7(32). doi:10.18632/oncotarget.9824

108. Verma A, Najahi-Missaoui W, Cummings BS, Somanath PR. Sterically stabilized liposomes targeting P21 (RAC1) activated kinase-1 and secreted phospholipase A(2) suppress prostate cancer growth and metastasis. *Oncol Lett*. 2020;20(5):179. doi:10.3892/ol.2020.12040

109. Arnold RD, Mager DE, Slack JE, Straubinger RM. Effect of repetitive administration of doxorubicin-containing liposomes on plasma pharmacokinetics and drug biodistribution in a rat brain tumor model. *Clin Cancer Res*. 2005;11(24):8856-8865. doi:10.1158/1078-0432.CCR-05-1365

110. Børresen B, Hansen AE, Fliedner FP, et al. Noninvasive molecular imaging of the enhanced permeability and retention effect by64Cu-liposomes: In vivo correlations with68Ga-RGD, fluid pressure, diffusivity and18F-FDG. *Int J Nanomedicine*. 2020;15:8571-8581. doi:10.2147/IJN.S239172

111. O'Brien MER, Wigler N, Inbar M, et al. Reduced cardiotoxicity and comparable efficacy in a phase III trial of pegylated liposomal doxorubicin HCl (CAELYX/Doxil) versus conventional doxorubicin for first-line treatment of metastatic breast cancer. *Ann Oncol Off J Eur Soc Med Oncol*. 2004;15(3):440-449. doi:10.1093/annonc/mdh097

112. Immordino ML, Cattel L. Stealth liposomes : review of the basic science , rationale , and clinical applications , existing and potential. 2006:297-315.

113. Nichols JW, Bae YH. EPR: Evidence and fallacy. *J Control Release*. 2014;190:451-464. doi:10.1016/j.jconrel.2014.03.057

114. Luo D, Carter KA, Molins EAG, et al. Pharmacokinetics and pharmacodynamics of liposomal chemophototherapy with short drug-light intervals. *J Control Release*. 2019;297:39-47. doi:https://doi.org/10.1016/j.jconrel.2019.01.030

115. Jensen C, Teng Y. Is It Time to Start Transitioning From 2D to 3D Cell Culture? *Front Mol Biosci*. 2020;7(March):1-15. doi:10.3389/fmolb.2020.00033

116. Fontana F, Raimondi M, Marzagalli M, Sommariva M, Gagliano N, Limonta P. Three-dimensional cell cultures as an in vitro tool for prostate cancer modeling and drug discovery. *Int J Mol Sci*. 2020;21(18):1-18. doi:10.3390/ijms21186806

117. Rahbari M, Rahlfs S, Jortzik E, Bogeski I, Becker K. H2O2 dynamics in the malaria parasite Plasmodium falciparum. *PLoS One*. 2017;12(4). doi:10.1371/journal

118. Bugelski PJ, Martin PL. Concordance of preclinical and clinical pharmacology and toxicology of therapeutic monoclonal antibodies and fusion proteins: Cell surface targets. *Br J Pharmacol*. 2012;166(3):823-846. doi:10.1111/j.1476-

5381.2011.01811.x

119. Weigelt B, Lo AT, Park CC, Gray JW, Bissell MJ. HER2 signaling pathway activation and response of breast cancer cells to HER2-targeting agents is dependent strongly on the 3D microenvironment. *Breast Cancer Res Treat*. 2010;122(1):35-43. doi:10.1007/s10549-009-0502-2

120. Comley J. 3D cell culture: Easier said than done! *Drug Discov World*. 2010;11(3):25-41.

121. Barcellos-Hoff MH, Aggeler J, Ram TG, Bissell MJ. Functional differentiation and alveolar morphogenesis of primary mammary cultures on reconstituted basement membrane. *Development*. 1989;105(2):223-235. doi:10.1242/dev.105.2.223

122. Sisson K, Zhang C, Farach-Carson MC, Chase DB, Rabolt JF. Evaluation of cross-linking methods for electrospun gelatin on cell growth and viability. *Biomacromolecules*. 2009;10(7):1675-1680. doi:10.1021/bm900036s

123. Jia XXAKJDAHMCF-CX. Hyaluronic Acid-Based Hydrogels: from a Natural Polysaccharide to Complex Networks. *Soft Matter*. 2012;8(12):3280-3294. doi:10.1039/C2SM06463D.Hyaluronic

124. Sawhney AS, Pathak CP, Hubbell JA. Photopolymerized Polyethylene glycol)-co-poly(-hydroxy. *Macromolecules*. 1993;26:581-587.

125. Horii A, Wang X, Gelain F, Zhang S. Biological designer self-assembling peptide nanofiber scaffolds significantly enhance osteoblast proliferation, differentiation and 3-D migration. *PLoS One*. 2007;2(2):1-9. doi:10.1371/journal.pone.0000190

126. Haycock JW. 3D cell culture: a review of current approaches and techniques.

Methods Mol Biol. 2011;695:1-15. doi:10.1007/978-1-60761-984-0_1

127. Achilli T-M, Meyer J, Morgan JR. Advances in the formation, use and understanding of multi-cellular spheroids. *Expert Opin Biol Ther*. 2012;12(10):1347-1360. doi:10.1517/14712598.2012.707181

128. Ryu N-E, Lee S-H, Park H. Spheroid Culture System Methods and Applications for Mesenchymal Stem Cells. *Cells*. 2019;8(12). doi:10.3390/cells8121620

129. Gong X, Lin C, Cheng J, et al. Generation of multicellular tumor spheroids with microwell-based agarose scaffolds for drug testing. *PLoS One*. 2015;10(6):1-18. doi:10.1371/journal.pone.0130348

130. Carlsson J, Yuhas JM. Liquid-overlay culture of cellular spheroids. *Recent results cancer Res Fortschritte der Krebsforsch Prog dans les Rech sur le cancer*. 1984;95:1-23. doi:10.1007/978-3-642-82340-4_1

131. Nyberg SL, Hardin J, Amiot B, Argikar UA, Remmel RP, Rinaldo P. Rapid, large-scale formation of porcine hepatocyte spheroids in a novel spheroid reservoir bioartificial liver. *Liver Transplant Off Publ Am Assoc Study Liver Dis Int Liver Transplant Soc*. 2005;11(8):901-910. doi:10.1002/lt.20446

132. Su T, Yang B, Gao T, Liu T, Li J. Polymer nanoparticle-assisted chemotherapy of pancreatic cancer. *Ther Adv Med Oncol*. 2020;12:1-33. doi:10.1177/1758835920915978

133. Castanares MA, Copeland BT, Chowdhury WH, et al. Characterization of a novel metastatic prostate cancer cell line of LNCaP origin. *Prostate*. 2016;76(2):215-225. doi:10.1002/pros.23115

134. Makkonen H, Kauhanen M, Jääskeläinen T, Palvimo JJ. Androgen receptor

amplification is reflected in the transcriptional responses of Vertebral-Cancer of the Prostate cells. *Mol Cell Endocrinol*. 2011;331(1):57-65. doi:10.1016/j.mce.2010.08.008

135. Sramkoski RM, Pretlow TG 2nd, Giaconia JM, et al. A new human prostate carcinoma cell line, 22Rv1. *In Vitro Cell Dev Biol Anim*. 1999;35(7):403-409. doi:10.1007/s11626-999-0115-4

136. Wang B-D, Yang Q, Ceniccola K, et al. Androgen Receptor-Target Genes in African American Prostate Cancer Disparities. Robson C, ed. *Prostate Cancer*. 2013;2013:763569. doi:10.1155/2013/763569

137. Theodore S, Sharp S, Zhou J, et al. Establishment and characterization of a pair of non-malignant and malignant tumor derived cell lines from an African American prostate cancer patient. *Int J Oncol*. 2010;37(6):1477-1482. doi:10.3892/ijo-00000800

138. Spans L, Helsen C, Clinckemalie L, et al. Comparative genomic and transcriptomic analyses of LNCaP and C4-2B prostate cancer cell lines. *PLoS One*. 2014;9(2):e90002. doi:10.1371/journal.pone.0090002

139. Scaccianoce E, Festuccia C, Dondi D, et al. Characterization of prostate cancer DU145 cells expressing the recombinant androgen receptor. *Oncol Res*. 2003;14(2):101-112. doi:10.3727/000000003108748658

140. Sehgal I, Foster TP, Francis J. Prostate cancer cells show elevated urokinase receptor in a mouse model of metastasis. *Cancer Cell Int*. 2006;6:1-9. doi:10.1186/1475-2867-6-21

141. Ishii K, Mizokami A, Tsunoda T, et al. Heterogenous induction of carcinoma-

associated fibroblast-like differentiation in normal human prostatic fibroblasts by co-culturing with prostate cancer cells. *J Cell Biochem*. 2011;112(12):3604-3611. doi:10.1002/jcb.23291

142. Özdemir BC, Hensel J, Secondini C, et al. The molecular signature of the stroma response in prostate cancer-induced osteoblastic bone metastasis highlights expansion of hematopoietic and prostate epithelial stem cell niches. *PLoS One*. 2014;9(12):1-32. doi:10.1371/journal.pone.0114530

143. Orr B, Riddick ACP, Stewart GD, et al. Identification of stromally expressed molecules in the prostate by tag-profiling of cancer-associated fibroblasts, normal fibroblasts and fetal prostate. *Oncogene*. 2012;31(9):1130-1142. doi:10.1038/onc.2011.312

144. Tuxhorn JA, Ayala GE, Smith MJ, Smith VC, Dang TD, Rowley DR. Reactive stroma in human prostate cancer: induction of myofibroblast phenotype and extracellular matrix remodeling. *Clin cancer Res an Off J Am Assoc Cancer Res*. 2002;8(9):2912-2923.

145. Liu AY, True LD. Characterization of prostate cell types by CD cell surface molecules. *Am J Pathol*. 2002;160(1):37-43. doi:10.1016/S0002-9440(10)64346-5

CHAPTER 2

MATERIALS AND METHODS

2.1 Chemicals and Reagents

Cell Culture: Fetal bovine serum (FBS) and trypsin (0.25% w/v) were purchased from Hyclone (Thermo Fisher Scientific Inc. Rockford, IL). F-12K Nutrient Mixture Medium (Kaighn's Mod.) was purchased from ATCC (Manassas, VA). Dulbecco's Modified Eagle's Medium (DMEM), Matrigel® Matrix low concentration (#356237), and Calcein AM were purchased from Corning (Manassas, VA). Trypan blue solution (0.4% w/v) was purchased from Cell Gro (Herndon, VA). Dimethyl sulfoxide (DMSO) was obtained from EMD Millipore Corporation (Darmstadt, Germany). 3-(4,5-dimethylthiazol-2-yl)-2,5-diphenyltetrazolium bromide (MTT), propidium iodide (PI) (Figure 2.1), and phosphate-buffered saline (PBS) were purchased from Sigma-Aldrich Inc. (St. Louis, MO).

Liposome formulations: Distearoylphosphatidylcholine (DSPC) and 1,2-distearoyl-sn-glycero-3-phosphoethanolamine-N-[methoxy(polyethyleneglycol)-2,000] (DSPE-PEG-2,000), and cholesterol were purchased from Avanti Polar Lipids Inc (Alabaster, USA) (Figure 2.2), chloroform was purchased from Avantor (Center Valley, PA), absolute ethanol (>99% v/v) was purchased from COPTEC (King of Prussia, PA), and dialysis membranes were purchased from Fisher Scientific (Pittsburgh, PA).

Flow cytometry: Antibody EpCAM Alexa Fluor® 647 Conjugate (5447) and Ghost Dye™ Red 780 (18452) were purchased from Cell Signaling Technology (Danvers, MA), Accumax was purchased from Innovative Cell Technologies (San Diego, CA), beads and Fc block were purchased from BD Biosciences (San Jose, CA), and FLOWMI™ cell strainers were purchased from SP-Bel-Art (Wayne, NJ). All glass and plastic ware were purchased from VWR (Radnor, PA).

Confocal imaging: Hoechst 33342 dye was purchased from Enzo Life Sciences (Farmingdale, NY), and CoverWell™ Imaging Chambers were purchased from Electron Microscopy Sciences (Hatfield, PA).

mRNA sequencing (RNA-seq): RNA Stabilization Reagent (Qiagen RNAlater™) was purchased for cell pellets preservation for future RNA isolation. QIAshredder and RNeasy kit (Qiagen) was purchased for RNA isolation. RNA quantification was performed by using Nanodrop-8000 spectrophotometer (Thermo Scientific, USA), Qubit 2.0 Fluorometer (Invitrogen, Carlsbad, CA, USA), and Agilent 2100 Bioanalyzer (Applied Biosystems, Carlsbad, CA, USA). RNA-seq libraries were constructed using Illumina TruSeq RNA Sample Preparation kit v2.

2.2 Cell Lines and Cell Culture

The human adenocarcinoma PCa cell line (PC-3) was obtained from American Type Culture Collection (ATCC, Rockville, MD). The PC-3 cell line that stably expresses enhanced GFP (eGFP-PC-3) was purchased from Perkin Elmer Life Sciences. The human bone marrow fibroblast cell line (HS-5) was gifted by our collaborator Dr. Amit Kumar Mitra, Auburn University. The cell lines were authenticated at the source and tested randomly at regular intervals for tissue specimen provenance and cell lineage (detect contaminants, including extraneous tissue or mixed cell populations) at the AU Center for Pharmacogenomics and Single-Cell Omics (AUPharmGx) using GenePrint 24 System (Promega). PC-3 cells were maintained in 10% (v/v) fetal bovine serum (FBS) supplemented in F-12K and HS-5 in Dulbecco's Modified Eagle's Medium (DMEM).

Conditioned Culture Medium (CCM): The CCM was prepared by growing PC-3 cells in ten 175 cm^2 flasks in complete growth media (F-12K). When cells reached about 90% confluence, they were washed with 1X PBS twice and incubated with 24 mL of serum-free DMEM. After 24 h, CCM was collected in 50 mL conical tubes, centrifuged for 10 min at 1,000rcf, and passed through a 0.22 μm filter to eliminate debris and cell floaters. Then, 10% (v/v) FBS was added to the CCM and used in further subcultures with HS-5 to convert into CAFs[1].

Generation of Cancer-Associated Fibroblasts (CAFs): HS-5 cells were not able to grow well in F-12K media, and PC-3 cells were not able to grow well in DMEM media. Hence, all experiments requiring incubation of HS-5 cells with PC-3 cells CCM and F-12K were used in the same ratio. Further, CAFs were generated by culturing HS-5 cells in a conditioned culture medium (CCM, described earlier)[1]. All cells were maintained at 37°C, 21% O_2, and 5% CO_2 in a humidified cell culture chamber (Heracell™ VIOS 160i CO_2; Thermo Scientific™) and passaged when they reached 80-90% confluence. The cells were passaged every 2 to 3 days in order to maintain them in a logarithmic growth phase. To confirm healthy growth, cell viability was measured using Countess Automated Cell Counter (Bio-Rad TC10™ Automated Cell Counter) and using a hematocytometer (Bright-Line, Horsham, PA), a cell line with >95% viability was used for further experiments.

2.3 3D Spheroid Preparation (Mono-Cellular; PC-3 and Multicellular Co-culture; PC-3+CAFs)

Cells were maintained in culture as described above. At the time of passage, multiple flasks were passaged to maintain them in a logarithmic growth phase and provide enough cells to form spheroids (5,000 cells/spheroid). Cell viability was determined after a sample was stained with trypan blue and counted using a hematocytometer (Bright-Line, Horsham, PA). The cell viability was over 95% to proceed with the experiment. Spheroids were prepared using a liquid-overlay culture[2]. Briefly, a cell suspension in ice-cold complete growth media (F-12K for the PC-3 cells and CCM (described earlier) for the CAFs cells) and (2.5% v/v) Matrigel was made at the concentration 5,000 cells/100 µl for spheroid formation. The plates used were 96-well poly HEMA coated. Poly HEMA was made at 1.2% (w/v) in 95% (v/v) ethanol in stirring condition at 60 °C overnight. 96 well-plates (round bottom) were kept heated at 60 °C during the coating experiment in a sterile condition (Class II, Type A2 Biosafety Cabinet). A 60 µl volume of poly HEMA was added onto each well until dry (~1 h)[3]. The cell suspension (PC-3 alone or PC-3 with CAFs (co-culture) was plated at 100 µL per well (5,000 total cells, when co-culture 1:1 ratio was applied (2,500 cells/cell type)) (Table 2.1). In co-culture, each cell type suspension was prepared separately, and cells were added in a random sequence (CAFs then PC-3 or PC-3 then CAFs). The 60 inner wells of 96 well poly HEMA coated plates were used for spheroid formation. The plate was centrifuged at 1,000 rcf for 10 min at 4 °C and placed into a humidified cell incubator at 37 °C, 21% O_2 and 5% CO_2. Spheroids were formed overnight (within 24 h), but studies were not initiated for at least 2 days of growth (allowed to stabilize for 1-2 days prior to initiating drug treatment).

2.4 Preparations of PI-liposomes

Liposomes were prepared using the thin-film hydration method followed by freeze-thaw and a hand extrusion process[4,5]. Briefly, phospholipids, cholesterol, and/or DSPE-PEG-2,000 were dissolved in chloroform and mixed together (total phospholipid is 10 mM) in a glass Pyrex test-tube or round bottom flask and dried under vacuum at 65 °C (water bath) for 25 min using a rotary evaporator (Büchi Labortechnik AG, Postlfach, Switzerland) to form a thin film. The thin film was hydrated using a previously prepared 1 mM PI solution. The formulation was heated above the phase transition of the primary lipid using a water bath at 65 °C and vortexed intermittently for 1 h to allow the thin film to detach and form multilamellar vesicles. The formulation then underwent seven freeze-thaw cycles using liquid nitrogen and a 65 °C water bath to result in unilamellar vesicles. Desired particle size was achieved by extrusion (n =10) through double-stacked laser-etched 100 nm polycarbonate membranes (Whatman, Sigma-Aldrich Inc., St. Louis, MO) using a Liposofast (Avestin Inc., Ottawa, Ontario, Canada) hand extruder at 65 °C. Free, unencapsulated, PI was removed after the formulation was transferred into a dialysis bag and placed in a glass beaker with cold 10% (w/v) sucrose. The beaker was placed in a cold room (4 °C) on a stir plate at low speed, and the dialysate was exchanged three times (at approx. 1, 4, and 24 hr). The resultant liposome sample was stored at 4 °C and protected from light.

2.5 Liposome Characterization

Total phospholipid was quantified using Bartlett inorganic phosphate assay[6,7]. In brief, blocks were heated 180-200 °C before placing the disposable culture tubes (20 x 150

mm). All samples were used in triplicate. Control samples were used with serial concentrations of phosphate solution (0.13, 0.0975, 0.062, 0.0325 µmol, and no phosphate). A volume of 400 µl of 10N H_2SO_4 (sulfuric acid) solution was added to each tube and heated for 1 h at 180-200 °C. Tubes, then, were removed and cooled to room temperature. 100 µl of 30% (v/v) H_2O_2 (hydrogen peroxide) was added to each tube, vortexed after each addition, and heated for about 1 h or until all peroxide had been digested (peroxide digestion test is using semi-quantitative test strips from Quantofix, Macherey-Angel, Germany). The tubes, then, were removed and cooled to room temperature. A water bath was heated to a rolling boil (100 °C) while waiting for the tubes to cool. The tubes were boiled for 7-10 min, then removed and cooled to room temperature. A 150 µl sample was pipetted from each tube into a 96 well-plate. The absorbance for each well was obtained at 830 nm using SpectraMax iD3 multimode plate reader with SoftMax Pro 7.1 software.

Liposome size of distribution, electrophoretic mobility, and zeta potential were measured using Dynamic Light Scattering (DLS) (Nano-ZS, Malvern Instrument Inc., Westborough, MA) with Zetasizer 7.12 software. In brief, all samples were collected immediately after the dialysis step. Liposome suspensions were vortexed, pipetted 10 µL into 2 mL microcentrifuge tubes (cent. tube), 1 mL of deionized water was added to the cent. tube, vortexed, and the suspension was loaded into DTS1070 capillary cell obtained from Malvern Instrument Inc., Westborough, MA. The size of distribution, electrophoretic mobility, and zeta potential were measured using the same sample in the capillary cell. The size of distribution was measured first, and the results were expressed in intensity and volume-weighted measurements. When DLS is used to measure the size

of distribution, the first parameter it measures is the intensity distribution, which is measured according to the scattering intensity of each particle fraction or family, and other parameters are acquired using different equations depending on the polydispersity index (PDI). The DLS, then, measures the volume of distribution, which assumes a spherical mass of material[8]. Later, electrophoretic mobility and zeta potential were measured.

PI loading in liposomes was determined experimentally. There is no published protocol to quantify PI dissolved in pure ethanol, which liposomes were dissolved in to release the encapsulated PI[9]; therefore, we developed a method to identify PI maximum absorbance and the limit of quantification (LOQ). In brief, standards were prepared by dissolving free PI in ethanol (1 mM) and sonicated for 10 min. When a clear solution was obtained, serial concentrations of PI were prepared (500, 250, 125, 62.5, 31.25, 15.62, 7.8, 3.9, 1.9, 0.9, and 0 mM pure ethanol) in the same solvent (pure ethanol). Samples were analyzed by transferring 150 µl of each concentration into 96 well-plate. The absorbance spectrum was run using one of the PI samples diluted in ethanol from 400 to 1,000 nm to identify the maximum absorbance; then, all other PI samples were also run from 400 to 600 nm using SpectraMax iD3 plate reader with SoftMax Pro 7.1 software. A standard curve was obtained to identify the LOQ and the CV% (coefficient of variation) using the same plate reader.

A sample of PI and PI-free liposomes at the same lipid concentrations were added to pure ethanol (dilution of liposomes in pure ethanol, 1 in 5 ratio (v/v)), sonicated for 1 h or until a clear solution was obtained. When a clear solution was obtained, 150 µl aliquot was pipetted into a well of a 96 well-plate. The absorbance of each well was determined

using a plate reader, and the PI concentration was quantified by comparing the absorbance for each sample to the standard curve.

The PI-recovery % was calculated as follows:

$$\boldsymbol{PI - Recovery}\ (\%) = \frac{Final\ PI\ conccentration}{Initial\ PI\ concentration} \times 100$$

The encapsulation efficiency (EE) was calculated as follows:

$$\boldsymbol{EE} = \frac{Final\ lipid\ concentration}{Final\ PI\ concentration} / \frac{Initial\ lipid\ concentration}{Initial\ PI\ concentration}$$

2.6 PI-Liposome Stability

Leakage of PI from liposomes was determined in serum-supplemented media at 37 °C to simulate biological conditions. Studies were conducted immediately after PI-liposome preparation. Initial samples were collected immediately after dialysis and before beginning experiments and considered to have 100% encapsulated PI concentration at time 0. Formulations were then loaded into new dialysis bags and immersed in 37 °C DMEM without phenol red to avoid interference in sample readings, supplemented with 10% FBS, and placed on a stir plate with a stir bar (low speed). Samples (50µl) were collected from dialysis bags at different time points (5, 24, 48, and 72 h), and media was changed at every time point to retain the "sink condition". Absorbance intensity of PI was measured as described above, 2.5 Liposome Characterization.

2.7 *In-vitro* Cytotoxicity (MTT)

The cytotoxicity of liposomes and free PI on PC-3 cells was determined by measuring mitochondrial enzyme activity (MTT)[10,11]. MTT is a tetrazolium salt (3-(4,5-dimethylthiazol-2-yl)-2,5-diphenyltetrazolium bromide, and it is a colorimetric assay meant to measure cellular metabolic activity by the cleavage of tetrazolium ring by dehydrogenases in active mitochondria of living cells[10]. In brief, a stock solution of MTT was prepared (13.2mM in 1X PBS). After PC-3 cells were passaged, cells were collected and evaluated with viability >95% using trypan blue (described earlier) to proceed with the experiment. Cells were seeded (5,000 cells/well) in 96 well-plates. When cells reached ~90% confluence, washed with 1X PBS three times, liposomes and free PI were added (100µl total volume per well) in different concentrations (Liposomes; Lipid at 5, 2.5, 1.25, 0.625, and 0.3125 µM, and free PI at 125, 62.5, 31.25, 15.6, 7.8, and 3.9 µM) with complete growth media (F-12K) and incubated for 48 h. After 48 h, 10 µl of the MTT solution was added (final concentration 0.5 mg/ml) over each well and incubated for 2 h at 37 °C. After 2 h, reagents were aspirated from all wells, and 200 µl of DMSO was added to each well. Absorbance was measured at 544 nm using the plate reader, as described above. Untreated (control) cells were considered 100% as no cytotoxicity effect[11–13]. Three studies (n=3) were performed with a total of 4 replicates for each concentration of lipid studied, and three studies (n=3) were performed with 8 replicates for each concentration of free PI studied[13].

2.8 Qualitative Uptake of PI-liposomes and Free PI *via* Live Cell Microscopy

2D monolayer cell culture: PC-3 cells were collected after passaging, and a viability test using trypan blue was measured (>95% cell viability to proceed with the experiment, describe earlier). 1ml of cells were seeded at $1.5x10^5$ cells/ml onto a 24 glass-bottom opaque cell culture plate until they reached ~90% confluence. Cells were washed with 1X PBS two times, then PI-liposomes and free PI were dosed (10 μM PI final concentration) and incubated over different time points (6, 12, 24, and 48 h). Cells were washed with 1X PBS two times; then, Calcein AM was added to wells for the overall concentration of 3 μM with complete growth media for 30 min to stain live cells. Cells were washed and incubated with ice-cold 1X PBS for imaging.

3D mono-culture spheroids: PC-3 spheroids were prepared as described above, 2.3 3D spheroid preparation. PI-liposomes and free PI were dosed after days of the spheroids' growth and incubated for 48 h. Then, the same process was proceeded as in 2D monolayer cell culture samples (n =3 wells/group). Three areas with approximately equal cell densities were identified in each well, and images were captured with an Agilent Cytation5 digital cell imaging system (BioTek, USA) using a 4X objective. A Texas Red (559-34 ex, 630-69 em, and 585 DM pass band) filter was used to capture the image. Images were analyzed using ImageJ software https://imagej.nih.gov/ij/ in a double-blind manner. The cellular uptake was visualized as red for PI staining through the laser channel Texas red with 20X power lenses. Once PI is bound to nucleic acids, its basic fluorescence is enhanced 20- to 30-fold and can be detected using fluorescence measurements[14].

2.9 Uptake of PI-liposomes and Free PI in 3D Spheroids *via* Confocal Imaging

Spheroids were prepared with PC-3 cells expressing enhanced GFP + CAFs (no tag) and grown for nine days (n =3 wells/group) as described earlier. PI-liposomes and free PI were dosed (10 µM PI final concentration) at 2 and 7 days after initiation of growth and incubated for 48 h. At the completion of the study, all cells were stained with Hoechst 33342 (blue) dye (10 µM, for 1h), so CAFs could be estimated by fluorescence imaging [Total Cells (blue) – GFP tag PC-3 Cells (green)]. Each spheroid (control vs. treated) was placed on a CoverWell™ Imaging chamber which is designed to stabilize and support thick and free-floating specimens for confocal microscopy imaging. Individual images and Z-stacks were obtained using Nikon Eclipse C1 2000-E confocal microscope with Nikon EZ-C1 3.91 software that has 5 filter cubes. The lasers used were DAPI (404nm), FITC (488nm), and TRITC (561nm). Images were captured using 10X power lenses. When Z-stacks were acquired, top and bottom layers of spheroids were identified manually, and the gap between two subsequent was ~0.45µm. In brief, PC-3 GFP (green) transfected cells and all cells (blue) were acquired via confocal fluorescence imaging. Fiji ImageJ version 2.3.0 software (https://imagej.net/software/fiji/) was used to analyze and count cells. The analysis started by choosing the channels colors used in the images, channels were split, a layer was selected, a threshold was applied to separate cells from background pixels, a watershed was applied to split cells, and an automated count was applied to count the cells. PC-3 GFP (green) cells were subtracted from Hoechst 33342 (blue) dye after analysis.

2.10 Uptake of PI-liposomes and Free PI Uptake and 3D Spheroid *via* Flow Cytometry

2D monolayer cell culture: cells were seeded in 24 well plates until they reached ~90% confluence (*n* =3 wells/group) as described earlier. Cells were washed with 1X PBS, then PI-liposomes and free PI were dosed (10 µM PI final concentration) and incubated over different time points (24 and 48h). Cells were washed with 1X PBS; then Calcein AM was added to overall wells at 3 µM for 30 min to stain live cells. Cells were detached from the plate using trypsin and pelleted using the centrifuge 400xg for 10 min. Pellets were rewashed with PBS. All samples were filtered to prevent clogging using FLOWMI cell strainers (SP-Bel-Art, Wayne, NJ) right before analysis using BD Accuri C6 Plus flow cytometry and BD Accuri™ C6 Plus version 1.0.27.1 software. The BD Accuri C6 Plus Flow Cytometer has two excitation lasers (488 and 640 nm) and 4 emission detection filters. Live cell populations were gated by the FITC channel (filter 533/30 nm), selecting for Calcein AM fluorescence. Then, PI uptake was measured using the PerCP channel (filter 610/20 borrowed from Flow Cytometry Laboratory, College of Veterinary Medicine, Auburn University, AL).

3D mono-culture spheroids: spheroids were prepared and grown for two days, as described earlier. A total of 12 spheroids for each group were dosed with PI-liposomes and free PI (10 µM PI final concentration) and incubated over different time points (6, 12, 24, and 48 h) (*n* =3/cohort). Each group of 12 spheroids was collected in 1.8 mL microcentrifuge tubes, pelleted, washed with PBS, and Calcein AM was added (3 µM for 30 min) to stain live cells. Spheroids were washed with PBS and then dissociated by adding 600 µL of Accumax (0.5 to 1 h in a shaker at room temperature). Mechanical

dissociation was also achieved using 1,000 µL pipette microtips. Another 600 µL of 10% (v/v) FBS supplemented F-12K media was added to the cell suspension to deactivate the Accumax effect. Cells were pelleted, washed, and incubated with PBS. All samples were filtered using FLOWMI cell strainer immediately before analysis using BD Accuri C6 Plus Flow Cytometer, as described above. All samples and controls are described in Table 2.2.

3D co-culture spheroids: spheroids were prepared and grown for nine days, as described above. A total of twenty spheroids for each group were dosed with PI-liposomes and free PI (10 µM PI final concentration) at different time points (after 2 and 7 days of growth) and incubated for 48 h (*n* =3/cohort). Each group of 20 spheroids was collected into 1.8 mL microcentrifuge tubes, pelleted, washed with 1X PBS, and dissociated with the addition of 600 µL of Accumax (0.5 to 1 h at room temperature). Mechanical dissociation was also achieved using 1,000 µL pipette microtips. Another 600 µL of 10% (v/v) FBS supplemented F-12K media was added to the cell suspension to deactivate the Accumax effect. Cells were pelleted, washed with 1X PBS followed by incubation with a mixture of a blocking [2.5% (v/v) of Fc blocker 0.5% (w/v) bovine serum albumin (BSA)] buffer to eliminate nonspecific antibody binding staining. Fc blocker was added to samples (100 µL, 20 min at room temperature). Cells were pelleted, and ghost dye (GD) red (ex/em 633/780 nm) was added to desired samples (500 µL, 0.1% (v/v) of GD in staining/antibody diluting buffer- 0.5% (w/v) BSA, 30 min at 4 °C, protected from light). Cells were pelleted, washed, and EpCAM Alexa Fluor® 647 conjugate was added to desired samples (100 µL, 1% (v/v) of EpCAM in staining/antibody diluting buffer - 0.5% (w/v) BSA, 1 h at 4 °C, protected from light).

Samples were washed, then filtered using a FLOWMI cell strainer right before analysis using CytoFLEX LX Flow Cytometer. The CytoFLEX LX flow cytometry has 6 lasers (375, 405, 488, 561, 638, and 808 nm) and 21 fluorescent color channels. All samples and controls are described in Table 2.3. Flow Cytometry data were analyzed by FlowJo version 10.8.1 software https://www.flowjo.com/. Samples were analyzed by gating live cell populations using the APCA750 channel for ghost dye. Populations were split between +ve EpCAM and -ve EpCAM using the APC660 channel, then PI uptake was identified by each population using the mCHERRY610 channel. Unstained samples were used to identify the right gating regions and differentiate them from the stained samples.

2.11 Tumor mRNA Sequencing (RNA-seq)

RNA isolation: 2D PC-3 cells, 3D PC-3 spheroids, and 3D multicellular co-culture spheroids PC-3+CAF were harvested, and cell pellets were collected after cell dissociation (described earlier). Cell pellets were washed with 1X PBS and stored in RNA stabilization reagent (Qiagen RNAlater™) at -80 °C. RNA stabilization is an absolute prerequisite for reliable gene expression analysis. Immediate stabilization of RNA in biological samples is necessary because, directly after harvesting the samples, changes in the gene expression pattern occur due to specific and nonspecific RNA degradation and transcriptional induction. Such changes need to be avoided for all reliable quantitative gene expression analyses, such as quantitative RT-PCR and RNAseq technologies. High-quality RNA was extracted using QIAshredder and RNeasy kit (Qiagen) according to the manufacturer's protocol[15]. Samples were first lysed and homogenized in the presence of a highly denaturing guanidine-thiocyanate–containing buffer, which immediately inactivates RNAses to ensure purification of intact RNA.

Ethanol was added to provide appropriate binding conditions, and the sample was then applied to an RNeasy Mini spin column, where the total RNA bound to the membrane and contaminants were washed away. High-quality RNA was then eluted in 30–100 µL of elution buffer. With the RNeasy procedure, all RNA molecules longer than 200 nucleotides were purified. The procedure provides enrichment for mRNA since most RNAs <200 nucleotides (such as 5.8S rRNA, 5S rRNA, and tRNAs, which comprise 15–20% of total RNA) are selectively excluded[15].

The effects of delivery system exposure on gene expression in PC-3 cell lines (2D and 3D) and multicellular co-culture PC-3+CAF were assessed using next-generation RNA sequencing of 2D PC-3 cells, 3D PC-3 spheroids, and 3D multicellular co-culture spheroid PC-3+CAF followed by conventional and PEGylated liposomes without PI incubation for 48h. Cells were harvested, and high-quality RNA will be extracted using QIAshredder and RNeasy kit (Qiagen) according to the manufacturer's protocol as described earlier[15].

RNA Quantification: RNA concentration and integrity were assessed using Nanodrop-8000 spectrophotometer (Thermo Scientific, USA), Qubit 2.0 Fluorometer (Invitrogen, Carlsbad, CA, USA), and Agilent 2100 Bioanalyzer (Applied Biosystems, Carlsbad, CA, USA) and stored at -80 °C. An RNA integrity number (RIN; ratio of 28S:18S ribosomal RNA) threshold >8 was applied[15,16].

mRNA sequencing: RNA-seq libraries were constructed using Illumina TruSeq RNA Sample Preparation kit v2. Libraries were then size-selected to generate inserts of ~200 bp, and RNA sequencing was performed on Illumina's NovaSeq platform using a

150bp paired-end protocol with a depth of > 20 million reads per sample. Average quality scores were thoroughly above Q30 for all libraries in both R1 and R2[15].

RNAseq data analysis: RNA-seq data (described above) was pre-processed and normalized, and differential expression (DE) analysis was performed using a command-line-based analysis pipeline (DEseq2 and edgeR) and Partek Flow software (Partek, Inc, USA). Quality control (QC) check on the RNA-seq raw reads was performed using the FastQC tool, followed by read-trimming to remove base positions that have a low median (or bottom quartile) score. STAR Aligner tool mapped processed RNA-seq reads to the hg38 human genome build. Next, read counts were CPM-normalized, and then we used GSA (Gene-specific analysis) based on limma trend, that applies an empirical Bayesian method, to perform differential gene expression analysis between groups and detect the DE genes. Genes with mean fold-change >|1| and $p<0.05$ were considered as the threshold for reporting significant differential gene expression. Heatmaps were generated using unsupervised hierarchical clustering (HC) analysis based on the differentially expressed genes (DEGs)[15].

2.12 Statistical Analysis

All statistical analyses were performed using GraphPad Prism (version 5.0). A two-way ANOVA and multiple comparisons post-test were used for confocal imaging and flow cytometry results. Any difference with a P-value < 0.05 was considered statistically significant. All images were analyzed by ImageJ software, all confocal images were analyzed by Fiji ImageJ, and flow cytometry data were analyzed by FlowJo version 10.8.1 software[12,15].

Spheroids	***Cells***	***Media***	***Ratio (cell:cell)***
Mono-culture	*PC-3*	*F-12K*	*1*
Co-culture	*PC-3 + CAFs*	*F-12K + CCM*	*1:1*

Table 2.1. Types of spheroids used in all experiments with cells, media, and ratio specifications.

Sample	Calcein AM	Free PI	PI-Conventional	PI-Pegylated
Control	–	–	–	–
Calcein AM	Yes	–	–	–
Free PI	–	Yes	–	–
Free PI + Calcein AM	Yes	Yes	–	–
PI-conventional + Calcein AM	Yes	–	Yes	–
PI-PEGylated + Calcein AM	Yes	–	–	Yes

Table 2.2 *2D monolayer cell culture* and *3D monocellular spheroid* samples tested by flow cytometry.

Sample	GD	EpCAM	Free PI	PI-Conventional	PI-PEGylated
Control co-culture spheroids	–	–	–	–	–
Ghost Dye (GD)	Yes	–	–	–	–
EpCAM	–	Yes	–	–	–
GD + EpCAM	Yes	Yes	–	–	–
Free PI	–	–	Yes	–	–
Free PI + GD +EpCAM	Yes	Yes	Yes	–	–
PI-conventional	–	–	–	Yes	–
PI-conventional + GD + EpCAM	Yes	Yes	–	Yes	–
PI-PEGylated	–	–	–	–	Yes
PI-PEGylated + GD + EpCAM	Yes	Yes	–	–	Yes

Table 2.3. *3D co-culture spheroids* tested by flow cytometry.

2.13 Figures Legends

Figure 2.1. Structure of Propidium Iodide

PI (dark red solid) is a fluorescent intercalating agent that can be used to stain cells and nucleic acids., molecular weight 668.4, hydrogen bond donor count 2, hydrogen bond acceptor count 4, and rotatable bond count is 7.

Figure 2.2. Liposome Phospholipids and Cholesterol structures.

DSPC is Distearoylphosphatidylcholine. DSPE-mPEG-2000 is 1,2-distearoyl-sn-glycero-3-phosphoethanolamine-N-[methoxy(polyethyleneglycol)-2,000].

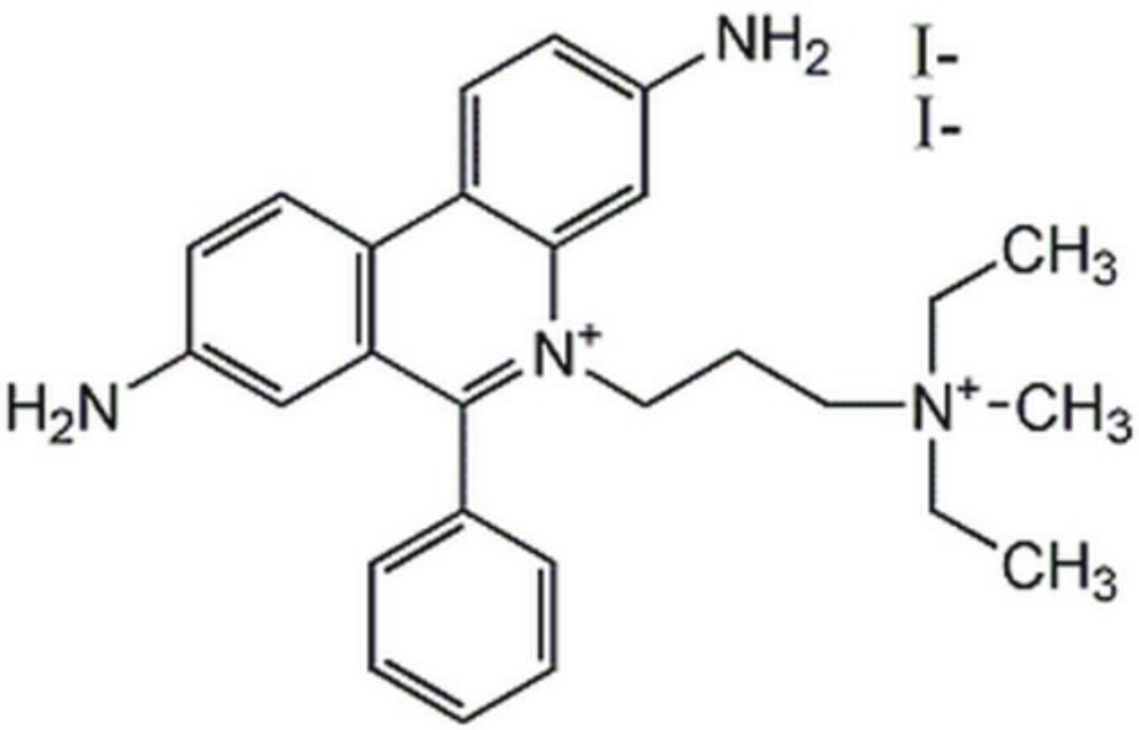

Figure 2.1

DSPC

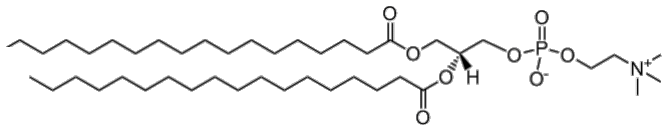

DSPE-mPEG-2000

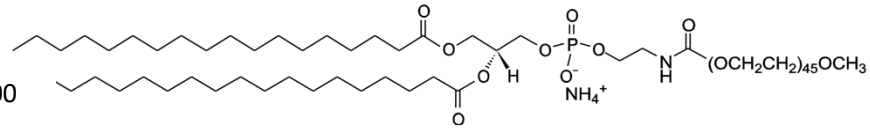

Cholesterol

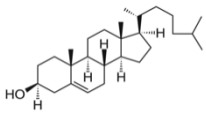

Figure 2.2

2.14 References:

1. Kaur SP, Verma A, Lee HK, Barnett LM, Somanath PR, Cummings BS. Inhibition of glypican-1 expression induces an activated fibroblast phenotype in a human bone marrow-derived stromal cell-line. *Sci Rep*. 2021;11(1):1-14. doi:10.1038/s41598-021-88519-7
2. Carlsson J, Yuhas JM. Liquid-overlay culture of cellular spheroids. *Recent results cancer Res Fortschritte der Krebsforsch Prog dans les Rech sur le cancer*. 1984;95:1-23. doi:10.1007/978-3-642-82340-4_1
3. Min S, Choe C, Roh S. Aqp3 increases intercellular cohesion in nsclc a549 cell spheroids through exploratory cell protrusions. *Int J Mol Sci*. 2021;22(8). doi:10.3390/ijms22084287
4. Cummings NDQMWERDABS. 2014 Role of PLA2 Receptor in Liposome in PSA.pdf.
5. Quach ND, Mock JN, Scholpa NE, et al. Role of the phospholipase A2 receptor in liposome drug delivery in prostate cancer cells. *Mol Pharm*. 2014;11(10):3443-3451. doi:10.1021/mp500174p
6. BARTLETT GR. Phosphorus assay in column chromatography. *J Biol Chem*. 1959;234(3):466-468. doi:10.1016/s0021-9258(18)70226-3
7. Mock JN, Costyn LJ, Wilding SL, Arnold RD, Cummings BS. Evidence for distinct mechanisms of uptake and antitumor activity of secretory phospholipase A $_2$ responsive liposome in prostate cancer. *Integr Biol*. 2013;5(1):172-182. doi:10.1039/C2IB20108A
8. Malvern Instruments. Calculating Volume Distributions From Dynamic Light

Scattering Data. *Tech Note*. 1(www.malvern.com):1-4. www.malvern.com.

9. Perrie Y, Webb C, Khadke S, et al. The impact of solvent selection: Strategies to guide the manufacturing of liposomes using microfluidics. *Pharmaceutics*. 2019;11(12). doi:10.3390/pharmaceutics11120653

10. Liu Y, Peterson DA, Kimura H, Schubert D. Mechanism of cellular 3-(4,5-dimethylthiazol-2-yl)-2,5-diphenyltetrazolium bromide (MTT) reduction. *J Neurochem*. 1997;69(2):581-593. doi:10.1046/j.1471-4159.1997.69020581.x

11. Mitra Ghosh T, White J, Davis J, et al. Identification and Characterization of Key Differentially Expressed Genes Associated With Metronomic Dosing of Topotecan in Human Prostate Cancer. *Front Pharmacol*. 2021;12(December):1-19. doi:10.3389/fphar.2021.736951

12. Aljuffali IA, Mock JN, Costyn LJ, et al. Enhanced antitumor activity of low-dose continuous administration schedules of topotecan in prostate cancer. *Cancer Biol Ther*. 2011;12(5):407-420. doi:10.4161/cbt.12.5.15950

13. Mosmann T. Rapid colorimetric assay for cellular growth and survival: application to proliferation and cytotoxicity assays. *J Immunol Methods*. 1983;65(1-2):55-63. doi:10.1016/0022-1759(83)90303-4

14. Kulkarni SA, Feng SS. Effects of particle size and surface modification on cellular uptake and biodistribution of polymeric nanoparticles for drug delivery. *Pharm Res*. 2013;30(10):2512-2522. doi:10.1007/s11095-012-0958-3

15. Mitra Ghosh T, Kansom T, Mazumder S, et al. The Andrographolide Analogue 3A.1 Synergizes with Taxane Derivatives in Aggressive Metastatic Prostate Cancers by Upregulation of Heat Shock Proteins and Downregulation of MAT2A-

Mediated Cell Migration and Invasion. *J Pharmacol Exp Ther*. 2022;380(3):180-201. doi:10.1124/jpet.121.000898

16. Schroeder A, Mueller O, Stocker S, et al. The RIN: an RNA integrity number for assigning integrity values to RNA measurements. *BMC Mol Biol*. 2006;7:3. doi:10.1186/1471-2199-7-3

CHAPTER 3

RESULTS

3.1 PI-Liposomes Characterizations

3.1. A. PI Loading in Liposomes:

The optimal loading concentration of PI was determined colorimetrically. PI was loaded into liposome formulations at 1, 0.5, and 0.25 mM concentrations to 10 mM phospholipid. An absorbance spectrum of PI diluted in PI was run with a wide range of 400 to 1,000 nm to identify the maximum absorbance (Figure 3.1). Another absorbance spectrum was run using different PI concentrations and identified the lower limit of detection (LOD) of PI (3.9 μM) (Figure 3.2). The overall linear range of the assay was 0.97 to 500 μM, linear (r^2) = 0.999, limit of quantification (LOQ) of the PI is 7.8 μM, with +/-10% accuracy and CV% <15% (Table 3.1). The concentration of PI in each liposome formulation was determined by constructing a standard curve of PI dissolved in absolute ethanol (>99% v/v) and measuring the absorbance at 545 nm (Figure 3.3). It was noted that PI concentrations of 0.25 mM were below the LOQ, so it was not considered. At PI loading of 1 and 0.5 mM, the percent recovery was ~12% for the conventional and PEGylated liposomes (Table 3.2). Moreover, the encapsulation efficiency (EE) for the 1 mM PI was 8.3 ± 2.42% with final PI:lipid (mole ratio) 0.12:10, and the EE for the 0.5 mM PI was 10.18 ± 4.63% with final PI:lipid (mole ratio) 0.06:10. Therefore, based on the mole basis ratio, 1 mM of PI was used for further experiments.

3.1. B. Liposome Size Distributions, Zeta Potentials, and Electrophoretic Mobility:

The effect of PI on size distribution, zeta potential, and electrophoretic mobility of conventional and PEGylated liposomes was determined. Utilizing the thin-film hydration method produced liposome formulations with narrow size distributions. Figure 3.4 shows the difference between the Conventional and PEGylated liposomes with and without PI

and compares intensity and volume size distribution measurements. The conventional liposomes with and without PI intensity and volume size distributions were 120-140 nm and 105-125 nm, respectively. The PEGylated liposomes with and without PI intensity and volume size distributions were 125-145 nm and 110-130 nm, respectively. When liposomes were loaded with PI, they did not show a consistent increase in the size distribution compared to the liposomes that have no PI.

The zeta potential of the liposome formulations was measured to determine the charge and potential impact of stability in solution. The zeta potential for the conventional liposomes with and without the PI were in the same range of 20 ± 2 mV, and the PEGylated liposomes with and without the PI were in the same range of -28 ± 2 mV. The zeta potential was not showing a consistent effect after loading PI into the liposomes. Moreover, the PEGylated liposomes are showing higher zeta potential compared to the conventional liposomes; which means that the PEG increased the stability of the PEGylated liposomes.

Figure 3.5 compares between the liposomes' zeta potential with and without the PI. The results showed that the PI did not affect the zeta potential in a consistent manner, where sometimes it gave the same value and other times higher or lower values; however, the all values are consistent in the same range (conventional liposomes are 20 ± 2 mV, PEGylated liposomes are -28 ± 2 mV). We compared the stability of the conventional and PEGylated liposomes after 72 h exposure to biological conditions (serum-supplemented media at 37°C). In Figure 3.6 the results showed no difference between the liposomes when loaded with PI or not; therefore, we only reported the difference in stability between the conventional and PEGylated liposomes in general. Electrophoretic

mobility measures the charges of the particles. The conventional liposomes' charge was 1.5 ± 0.15 μmcm/Vs and the PEGylated liposomes' charge was -2 ± 0.15 μmcm/Vs. Table 3.3 compares the liposome formulations' size distributions, zeta potentials, and electrophoretic mobility before and after 72 h exposure to biological conditions. The intensity size distributions of the conventional liposomes after 72 h increased by 22%, whereas the PEGylated liposome size increased by 0.6%. The zeta potentials for the conventional liposomes changed from 20 ± 2 to -4.5 ± 2.6 mV, whereas the PEGylated liposomes changed from -29 ± 2 to -19.4 ± 2 mV. The conventional liposomes' electrophoretic mobility was 1.5 ± 0.15 and changed to -0.3 ± 0.25 μmcm/Vs, whereas the PEGylated liposomes' electrophoretic mobility was -2 ± 0.15 and changed to -1.5 ± 0.2 μmcm/Vs.

3.2 PI Stability in Liposomes

To evaluate the PI stability in the conventional-PI and PEGylated-PI liposomes, they were tested in biological conditions (serum-supplemented media at 37°C) for 72 h. Samples were collected at different time points (0, 5, 24, 48, and 72 h). The 0 time-point samples were collected immediately before the stability experiments started. We considered the 0 time-point as 100% encapsulated PI. A free PI sample was included in the experiments to examine its leakage from the dialysis bags. We observed that 100% of the free PI leaked out after 5 h (the first time-point after we started the stability studies). When samples were collected (50 μl) from the dialysis bags, they were dissolved in pure ethanol (total volume 250 μl) and analyzed to identify PI concentrations, as described earlier.

The results showed a gradual release (15%) of the PI from the conventional-PI liposomes over 72 h. . The PEGylated-PI liposomes showed an initial release of 15% of the PI over the 5 h (the first time-point), but further PI release over the 72 hours was not observed (Figure 3.7). Overall, the conventional-PI and PEGylated-PI liposomes showed stability of 85% of the encapsulated PI until 72 h at 37 ^{o}C and in the presence of serum.

3.3 *In-vitro* Cytotoxicity (MTT)

To determine the cytotoxicity of the formulations (free PI, conventional-PI liposomes, and PEGylated-PI liposomes) used in our studies, we measured mitochondrial enzyme activity (MTT)[1–3]. The assay measures the cellular metabolic activity by the cleavage of tetrazolium ring by dehydrogenases in active mitochondria of living cells[1].

Propidium iodide (PI): PI is a stain used commonly to identify dead cells. PI is widely known to cross only damaged cell membranes; however, we demonstrated it was able to cross intact cells membrane upon incubation for longer time periods (>6 h). We determined the effect of free PI on the *in-vitro* metabolic activity of PC-3 cells following 48 h exposure to different PI concentrations (125, 62.5, 31.25, 15.6, 7.8, and 3.9 µM). A concentration response curve was prepared and showed that little to no toxicity was seen by 10 µM up to 15 µM and above that we saw increasing toxicity, as shown in Figure 3.8. The goal of using PI in this project was to understand liposome uptake and intra-tumor distribution within cancer cells. To minimize the potential for cellular toxicity mediated by PI, a concentration of 10 µM was used in further experiments.

Liposomes: The cytotoxicity of empty liposomes (without PI) was also measured using MTT. The effect of liposomes on the *in-vitro* growth of PC-3 cells following 48 h exposure to different lipid concentrations (5, 2.5, 1.25, 0.625, and 0.3125 mM) was

determined. The results showed no evidence of cytotoxicity (alteration in MTT staining) following incubation with conventional and the PEGylated liposomes for 48 h, as shown in Figure 3.9.

3.4 Qualitative Uptake of PI-liposomes and Free PI *via* Live-Cell Microscopy

The aim of the microscopic evaluation was to visualize distribution. To demonstrate that PI can be used to visualize liposome uptake, we exposed cells to 10 μM free PI for 24 h, and we were able to capture the PI (red color) with a Texas red laser (596/615 ex/em) in live cells and co-staining live cells with 3 μM of Calcein AM 30 min before the images were taken (Figure 3.10). Calcein AM fluorescence was captured using a FITC laser (490/525 ex/em). A Cytation™5 cell imaging Multi-Mode Reader was used to capture the images.

***2D monolayer cell culture*:** The uptake of PI was determined after the exposure of free PI, conventional-PI, and PEGylated-PI (PI final concentration was 10 μM) at 6, 12, 24, and 48 h. Images are shown in a bright field (BF) with Texas red (TR) to better visualize the PI, pseudocolored a red color. TR images are showing only the PI channel. FITC images are merged with BF and TR to show the uptake in live cells, as described earlier. Evidence of free PI uptake was observed after 6 h exposure, which increased over time, as shown in Figure 3.11. The conventional PI-liposomes showed low uptake of PI in all-time points observed, as shown in Figure 3.12. The PEGylated liposomes showed uptake at 48 h, as shown in Figure 3.13.

***3D mono-culture spheroids*:** We compared the uptake of PI-liposomes and free PI in 2D monolayer cell culture model, to a more physiologically relevant 3D mono-culture spheroid model. Spheroids were grown for 2 days before the treatment was added. Free

PI, conventional-PI, and PEGylated-PI were dosed at the same final PI concentrations as in the 2D monolayer cell culture experiments. The images were captured after different time points (6, 12, 24, and 48 h). Free PI showed uptake at 6 h and further time points, as shown in Figure 3.14. The conventional liposomes showed no uptake at all-time points, as shown in Figure 3.15. The PEGylated liposomes showed higher uptake at 48 h than the conventional liposomes, as shown in Figure 3.16. As we visualized the PI in those images, we followed up these experiments with Flow cytometry to quantify the PI uptake.

3.5 3D Spheroids Growth *via* Confocal Imaging

3D mono-culture and co-culture spheroids' growth was evaluated using confocal imaging. The mono-culture spheroids were growing uncontrollably and fast, reaching 30,000 cells by count after 9 days, as shown in Figure 3.17. On the other hand, the co-culture spheroids were growing slowly and resembling solid tumors, and they reached a maximum of 8,000 cells by count after 9 days, as shown in Figures 3.18 and 3.19. One of the comparisons was the size change between mono-culture and co-culture spheroids after 2 and 7 days of growth. The mono-culture spheroids were significantly larger than the co-culture spheroids, as shown in Figure 3.20.

3.6 PI-liposomes and Free PI Uptake *via* Confocal Imaging

Scanning fluorescence confocal microscopy offers more advantages over conventional fluorescence and brightfield imaging, including control depth of field, reduction of background, and the ability to collect Z-stack sections from 3D objects[4]. Therefore, we used confocal imaging microscopy to better visualize the 3D spheroids and identify the uptake in different regions of the spheroids. To capture the images using confocal

microscopy, we used PC-3 cells that constitutively express enhanced green fluorescence protein (eGPF)[5]. CAFs were not tagged with any fluorescent probe; thus, we used Hoechst 33342 dye, which stains all cells' nuclei and has been used in the literature for staining and evaluating 3D spheroids using confocal imaging[6].

The uptake of PI-liposomes and free PI in 3D spheroids was measured in two regions (surface or tumor periphery and the center) to gain insights into how distribution and uptake can be altered spatially within a tumor spheroid. After two and seven days of the spheroid growth, free PI, conventional-PI, and PEGylated-PI (PI final concentration is 10 μM) were incubated with the spheroids for 48 h. At completion of the study, Hoechst 33342 dye was incubated with the 3D co-culture spheroids at a final concentration of 10 μM for 1 h.

Surface Uptake: When the formulations were dosed after 2 days of spheroid growth, the free PI, conventional-PI liposomes, and PEGylated-PI liposomes showed significantly (P<0.05) greater uptake in 3D mono-culture (PC-3) spheroids (mean ± SEM = 10500 ± 764, 2430 ± 233, 2200 ± 115, respectively) compared to the 3D co-culture (PC-3 + CAFs) spheroids (mean ± SEM = 5070. ± 348, 600 ± 153, 933 ± 88.2, respectively). When the formulations were dosed after 7 days of spheroid growth, the free PI and conventional-PI liposomes also showed significantly (P<0.05) higher uptake in the 3D mono-culture spheroids (mean ± SEM = 10700 ± 882, 2230 ± 176, respectively) compared to the 3D co-culture spheroids (mean ± SEM = 54667 ± 290.59, 566.667 ± 291, respectively). The PEGylated liposomes showed higher uptake in the 3D mono-culture spheroids (mean ± SEM = 3070 ± 145) compared to the 3D co-culture spheroids (mean ± SEM = 1730 ± 120) but it was not significant.. The results showed the same

pattern of having higher uptake in the 3D mono-culture spheroids compared to the 3D co-culture spheroids after 2 and 7 days of the spheroids' growth (Figures 3.21).

Center Uptake: The uptake of PI in the center of the spheroid after 2 days of growth showed significantly higher uptake of the PEGylated liposomes in the 3D mono-culture (PC-3) spheroids (mean ± SEM = 3070 ± 120) compared to the 3D co-culture (PC-3 + CAFs) spheroids (mean ± SEM = 1230 ± 145), the free PI showed a little higher uptake in the 3D mono-culture spheroids (mean ± SEM = 5170 ± 145) compared to the 3D co-culture spheroids (mean ± SEM = 4570 ± 233) but not significant, and the conventional-PI liposomes showed almost similar uptake between the 3D mono-culture and co-culture spheroids (mean ± SEM = 1170 ± 145, 1200 ± 173, respectively). The uptake after 7 days of the spheroids' growth of the free PI showed no significant difference between the 3D mono-culture and co-culture spheroids (mean ± SEM = 7470 ± 433, 5970 ± 895, respectively), the conventional-PI showed no significant difference between the 3D mono-culture and co-culture spheroids (mean ± SEM = 1870 ± 88.2, 1030 ± 88.2, respectively), and the PEGylated-PI showed no significant difference between the 3D mono-culture and co-culture spheroids (mean ± SEM = 3770 ± 145, 2130 ± 176, respectively) (Figure 3.22).

3.7 PI-Liposomes and Free PI Uptake *via* Flow Cytometry

Flow cytometry is a technique that works by the light scattering and fluorescence emission as the specific fluorescent probe-labeled cells pass through a laser beam. It provides a multi-parametric analysis of cell populations at the single-cell level[7]. The PC-3 cells used in these experiments were not GFP tagged.

Identifying the uptake in *2D monolayer cell culture*: Calcein AM was used at 3 µM final concentration for 30 min to capture live cell populations and measured using the FITC fluorochrome (filter 533/30). The PI uptake was captured using PerCP fluorochrome (filter 610/20). The analysis was acquired using BD Accuri C6 Plus Flow Cytometer, and data were analyzed as recommended by the manufacturer using the BD Accuri™ C6 Plus version 1.0.27.1 software.

We determined the uptake of the free PI in live cells by incubating the free PI in different concentrations (20, 10, 5, 2.5, 1.25, and 0.62 µM), and the samples were collected after 24 and 48 h exposure. The results showed that the PI is concentration and time-dependent, as shown in Figure 3.23. The PI concentrations of 5 µM and higher presented significant (P<0.05) uptake when incubated with the cells after 24 and 48 h.

Identifying the uptake in *3D Mono-Culture Spheroids*: 3D mono-culture (PC-3) spheroids were dissociated and incubated with Calcein AM at a final concentration of 3 µM for 30 min to capture live cell populations at the FITC fluorochrome (filter 533/30). The PI uptake was captured using PerCP fluorochrome (filter 610/20). The analysis was acquired using BD Accuri C6 Plus flow cytometry, and data were analyzed using BD Accuri™ C6 Plus version 1.0.27.1 software.

Identifying the uptake in *3D co-culture spheroids*: in Figure 3.24, we used the 3D co-culture (PC-3 + CAFs) spheroids and we showed all the markers expressions in PC-3 and CAFs cells. EpCAM antibody showed as a specific marker for PC-3 cells. The results showed 97.5% of the PC-3 cells stained with EpCAM, whereas the CAFs cells showed only 6.3% of EpCAM stain.

One of the standardization assays was choosing the right blocking buffer to avoid non-specific binding. FBS (fetal bovine serum) blocker buffer helps to minimize the non-specific binding of antibodies [8]. Fc blocker buffer minimizes non-specific binding by blocking the Fc receptors found on the cells[9]. In Figure 3.25**,** we showed the difference between using FBS and Fc blocking buffers. Both buffers were diluted in 0.5% (w/v) BSA buffer. The FBS buffer concentration was 10% (v/v) of FBS in 0.5% (w/v) bovine serum albumin (BSA). The Fc blocker buffer concentration was 2.5% (v/v) of Fc blocker in 0.5% (w/v) bovine serum albumin (BSA). Both buffers were incubated with the cells for 20 min at room temperature. The results showed that the Fc blocking buffer provides higher blocking than the FBS. The antibody used in this experiment was the EpCAM marker.

In the 3D co-culture (PC-3 + CAFs) spheroids flow cytometry experiments, we used Ghost dye (GD) red (ex/em 633/780 nm) to exclude dead cells populations from the live cells populations. GD was added to desired samples (500 µL, 0.1% (v/v) of GD in staining/antibody diluting buffer- 0.5% (w/v) BSA, 30 min at 4 °C, protected from light). We also used the EpCAM antibody. EpCAM Alexa Fluor® 647 conjugate was added to desired samples (100 µL, 1% (v/v) of EpCAM in staining/antibody diluting buffer - 0.5% (w/v) BSA, 1 h at 4 °C, protected from light).

A gating strategy was provided to validate how the results were analyzed in Figure 3.26. EpCAM +ve was considered PC-3, and EpCAM -ve was considered CAFs and PC-3 with -ve EpCAM marker.

The target determination in our project is to identify the difference in the uptake of the liposome nanoparticles between the 2D monolayer culture, 3D mono-culture, and 3D co-

culture. Therefore, we compared the uptake of the free PI, conventional-PI liposomes, and PEGylated-PI liposomes between all the models in our project.

Dosing the formulations after 2 days of the spheroids' growth and identifying their uptake: after growing the 3D mono-culture (PC-3) and co-culture (PC-3 + CAFs) spheroids for two days and when the 2D monolayer cells were ~90% confluent, we incubated the free PI, conventional-PI liposomes, and PEGylated-PI liposomes at a final PI concentration of 10 μM for 48 h. In Figure 3.27, we showed significantly (P<0.05) lower uptake of the PEGylated-PI liposomes in the 3D mono-culture and 3D co-culture compared to the 2D monolayer culture model. There was no significant difference between the 3D mono-culture and 3D co-culture with the PEGylated-PI liposomes, and there was no significant difference between all kinds of culture models with the conventional-PI liposomes. The free PI uptake was significantly (P<0.05) lower in the 3D co-culture model compared to the 2D monolayer culture and 3D mono-culture.

Dosing the formulations after 7 days of the spheroids' growth and identifying their uptake: since the 2D monolayer (PC-3) culture model cannot grow for 7 days because of their fast confluence, we excluded that model from these experiments. We incubated the free PI, conventional-PI liposomes, and PEGylated-PI liposomes at a final PI concentration of 10 μM for 48 h. In Figure 3.28, we identified the difference in the uptake between the 3D mono-culture (PC-3) and 3D co-culture (PC-3 + CAFs) after growing the spheroids for seven days. After seven days, the PEGylated-PI liposomes significantly (P<0.05) showed lower uptake in the 3D co-culture compared to the 3D mono-culture. The free PI showed significantly (P<0.05) reduced uptake in the 3D co-culture than in the 3D mono-culture. The conventional-PI liposomes showed greater

uptake in the 3D co-culture compared to the 3D mono-culture, but it was not statistically significant.

Identifying the uptake between the *3D co-culture spheroids populations*: The 3D co-culture spheroids model has PC-3 and CAFs cells. We have used the EpCAM marker more specific to the PC-3 cells. Therefore, we identified the uptake between the PC-3 cells and the other populations (CAFs and EpCAM –ve PC-3). In Figure 3.29, the uptake of PI was measured after two and seven days of spheroids' growth. After two days of the spheroids' growth, the uptake was generally higher in the CAFs and EpCAM –ve PC3 cells populations, but the PEGylated liposomes had a significantly (P<0.05) greater uptake in the CAFs and EpCAM -ve PC-3 cells populations than EpCAM +ve PC3 cells populations. After seven days of the spheroids' growth, the uptake showed more in the EpCAM +ve PC-3 cells populations, which is the opposite of the two days. The only significant difference was the PEGylated-PI liposomes that showed greater uptake in the EpCAM +ve PC-3 cells.

3.8 3D Co-culture Spheroids Growth Change in (1:1) PC-3 and CAFs *via* Flow Cytometry

The growth difference between PC-3 and CAFs in co-culture was analyzed using flow cytometry. The gating strategy proceeded as described earlier but without considering the PI uptake gate because it was not dosed in the spheroids in these experiments. The growth was evaluated on days 0, 2, 4, 7, and 9 (day 0 was assessed to confirm the 1:1 ratio of PC-3 and CAFs). There was a significant (P<0.05) difference between CAFs and EpCAM -ve PC-3 cells populations and the other group (EpCAM +ve) after 4, 7, and 9

days of spheroid growth. We observed that the longer the co-culture spheroids grew, the lower the EpCAM +ve population percentage, as shown in Figure 3.30.

3.9 2D Monolayer Model RNA Sequencing Analysis

PC-3 2D cell line RNA sequencing was performed to identify baseline gene expression signature. Baseline Gene Expression Profile (GEP) identified DEGs for PC-3. Further, the top 100 (FDR<0.05, *P*<0.5) DEGs for PC-3 were the majority of EMT and Matrix metalloproteinase (MMPs) markers such as Vimentin/VIM, Hyaluronan Synthase-3/HAS3, S100 Calcium Binding Protein A6/S100A6, Epithelial Cell Adhesion Molecule EPCAM, Annexin A2/ANXA2, Annexin A2 Pseudogene-2/ANXA2P2, Lysyl Oxidase Like 2- LOXL2, Annexin A3/ ANXA3, Transforming Growth Factor Beta Receptor 2- TGFBR2, AHNAK Nucleoprotein 2- AHNAK2, Transforming Growth Factor Beta 1-TGFB1, Ubiquitin C-Terminal Hydrolase L1- UCHL1, CD55, CD44, CD109. Fascin Actin-Bundling Protein-1/FSCN1, a taxane-resistant gene, was also identified as the top DEG for PC-3 2D model subtypes (Table 3.4).

3.10 3D RNA sequencing analysis

PC-3 mono-culture 3D RNA sequencing was performed to identify the gene expression fold changes for top EMT and MMP markers compared with the PC-3 2D monolayer cell line model (Figure 3.31). Top DEGs for PC-3 3D was also the majority of EMT, cancer pathway hallmark genes, and matrix metalloproteinase (MMPs) markers such as vimentin (VIM), hyaluronan synthase-3 (HAS3,) S100 calcium binding protein A6 (S100A6), epithelial cell adhesion molecule (EPCAM), annexin A2 (ANXA2), annexin A2 pseudogene-2 (ANXA2P2), lysyl oxidase like 2 (LOXL2), Annexin A3 (ANXA3), transforming growth factor beta receptor 2 (TGFBR2), AHNAK

nucleoprotein 2 (AHNAK2), transforming growth factor beta 1 (TGFB1), ubiquitin C-terminal hydrolase L1 (UCHL1), CD55, CD44, CD109. Fascin actin-bundling protein-1 (FSCN1), a taxane-resistant gene, was also identified as the top DEG for PC-3 2D model subtypes (Table 3.5). DEGs including CD55, VIM, CD44, HAS3, EPCAM, ANXA3, LOXL2, CD109, TGFBR2, AHNAK2, and ANXA2 were upregulated compared to initial (0 days) 3D spheroids with three days 3D spheroids and seven days 3D spheroids. Further, MMPs and their activating factors such as MMP1, MMP13, MMP14, MMP15, MMP16, plasminogen activator, urokinase (PLAU), and other cancer hallmark genes Fos proto-oncogene, AP-1 transcription factor subunit (FOS), P21 (CDKNA1), and vascular endothelial growth factor A (VEGFA) were also expressed differentially in PC-3 2 days 3D spheroid vs. 7 days 3D spheroid (Figure 3.32).

3.11 2D vs. 3D RNA Sequencing Analysis

PC-3 2D vs. 3D mono-culture spheroid analysis identified that a majority of known EMT markers were upregulated in the 3D spheroid model compared to the 2D cell line culture. S100A6, HAS3, CD44, LOXL2, ANXA2P2, ANXA2, EPCAM were upregulated 1.46, 2.78, 1.99, 2.06, 1.35, and 1.24, respectively ($P<0.05$) (Table 3.6). Further, the Taxane-resistance gene FSCN1 was upregulated 2.51-fold in the 3D spheroid compared to the 2D PC-3 model (Table 3.6).

PI (µM)	Absorptions (OD)			Mean	SD	CV%	LOQ
0.97	0.005	0.004	0.002	0.00	0.001	39.250	-9.04
1.95	0.010	0.009	0.007	0.01	0.002	22.434	131.35
3.9	0.016	0.011	0.011	0.01	0.003	20.341	120.56
7.8	0.018	0.020	0.018	0.02	0.001	7.47	100.5
15.6	0.030	0.037	0.031	0.03	0.004	12.2	97.5
31.3	0.059	0.073	0.059	0.06	0.008	12.8	100
62.5	0.113	0.145	0.135	0.13	0.017	12.7	107
125	0.214	0.273	0.228	0.24	0.031	13.1	98.7
250	0.442	0.546	0.457	0.48	0.057	11.7	100
500	0.993	0.947	0.945	0.96	0.027	2.8	100

Table 3.1 Propidium iodide (PI) quantification assay using standard curve to identify LOQ (limit of quantification) of the PI with +/-10% accuracy and CV% (coefficient of variation) of <15%. SD, standard deviation.

PI Loading Concentration (mM)	1	0.5	0.25
Lipid Concentration (mM)	10	10	10
PI-Recovery %	12 ± 3	12 ± 3	Below Detection Limit
Lipid Concentration after Preparation (mM)	10 ± 1	10 ± 1	10 ± 1
Final PI: Lipid (mole basis)	0.12:10	0.06:10	_
Encapsulation Efficiency %	8.69 ± 2.42	10.18 ± 4.63	_

Table 3.2. Propidium iodide (PI) loading concentrations, Lipid concentration at the preparation, PI-recovery %, Lipid concentration after the preparation, final PI: Lipid (mole basis), and encapsulation efficiency %. Conventional and PEGylated liposomes showed similar results (mean ± SD).

Formulation	Size Distribution (nm)			Electrophoretic Mobility (μmcm/Vs)		Zeta Potential (mV)	
Time Point	**Zero**	**72 h**	**PdI**	**Zero**	**72 h**	**Zero**	**72 h**
Conventional	105-125	+22%	<0.1	1.5±0.15	-0.3±0.25	20±2	-4.5±2.6
PEGylated	110-130	+0.6%	<0.1	-2±0.15	-1.5±0.2	-29±2	-19.4±2

Table 3.3. Liposome formulations' volume weighted size distribution, electrophoretic mobility, and zeta potential stability after 72 h in biological conditions (serum-supplemented media at 37˚C), mean ± SD.

Gene symbol	Gene name	P-value (PC-3 - 3D vs. PC-3- 2D)	FDR step up (PC-3 - 3D vs. PC-3- 2D)	Ratio (PC-3 - 3D vs. PC-3- 2D)	Fold change (PC-3 - 3D vs. PC3- 2D)	LS Mean (PC-3 - 3D) (PC-3 - 3D vs. PC-3- 2D)	LS Mean (PC-3- 2D) (PC-3 - 3D vs. PC-3- 2D)
ENSG00000075618	**FSCN1**	4.04E-65	1.56E-62	2.51E+00	2.51	1.21E+03	4.81E+02
ENSG00000197956	**S100A6**	7.41E-46	2.04E-43	1.46E+00	1.46	3.46E+03	2.37E+03
ENSG00000103044	**HAS3**	7.67E-40	1.85E-37	2.78E+00	2.78	6.31E+02	2.27E+02
ENSG00000185567	**AHNAK2**	3.11E-22	3.60E-20	4.54E-01	-2.20	2.19E+02	4.83E+02
ENSG00000026508	**CD44**	6.98E-14	4.31E-12	1.99E+00	1.99	3.55E+02	1.78E+02
ENSG00000026025	**VIM**	3.63E-05	6.68E-04	8.08E-01	-1.24	6.79E+02	8.40E+02
ENSG00000134013	**LOXL2**	3.85E-05	7.04E-04	2.06E+00	2.06	9.96E+01	4.84E+01
ENSG00000231991	**ANXA2P2**	1.03E-04	1.67E-03	1.35E+00	1.35	4.02E+02	2.99E+02
ENSG00000182718	**ANXA2**	2.18E-04	3.21E-03	1.24E+00	1.24	6.62E+02	5.34E+02
ENSG00000138772	**ANXA3**	1.86E-03	2.00E-02	5.67E-01	-1.76	4.72E+01	8.32E+01
ENSG00000156535	**CD109**	2.82E-02	1.79E-01	7.61E-01	-1.31	1.14E+02	1.50E+02
ENSG00000119888	**EPCAM**	3.52E-02	2.10E-01	1.27E+00	1.27	1.78E+02	1.41E+02
ENSG00000163513	**TGFBR2**	6.08E-02	3.09E-01	7.53E-01	-1.33	7.69E+01	1.02E+02
ENSG00000105329	**TGFB1**	7.09E-02	3.44E-01	8.26E-01	-1.21	1.64E+02	1.98E+02
ENSG00000196352	**CD55**	7.03E-01	9.99E-01	9.64E-01	-1.04	2.15E+02	2.23E+02

Table 3.4. RNA sequencing analysis for PC-3 2D.

The results included top DEGs for the PC-3 2D model.

Gene symbol	P-value (CTRL -control spheroid day 3 vs. day 0)	Fold change (CTRL -control spheroid day 3 vs. day 0)	P-value (CTRL - control spheroid day 7 vs. day 0)	Fold change (CTRL - control spheroid day 7 vs. day 0)
CD55	1.72E-03	1.33	1.89E-01	1.13E+00
VIM	2.65E-03	1.16	7.16E-02	1.10E+00
CD44	2.05E-02	-1.19	5.56E-01	1.04E+00
HAS3	1.39E-01	1.08	7.80E-09	1.34E+00
EPCAM	1.64E-01	-1.16	7.36E-01	-1.04E+00
ANXA3	1.98E-01	1.28	5.75E-01	1.12E+00
LOXL2	3.97E-01	1.12	4.38E-02	1.30E+00
CD109	4.65E-01	-1.10	3.29E-01	1.13E+00
TGFBR2	4.69E-01	1.11	3.07E-01	1.16E+00
AHNAK2	8.44E-01	-1.02	4.68E-03	1.28E+00
ANXA2	8.65E-01	1.01	1.83E-01	-1.08E+00

Table 3.5. RNA sequencing analysis for PC-3 3D mono-cellular spheroid model.

The result included top DEGs for the 3D model

Gene name	P-value (PC-3 - 3D vs. PC-3-2D)	Fold change (PC-3 - 3D vs. PC-3-2D)
FSCN1	4.04E-65	2.51
S100A6	7.41E-46	1.46
HAS3	7.67E-40	2.78
CD44	6.98E-14	1.99
LOXL2	3.85E-05	2.06
ANXA2P2	1.03E-04	1.35
ANXA2	2.18E-04	1.24
EPCAM	3.52E-02	1.27

Table 3.6. RNA sequencing analysis for PC-3 2D vs. PC-3 3D spheroid

3.12 Figure legends

Figure 3.1 A wide range absorbance spectrum of PI dissolved in pure ethanol to identify the maximum absorbance. A 15.6 μM of PI was used.

Figure 3.2 Absorbance spectrum of PI dissolved in pure ethanol. Different PI concentrations were used (500, 250, 125, 62.5, 31.25, 15.6, 7.8, 3.9, 1.95, and 0.97 μM).

Figure 3.3 Standard curve of free PI dissolved in pure ethanol. This figure represent the values calculated in table 3.1. The R^2 is the proportion of the variance in a regression. y represents any of the PI concentrations (μM), and x represents the absorbance (OD) of that specific PI concentration. 0.0019 is the slope and 0.0037 is the intercept. n=3.

Figure 3.4 Liposome size distribution comparisons between intensity and volume weighted with narrow (<0.1) polydispersity index (PDI) measurements. A) Conventional liposomes without PI. B) Conventional-PI liposomes. C) PEGylated liposomes without PI. D) PEGylated-PI liposomes. The left-sided figures show the size distributions by the intensity, and the right-sided figures show the size distributions by volume.

Figure 3.5 Liposome zeta potential comparisons between the formulations with and without the PI. A) Conventional liposomes. B) PEGylated liposomes. The standard deviation shows the no significant difference between the formulations with or without the PI.

Figure 3.6 Zeta Potential and stability of Conventional and PEGylated liposomes after 72 h exposure in biological conditions, serum-supplemented media at 37˚C. A) Represents

the conventional PI liposomes before and after stability studies. B) Represents the PEGylated PI liposomes before and after stability studies.

Figure 3.7 Propidium iodide (PI) stability in liposomes exposed to biological conditions (serum-supplemented media at 37˚C) for 72 h. Samples considered 100% encapsulating PI at time 0 were collected after 5, 24, 48, and 72 h exposure. The PEGylated liposomes showed reduced PI encapsulation after 5 hours for 15%, but the PI concentration was stable until the end of the experiments. The conventional liposomes showed gradual leakage of PI, but it had not exceeded 15% at the end of the experiments.

Figure 3.8 Propidium iodide (PI) cytotoxicity effect over PC-3 cell line. *In-vitro* effect of PI on the growth of PC-3 cells following 48h of different PI concentrations (125, 62.5, 31.25, 15.6, 7.8, and 3.9 µM) using mitochondrial activity (3-(4, 5-Dimethylthiazol-2-yl)-2,5-diphenyltetrazolium bromide or MTT assay. Results showed that little to no toxicity was identified at 10 µM up to 15 µM.

Figure 3.9 Conventional and PEGylated liposomes cytotoxicity effect over PC-3 cell line. *In-vitro* effect of liposomes on the growth of PC-3 cells following 48h of different lipid concentrations (5, 2.5, 1.25, 0.625, and 0.3125 mM) using mitochondrial activity (3-(4, 5-Dimethylthiazol-2-yl)-2,5-diphenyltetrazolium bromide or MTT assay. Results showed that liposome formulations are not toxic.

Figure 3.10 Propidium iodide (PI) uptake in live cells. Cells were incubated with 10 µM of free PI for 24 h, and it was captured using a Texas Red laser (596/615 excitation/emission). 30 min before imaging, cells were stained with 3 µM of Calcein

AM to identify live cells. Calcein AM was captured using a FITC laser (490/525 excitation/emission). Red is for PI. Green is for Calcein AM. Scale bar: 100 µm.

Figure 3.11 Free PI uptake in 2D monolayer PC-3 cells. 10 µM of PI was dosed over PC-3 cells and measured the uptake following different time points (6, 12, 24, and 48h) using fluorescence imaging with a Cytation5 multimode reader. BF is a Bright Field. TR is a Texas Red, and it represents PI uptake (red). FITC shows Calcein AM dye (green), and it stains live cells. The uptake increases with prolonged exposure to the free PI and starts after 12h.

Figure 3.12 PI-Conventional liposomes uptake in 2D monolayer PC-3 cells. 10 µM of PI was dosed over PC-3 cells and its uptake was measured at 6, 12, 24, and 48 h by fluorescence imaging. BF is a Bright Field. TR is a Texas Red, and it shows PI uptake (red). FITC shows Calcein AM dye (green), and it stains live cells. No uptake of the conventional-PI liposomes was visualized.

Figure 3.13 PI-PEGylated liposomes uptake in 2D monolayer PC-3 cells. 10 µM of PI was dosed over PC-3 cells and its uptake was measured at 6, 12, 24, and 48 h using fluorescence imaging. BF is a Bright Field. TR is a Texas Red, and it shows PI uptake (red). FITC shows Calcein AM dye (green), and it stains live cells. The uptake can be visualized after 48 h exposure to the PEGylated-PI liposomes.

Figure 3.14 Free PI uptake in 3D mono-culture PC-3 cells. 10 µM of PI was dosed over PC-3 cells and its uptake was measured at 6, 12, 24, and 48 h using fluorescence imaging. BF is a Bright Field. TR is a Texas Red, and it shows PI uptake (red). FITC shows

Calcein AM dye (green), and it stains live cells. The uptake of the free PI can be visualized after 6 h, which increases with further time points.

Figure 3.15 PI-Conventional liposomes uptake in 3D mono-culture PC-3 cells. 10 μM of PI was dosed over PC-3 cells and measured the uptake following different time points (6, 12, 24, and 48h) using Cytation5 imaging. BF is a Bright Field. TR is a Texas Red, and it shows PI uptake (red). FITC shows Calcein AM dye (green), and it stains live cells. There is no visualized uptake of the conventional-PI liposomes.

Figure 3.16 PI-PEGylated liposomes uptake in 3D mono-culture PC-3 cells. 10 μM of PI was dosed over PC-3 cells and measured the uptake following different time points (6, 12, 24, and 48h) using Cytation5 imaging. BF is a Bright Field. TR is a Texas Red, and it shows PI uptake (red). FITC shows Calcein AM dye (green), and it stains live cells. The uptake of the PEGylated-PI liposomes can be visualized after 48h.

Figure 3.17 Growth change within 3D mono-culture PC-3 cells. 3D spheroids of PC-3 cells were grown, and cell counts were identified at different time points (2, 4, 7, and 9 days) using confocal imaging. PC-3 cells were eGFP. The 3D mono-culture spheroids show a continuous growth.

Figure 3.18 Surface growth change within 3D co-culture (1:1) PC-3 and CAFs cells. 3D co-culture spheroids were grown, and cell counts were identified at different time points (2, 4, 7, and 9 days) using confocal imaging. PC-3 cells were GFP transfected. CAFs cells had no fluorescent, so all cells were stained with Hoechst 33342 dye to be able to

capture CAFs. Later at analysis, the eGFP cells (PC-3) number was deducted from the total cells number to get CAFs' number.

Figure 3.19 Center growth change within 3D co-culture (1:1) PC-3 and CAFs cells. 3D co-culture spheroids were grown, and cell counts were identified at different time points (2, 4, 7, and 9 days) using confocal imaging. PC-3 cells were GFP transfected. CAFs cells had no fluorescence, so all cells were stained with Hoechst 33342 dye to be able to capture CAFs. Later at analysis, the eGFP expressing PC-3 cell number was deducted from the total cells number to get CAFs' number. There was no significant growth difference between CAFs and PC-3 cells.

Figure 3.20 Growth comparison between mono-culture (PC-3) spheroids and co-culture [(1:1) PC-3 and CAFs] spheroids. A) The figure compares mono-culture and co-culture after 2 and 7 days. B) The images compare mono-culture and co-culture, captured after 2 days of growth. C) The images compare mono-culture and co-culture; they were captured after 7 days of growth. The size of the spheroids was identified by confocal imaging. A significant (P<0.05) growth difference between mono-culture and co-culture spheroids. Scale bar: 300 μm.

Figure 3.21 Surface uptake of free PI, Conventional-PI, and PEGylated-PI in 3D mono-culture and co-culture spheroids. After 2 and 7 days of the spheroids' growth, the formulations were dosed, and the formulations were incubated with spheroids for 48 h. The results were acquired using confocal imaging and analyzed by Fiji ImageJ version 2.3.0 software. A) Spheroids grown for 2 days. B) Spheroids grown for 7 days. PC-3 cells stably expressed eGFP. 3D co-culture spheroids nuclei stained with Hoechst 33342 dye,

including the CAFs. A significant difference (*P<0.05)* between the 3D mono-culture and co-culture in the free PI and the conventional-PI liposomes after 2 and 7 days of spheroid growth was observed. There was greater uptake of the PEGylated liposomes in the 3D mono-culture spheroids after 2 and 7 days of the spheroids' growth, but was only significant after 2 days of the spheroids growth.

Figure 3.22 Center uptake of free PI, Conventional-PI, and PEGylated-PI in 3D mono-culture and co-culture spheroids. After 2 and 7 days of the spheroids' growth, the formulations were dosed, and the formulations were incubated with spheroids for 48h. The results were acquired using confocal imaging and analyzed by Fiji ImageJ version 2.3.0 software. A) The spheroids were grown for 2 days. B) The spheroids were grown for 7 days. PC-3 cells stably expressed eGFP. 3D co-culture spheroids were stained with Hoechst 33342 dye to stain all cells' nuclei, including the CAFs. A significant (*P<0.05)* difference between the 3D mono-culture and co-culture spheroids in the PEGylated-PI liposomes after 2 days of the spheroids' growth.

Figure 3.23 Serial concentrations uptake free PI over different time points in a 2D monolayer of PC-3 cells. The cells were stained with different concentrations (20, 10, 5, 2.5, 1.25, and 0.62 μM) of free PI, and the uptake was identified after 24 and 48h of exposure. PC-3 cells were not GFP transfected. Calcein AM was used to capture live cell populations. The uptake of the free PI is time and concentration-dependent.

Figure 3.24 Antibody markers expression in PC-3 and CAFs cells. All marker expressions are identified by comparing unstained with stained populations. α-SMA is an intracellular marker; CD44, CD133, and EpCAM are cellular surface markers. EpCAM

antibody showed as a specific marker for PC-3 cells. 97.5% of the PC-3 cells stained with EpCAM, whereas the CAFs cells showed only 6.3% of EpCAM stain.

Figure 3.25 The effect of FBS blocking buffer vs Fc blocking buffer. Both buffers were diluted in 0.5% BSA buffer. Both buffers are incubated with the cells for 20 min at room temperature. The FBS buffer concentration was 10% (v/v) of FBS in 0.5% (w/v) bovine serum albumin (BSA). The Fc blocker buffer concentration was 2.5% (v/v) of Fc blocker in 0.5% (w/v) bovine serum albumin (BSA). A and B represent the 10% FBS blocking buffer. C and D represent the Fc blocking buffer. PC-3 cells are in A and C. CAFs are in B and D. The Fc blocking buffer shows better blocking of non-specific binding than the FBS blocking buffer. The antibody used in this experiment was the EpCAM marker.

Figure 3.26 Gating strategy depicting how samples were analyzed using FlowJo software. The samples were stained with Ghost Dye to exclude dead cells. EpCAM was used to stain PC-3 cells. PI was used to identify the uptake of the free PI or the PI-liposomes.

Figure 3.27 Free PI and PI-liposomes uptake in PC-3 cells in 2D monolayer culture, 3D mono-culture, and 3D co-culture after 2 days of growth. The cells were incubated with free PI, conventional PI liposomes, and PEGylated PI liposomes for 48h. The uptake was identified using flow cytometry. The PC-3 cells used were wild, not expressing eGFP. In 2D monolayer culture and 3D mono-culture, Calcein AM was used to capture live cell populations. In 3D co-culture, PC-3 cells were captured using EpCAM antibody, and the dead cells were excluded using Ghost Dye. The figure shows significantly (P<0.05)

lower uptake of the free PI and the PEGylated liposomes in the 3D co-culture compared to the 2D monolayer and 3D mono-culture. *Baseline is corrected to unstained controls.

Figure 3.28 Free PI and PI-liposomes uptake in PC-3 cells in 3D mono-culture and 3D co-culture after 7 days of growth. The cells were incubated with free PI, conventional PI liposomes, and PEGylated PI liposomes for 48 h. The uptake was identified using flow cytometry. The PC-3 cells used were not GFP transfected. In the 3D mono-culture, Calcein AM was used to capture live cell populations. In the 3D co-culture, PC-3 cells were captured using EpCAM antibody, and the dead cells were excluded using Ghost Dye. The figure shows significantly (P<0.05) reduced uptake of free PI and the PEGylated liposomes in the 3D co-culture compared to the 3D mono-culture. *Baseline is corrected to unstained controls.

Figure 3.29 Free PI and PI-liposomes uptake in co-culture (1:1) PC-3 and CAFs spheroids. The uptake was determined using flow cytometry. The samples were stained with EpCAM antibody that binds PC-3 cells' surfaces. A) The spheroids were grown for two days before adding the formulations. The PEGylated PI liposomes showed significantly (P<0.05) lower uptake in the EpCAM +ve PC-3 cells. B) The spheroids were grown seven days before the formulations were added. The PEGylated liposomes showed higher uptake in the EpCAM +ve PC-3 cells. *Baseline is corrected to unstained controls.

Figure 3.30 Growth change within 3D co-culture (1:1) PC-3 and CAFs cells. Spheroids' growth change compared between EpCAM +ve and EpCAM –ve populations at different time points (0, 2, 4, 7, and 9 days) using flow cytometry. A) Shows a significant (P<0.05)

reduction of the EpCAM +ve population, representing PC-3 cells after 4 days, and the further time points, the greater the significant (P<0.05) difference. B) The EpCAM gating of data using FlowJo software. *Baseline is corrected to unstained controls.

Figure 3.31 HeatMap represented Differentially Expressed Gene Signature (DEGs) for PC-3 3D mono-culture spheroid (P<0.05) for 0 days, 3 days, and 7 days. EMT markers were identified as top markers for 3D spheroids.

Figure 3.32 HeatMap represented Differentially Expressed Gene Signature (DEGs) for MMPs and cancer hallmark genes for PC-3 3D mono-culture spheroid (P<0.05) for 0 days, 3 days, and 7 days.

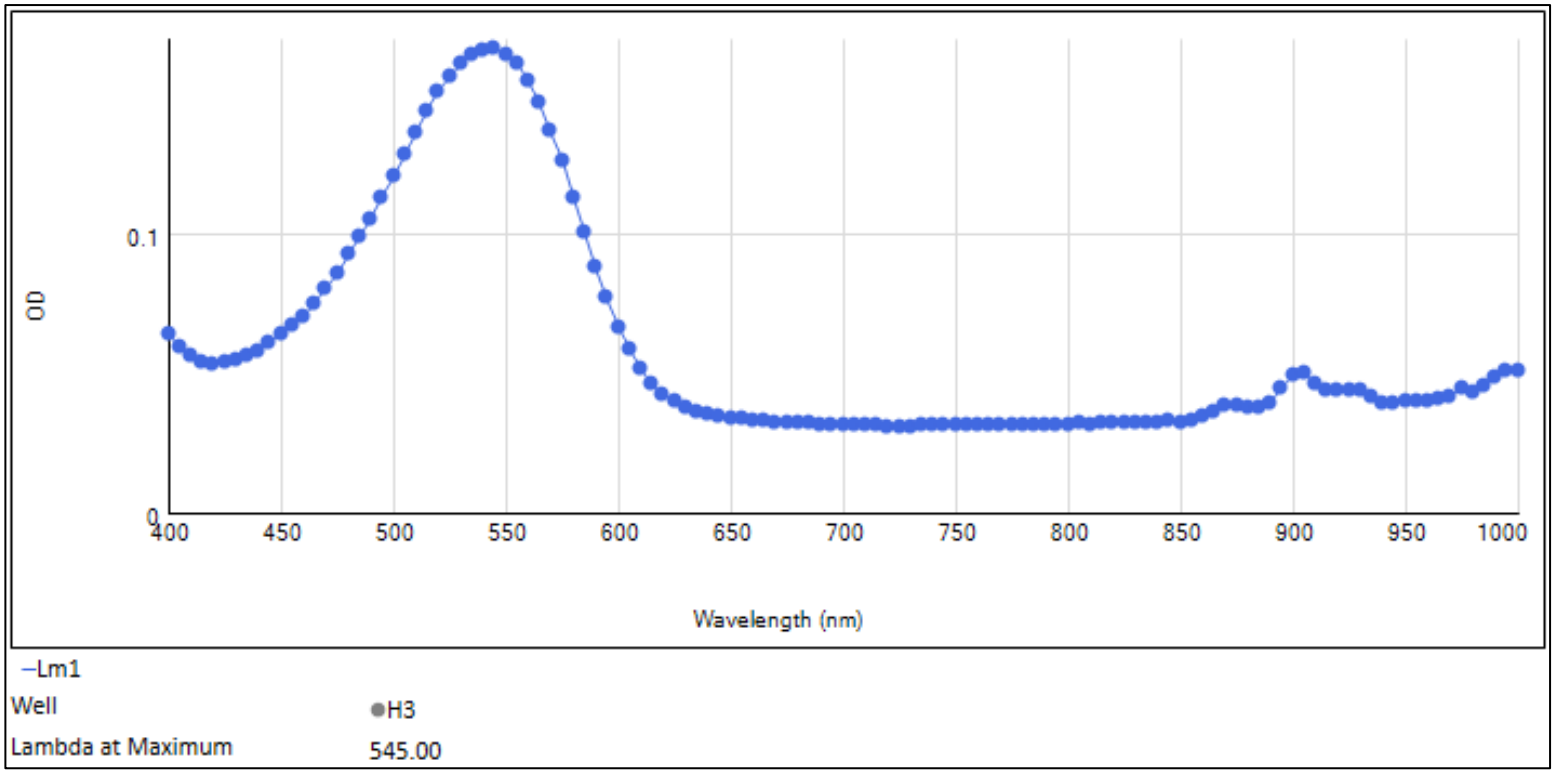
OD
0.1
0
400
450
500
550
600
650
700
750
800
850
900
950
1000
Wavelength (nm)
Lm1
Well
H3
Lambda at Maximum
545.00

Figure 3.1

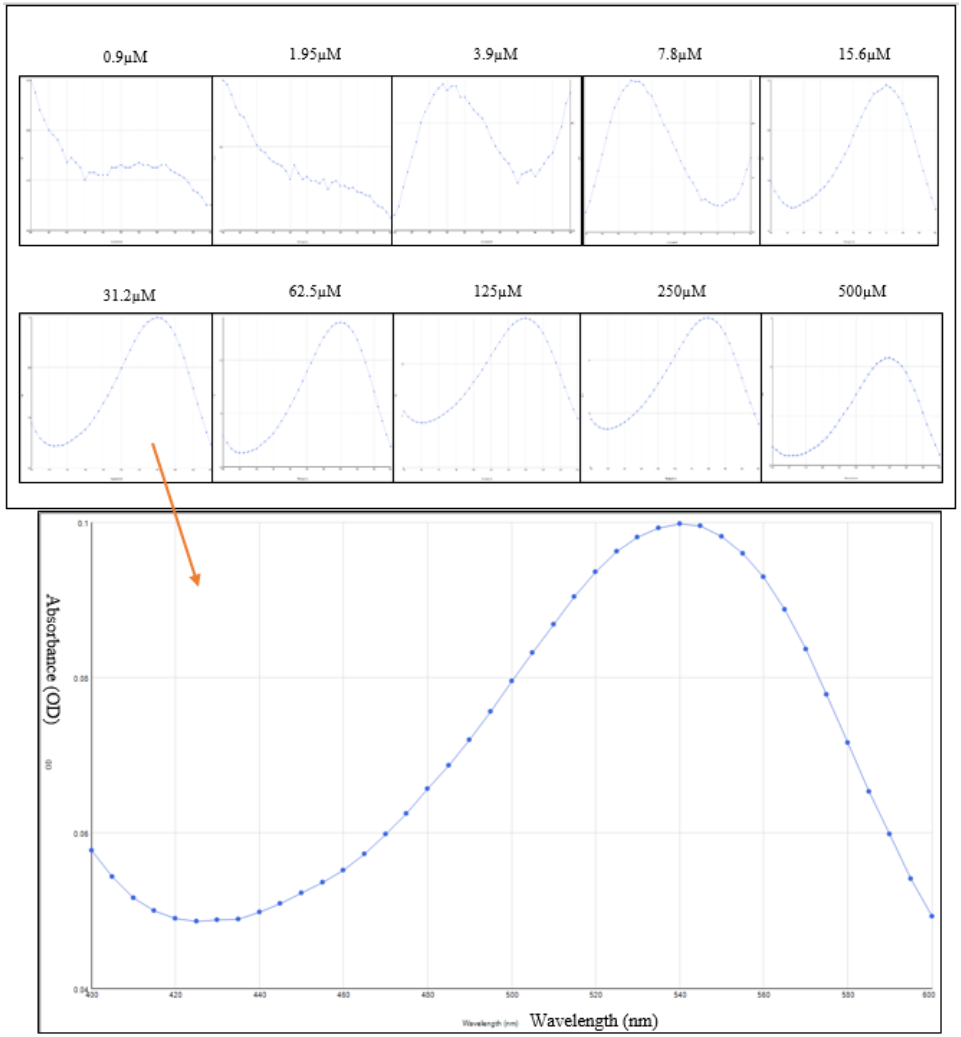
0.9µM
1.95µM
3.9µM
7.8µM
15.6µM
31.2µM
62.5µM
125µM
250µM
500µM
Absorbance (OD)
Wavelength (nm)

Figure 3.2

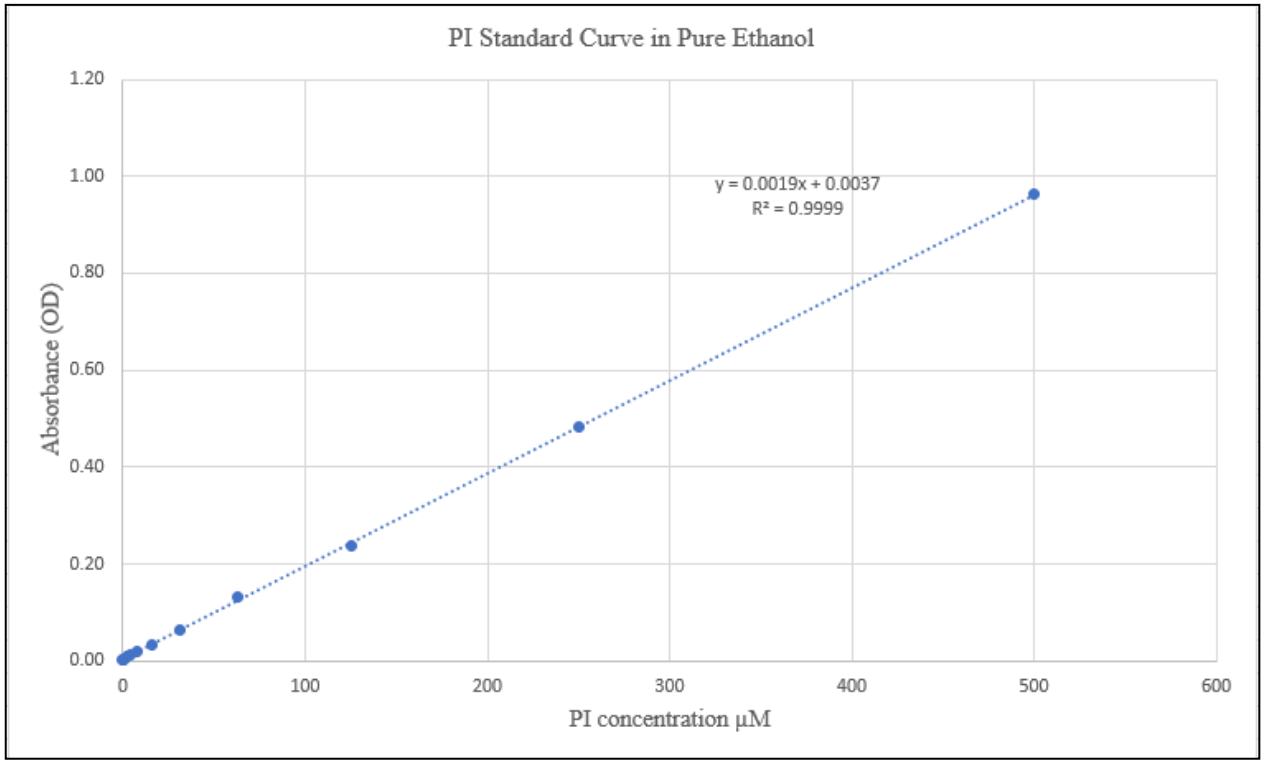
PI Standard Curve in Pure Ethanol
y = 0.0019x + 0.0037
R² = 0.9999
Absorbance (OD)
PI concentration µM
1.20
1.00
0.80
0.60
0.40
0.20
0.00
0
100
200
300
400
500
600

Figure 3.3


A
Z-Average (d.nm): 114.7
PdI: 0.096
Intercept: 0.929
Result quality : Good
Size (d.nm): % Intensity: St Dev (d.nm):
Peak 1: 126.5 100.0 40.23
Peak 2: 0.000 0.0 0.000
Peak 3: 0.000 0.0 0.000
Size Distribution by Intensity
Intensity (Percent)
Size (d.nm)
Record 5: Conventional No Pl
Z-Average (d.nm): 114.7
PdI: 0.096
Intercept: 0.929
Result quality : Good
Size (d.nm): % Volume: St Dev (d.nm):
Peak 1: 108.7 100.0 40.28
Peak 2: 0.000 0.0 0.000
Peak 3: 0.000 0.0 0.000
Size Distribution by Volume
Volume (Percent)
Size (d.nm)
Record 5: Conventional No Pl
B
Z-Average (d.nm): 116.5
PdI: 0.055
Intercept: 0.930
Result quality : Good
Size (d.nm): % Intensity: St Dev (d.nm):
Peak 1: 124.4 100.0 33.07
Peak 2: 0.000 0.0 0.000
Peak 3: 0.000 0.0 0.000
Size Distribution by Intensity
Intensity (Percent)
Size (d.nm)
Record 4: Conventional-Pl
Z-Average (d.nm): 116.5
PdI: 0.055
Intercept: 0.930
Result quality : Good
Size (d.nm): % Volume: St Dev (d.nm):
Peak 1: 111.6 100.0 34.27
Peak 2: 0.000 0.0 0.000
Peak 3: 0.000 0.0 0.000
Size Distribution by Volume
Volume (Percent)
Size (d.nm)
Record 4: Conventional-Pl
C
Z-Average (d.nm): 126.3
PdI: 0.088
Intercept: 0.920
Result quality : Good
Size (d.nm): % Intensity: St Dev (d.nm):
Peak 1: 137.7 100.0 40.81
Peak 2: 0.000 0.0 0.000
Peak 3: 0.000 0.0 0.000
Size Distribution by Intensity
Intensity (Percent)
Size (d.nm)
Record 4: PEGylated No Pl
Z-Average (d.nm): 126.3
PdI: 0.088
Intercept: 0.920
Result quality : Good
Size (d.nm): % Volume: St Dev (d.nm):
Peak 1: 123.7 100.0 43.24
Peak 2: 0.000 0.0 0.000
Peak 3: 0.000 0.0 0.000
Size Distribution by Volume
Volume (Percent)
Size (d.nm)
Record 4: PEGylated No Pl
D
Z-Average (d.nm): 126.3
PdI: 0.099
Intercept: 0.925
Result quality : Good
Size (d.nm): % Intensity: St Dev (d.nm):
Peak 1: 139.5 100.0 44.06
Peak 2: 0.000 0.0 0.000
Peak 3: 0.000 0.0 0.000
Size Distribution by Intensity
Intensity (Percent)
Size (d.nm)
Record 5: PEGylated-Pl
Z-Average (d.nm): 126.3
PdI: 0.099
Intercept: 0.925
Result quality : Good
Size (d.nm): % Volume: St Dev (d.nm):
Peak 1: 124.2 100.0 46.36
Peak 2: 0.000 0.0 0.000
Peak 3: 0.000 0.0 0.000
Size Distribution by Volume
Volume (Percent)
Size (d.nm)
Record 5: PEGylated-Pl

Figure 3.4

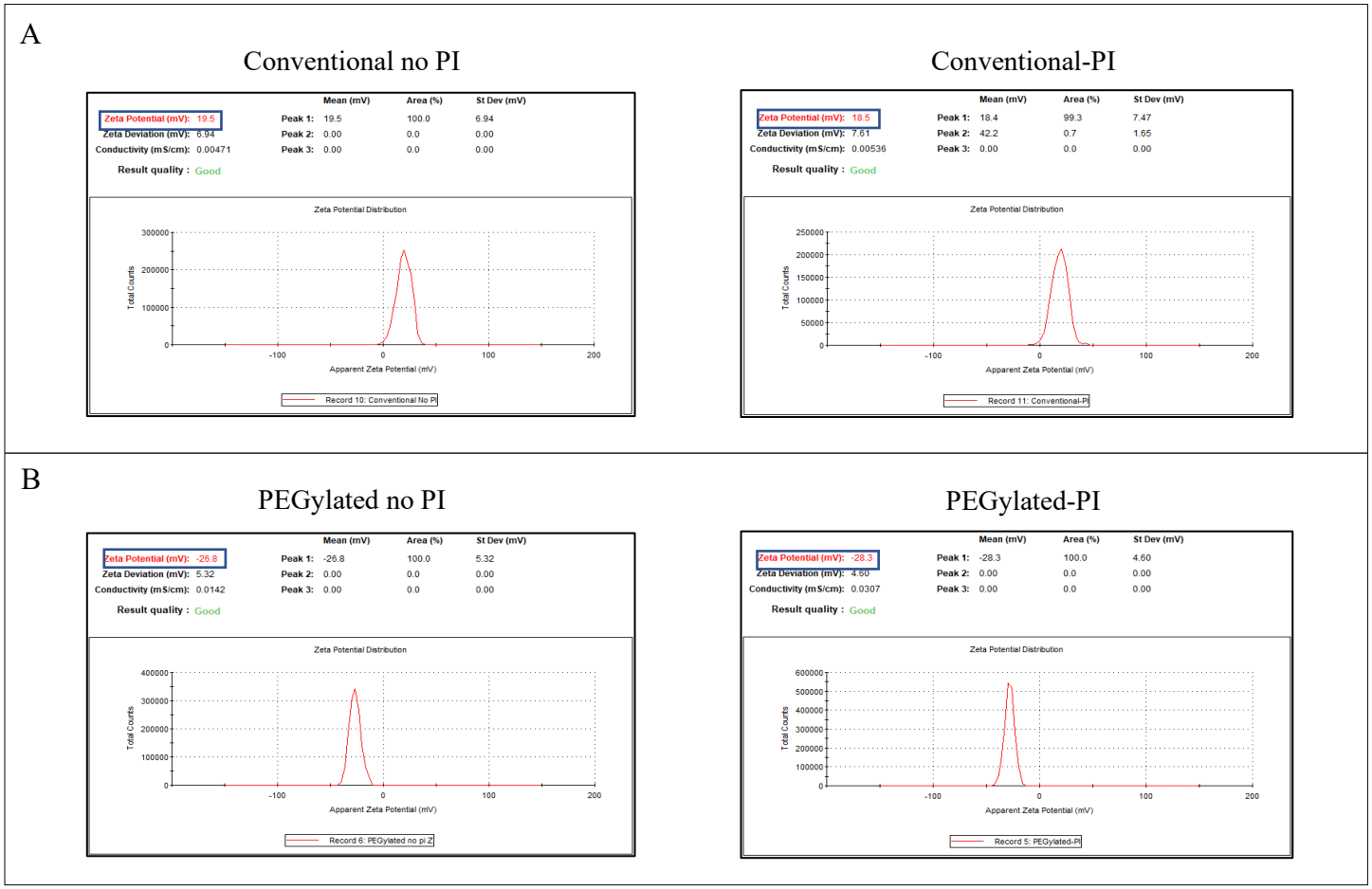
A
Conventional no PI
Zeta Potential (mV): 19.5
Zeta Deviation (mV): 6.94
Conductivity (mS/cm): 0.00471
Result quality : Good
Mean (mV) Area (%) St Dev (mV)
Peak 1: 19.5 100.0 6.94
Peak 2: 0.00 0.0 0.00
Peak 3: 0.00 0.0 0.00
Zeta Potential Distribution
Total Counts
Apparent Zeta Potential (mV)
Record 10: Conventional No PI
Conventional-PI
Zeta Potential (mV): 18.5
Zeta Deviation (mV): 7.61
Conductivity (mS/cm): 0.00536
Result quality : Good
Mean (mV) Area (%) St Dev (mV)
Peak 1: 18.4 99.3 7.47
Peak 2: 42.2 0.7 1.65
Peak 3: 0.00 0.0 0.00
Zeta Potential Distribution
Total Counts
Apparent Zeta Potential (mV)
Record 11: Conventional-PI
B
PEGylated no PI
Zeta Potential (mV): -26.8
Zeta Deviation (mV): 5.32
Conductivity (mS/cm): 0.0142
Result quality : Good
Mean (mV) Area (%) St Dev (mV)
Peak 1: -26.8 100.0 5.32
Peak 2: 0.00 0.0 0.00
Peak 3: 0.00 0.0 0.00
Zeta Potential Distribution
Total Counts
Apparent Zeta Potential (mV)
Record 6: PEGylated no pI Z
PEGylated-PI
Zeta Potential (mV): -28.3
Zeta Deviation (mV): 4.60
Conductivity (mS/cm): 0.0307
Result quality : Good
Mean (mV) Area (%) St Dev (mV)
Peak 1: -28.3 100.0 4.60
Peak 2: 0.00 0.0 0.00
Peak 3: 0.00 0.0 0.00
Zeta Potential Distribution
Total Counts
Apparent Zeta Potential (mV)
Record 5: PEGylated-PI

Figure 3.5

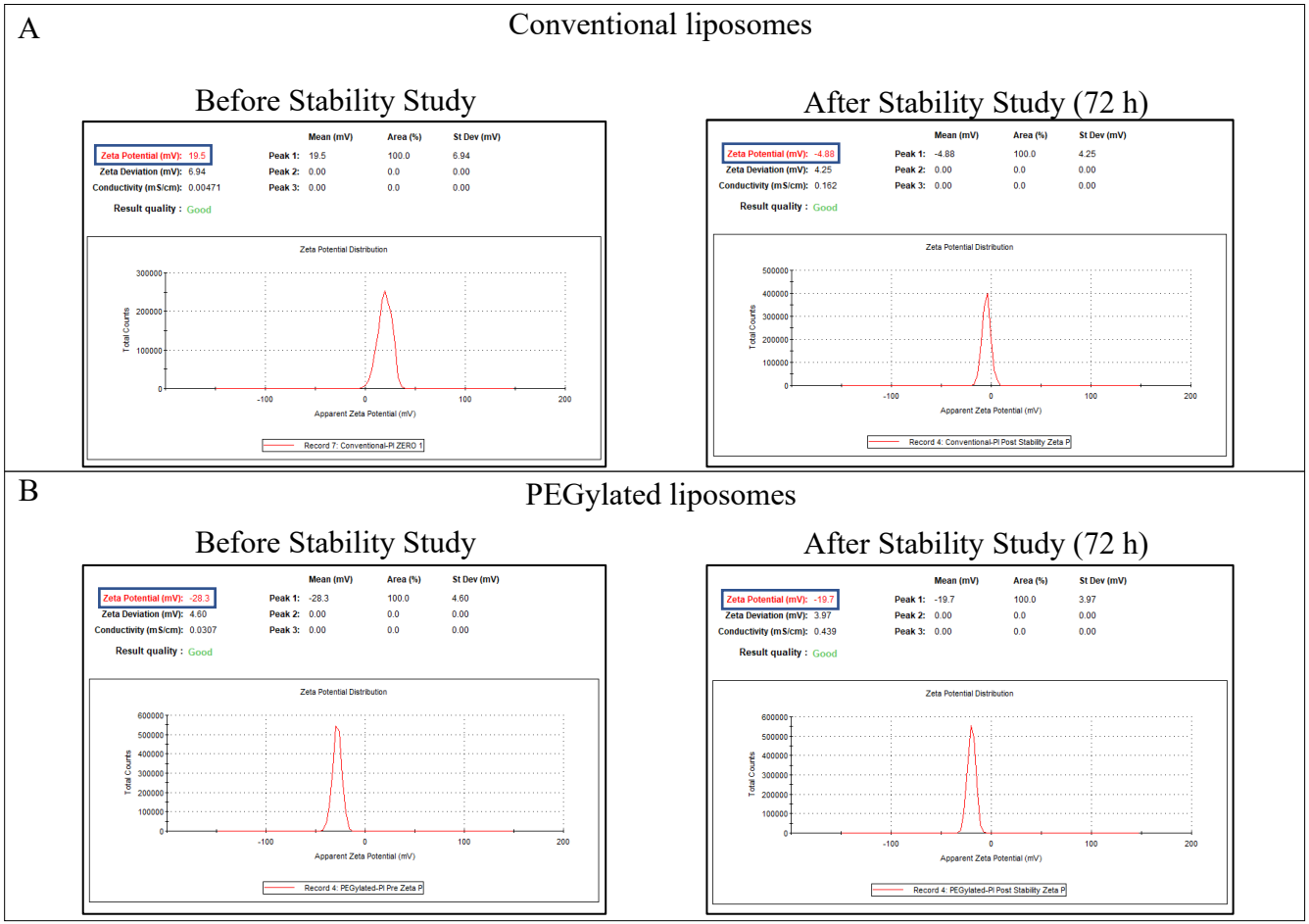
A
Conventional liposomes
Before Stability Study
Zeta Potential (mV): 19.5
Zeta Deviation (mV): 6.94
Conductivity (mS/cm): 0.00471
Result quality : Good
Mean (mV) Area (%) St Dev (mV)
Peak 1: 19.5 100.0 6.94
Peak 2: 0.00 0.0 0.00
Peak 3: 0.00 0.0 0.00
Zeta Potential Distribution
Total Counts
Apparent Zeta Potential (mV)
Record 7: Conventional-PI ZERO 1
After Stability Study (72 h)
Zeta Potential (mV): -4.88
Zeta Deviation (mV): 4.25
Conductivity (mS/cm): 0.162
Result quality : Good
Mean (mV) Area (%) St Dev (mV)
Peak 1: -4.88 100.0 4.25
Peak 2: 0.00 0.0 0.00
Peak 3: 0.00 0.0 0.00
Zeta Potential Distribution
Total Counts
Apparent Zeta Potential (mV)
Record 4: Conventional-PI Post Stability Zeta P
B
PEGylated liposomes
Before Stability Study
Zeta Potential (mV): -28.3
Zeta Deviation (mV): 4.60
Conductivity (mS/cm): 0.0307
Result quality : Good
Mean (mV) Area (%) St Dev (mV)
Peak 1: -28.3 100.0 4.60
Peak 2: 0.00 0.0 0.00
Peak 3: 0.00 0.0 0.00
Zeta Potential Distribution
Total Counts
Apparent Zeta Potential (mV)
Record 4: PEGylated-PI Pre Zeta P
After Stability Study (72 h)
Zeta Potential (mV): -19.7
Zeta Deviation (mV): 3.97
Conductivity (mS/cm): 0.439
Result quality : Good
Mean (mV) Area (%) St Dev (mV)
Peak 1: -19.7 100.0 3.97
Peak 2: 0.00 0.0 0.00
Peak 3: 0.00 0.0 0.00
Zeta Potential Distribution
Total Counts
Apparent Zeta Potential (mV)
Record 4: PEGylated-PI Post Stability Zeta P

Figure 3.6

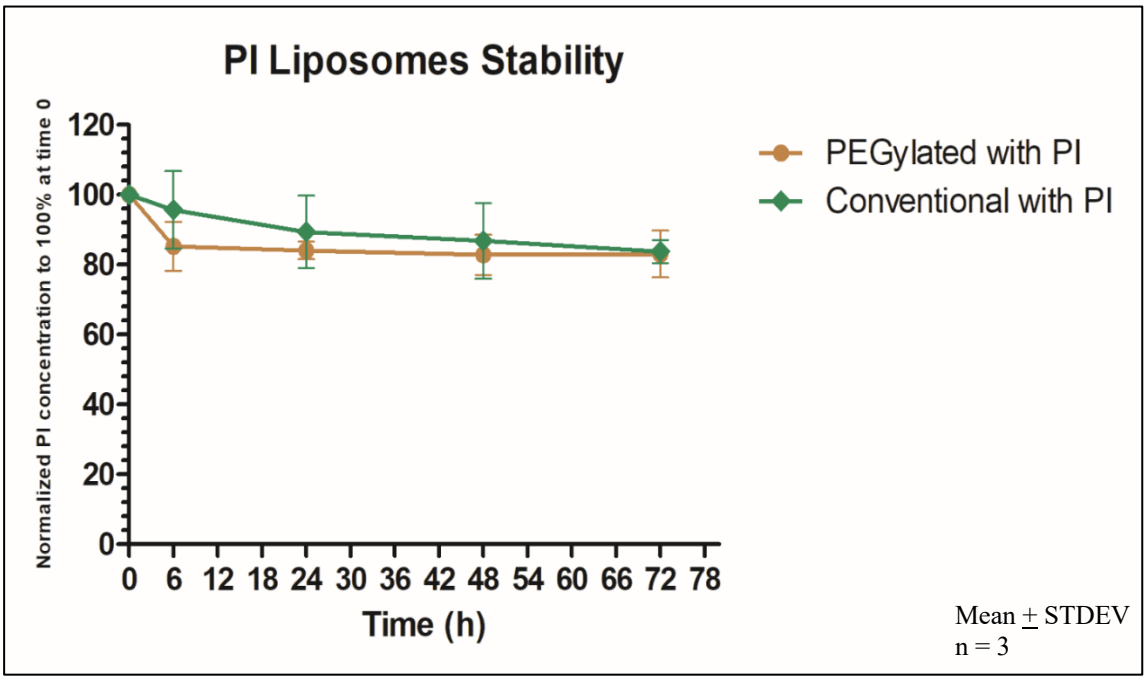
PI Liposomes Stability
Normalized PI concentration to 100% at time 0
120
100
80
60
40
20
0
0 6 12 18 24 30 36 42 48 54 60 66 72 78
Time (h)
PEGylated with PI
Conventional with PI
Mean ± STDEV
n = 3

Figure 3.7

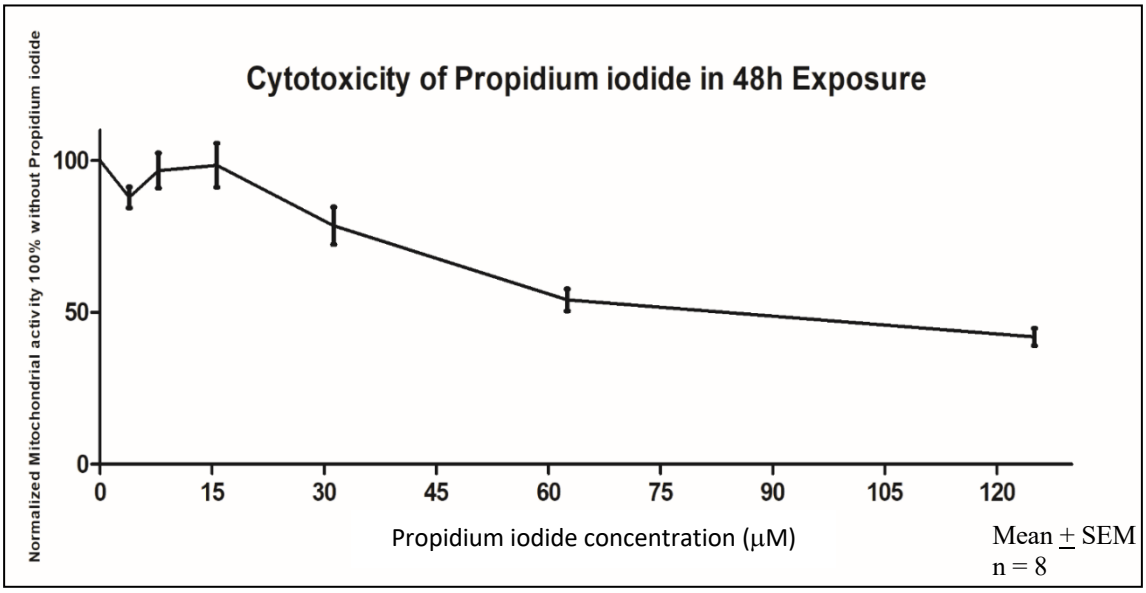
Cytotoxicity of Propidium iodide in 48h Exposure
Normalized Mitochondrial activity 100% without Propidium iodide
100
50
0
0
15
30
45
60
75
90
105
120
Propidium iodide concentration (μM)
Mean ± SEM
n = 8

Figure 3.8

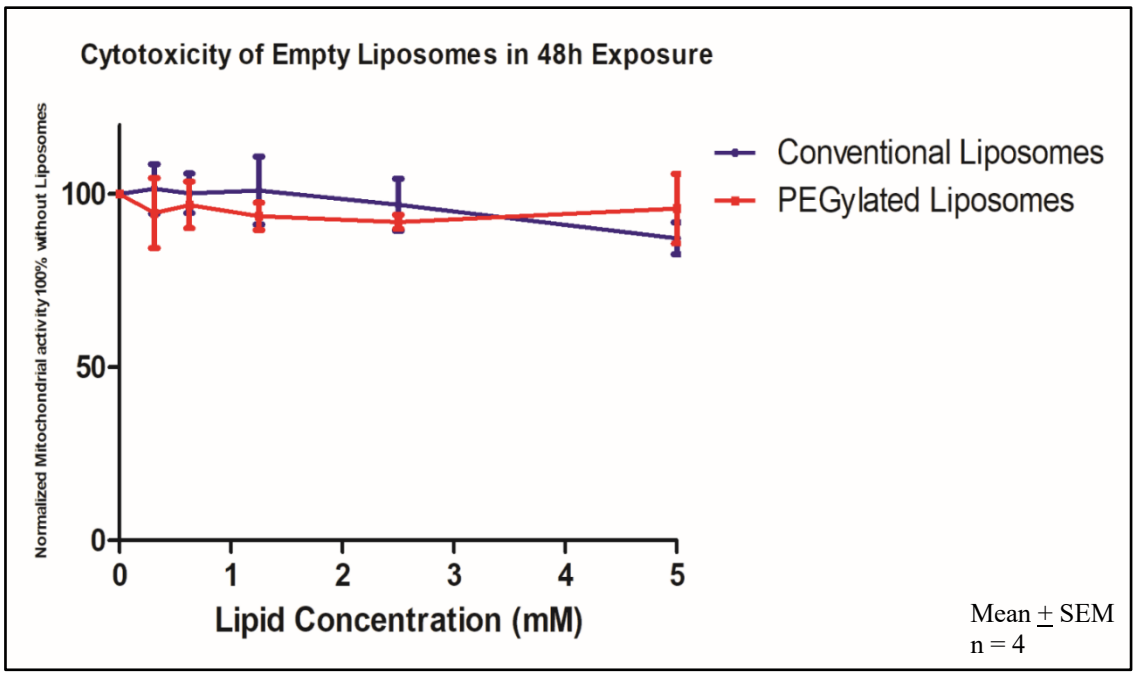
Cytotoxicity of Empty Liposomes in 48h Exposure
Normalized Mitochondrial activity 100% without Liposomes
100
50
0
0
1
2
3
4
5
Lipid Concentration (mM)
Conventional Liposomes
PEGylated Liposomes
Mean ± SEM
n = 4

Figure 3.9

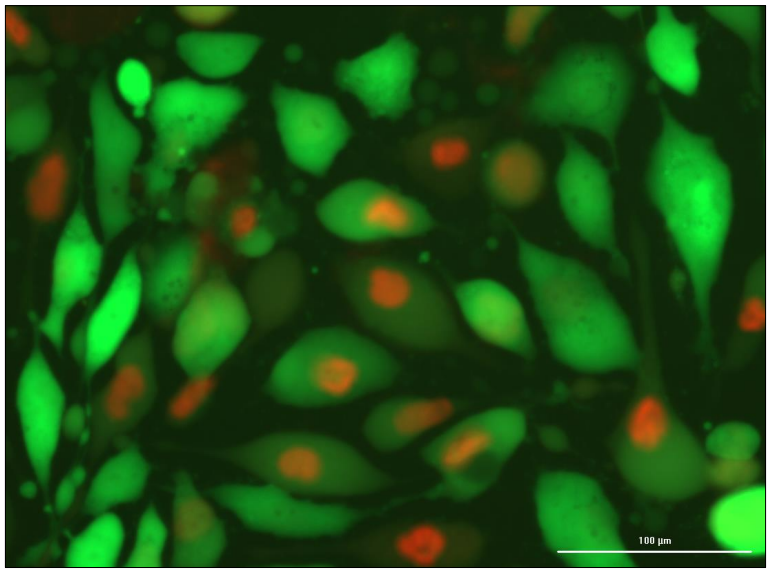

Figure 3.10

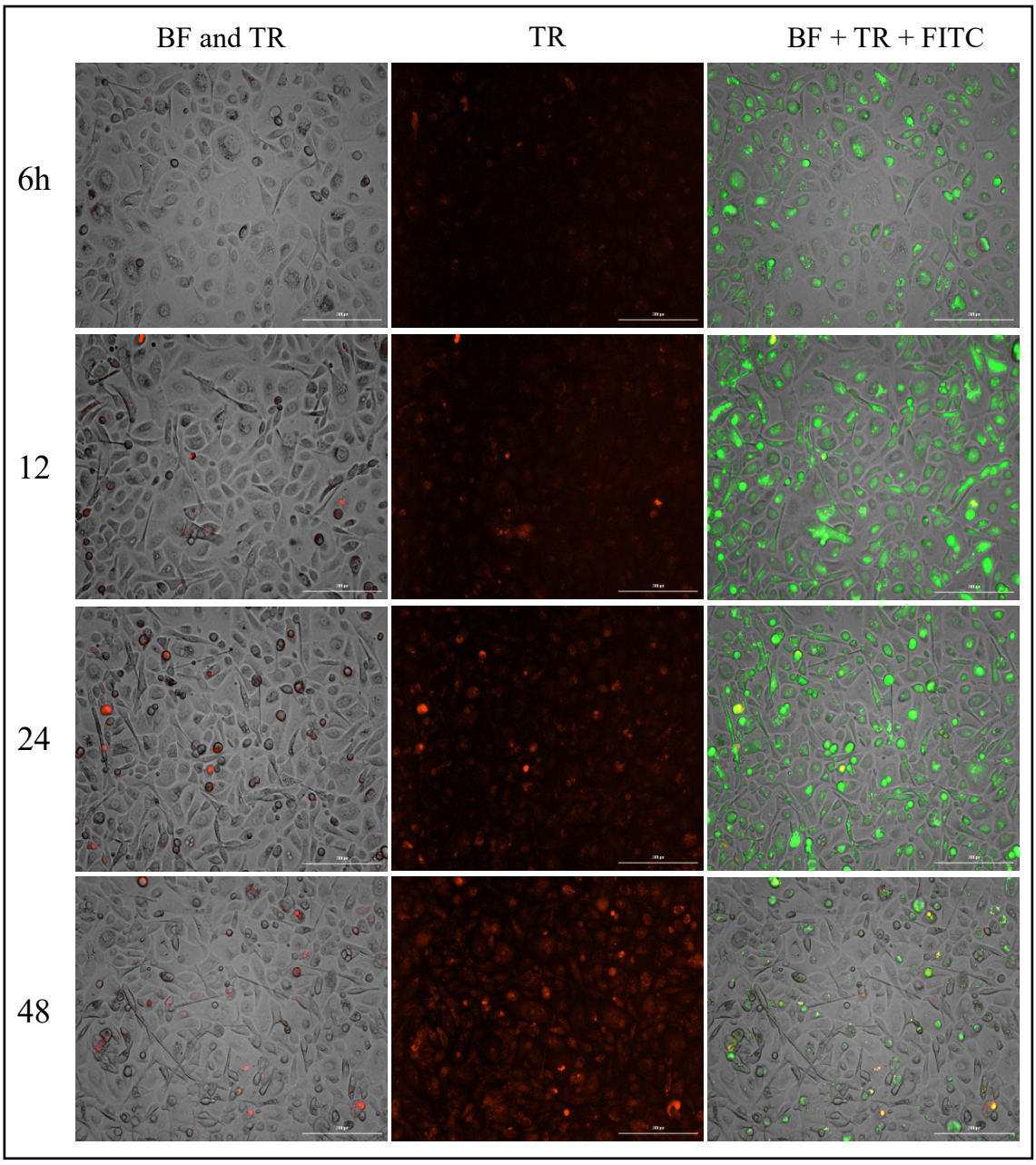

Figure 3.11

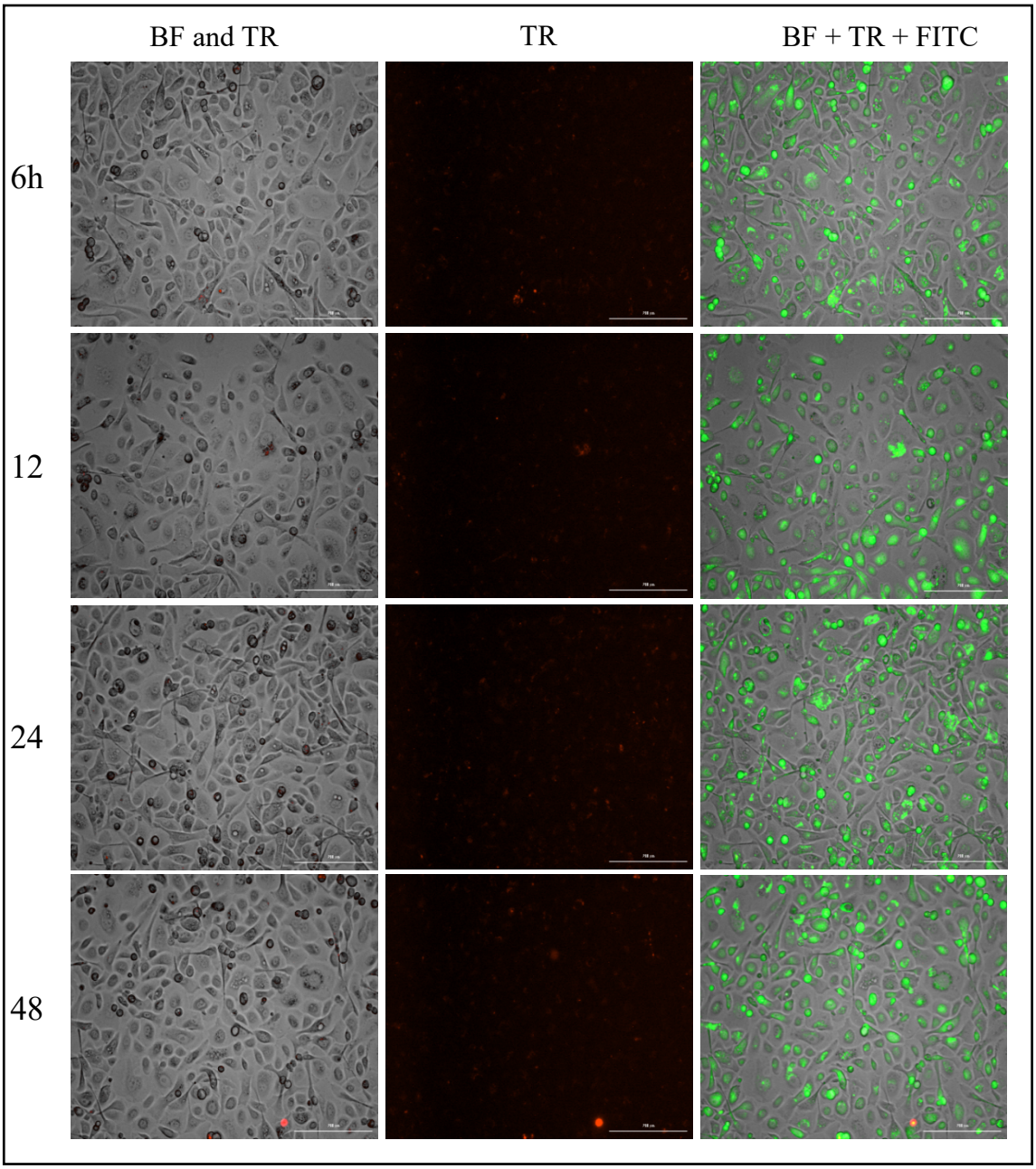

Figure 3.12

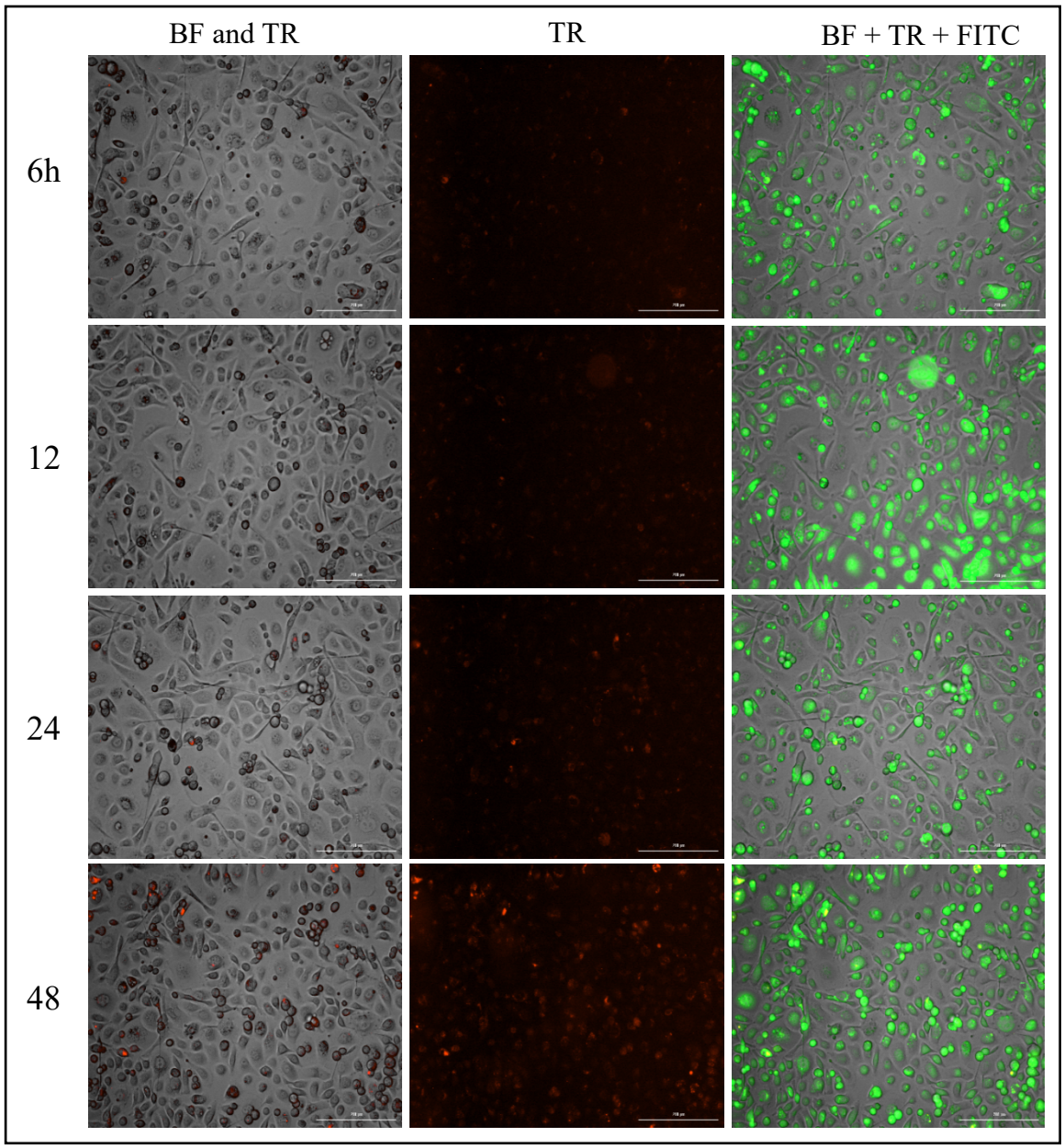

Figure 3.13

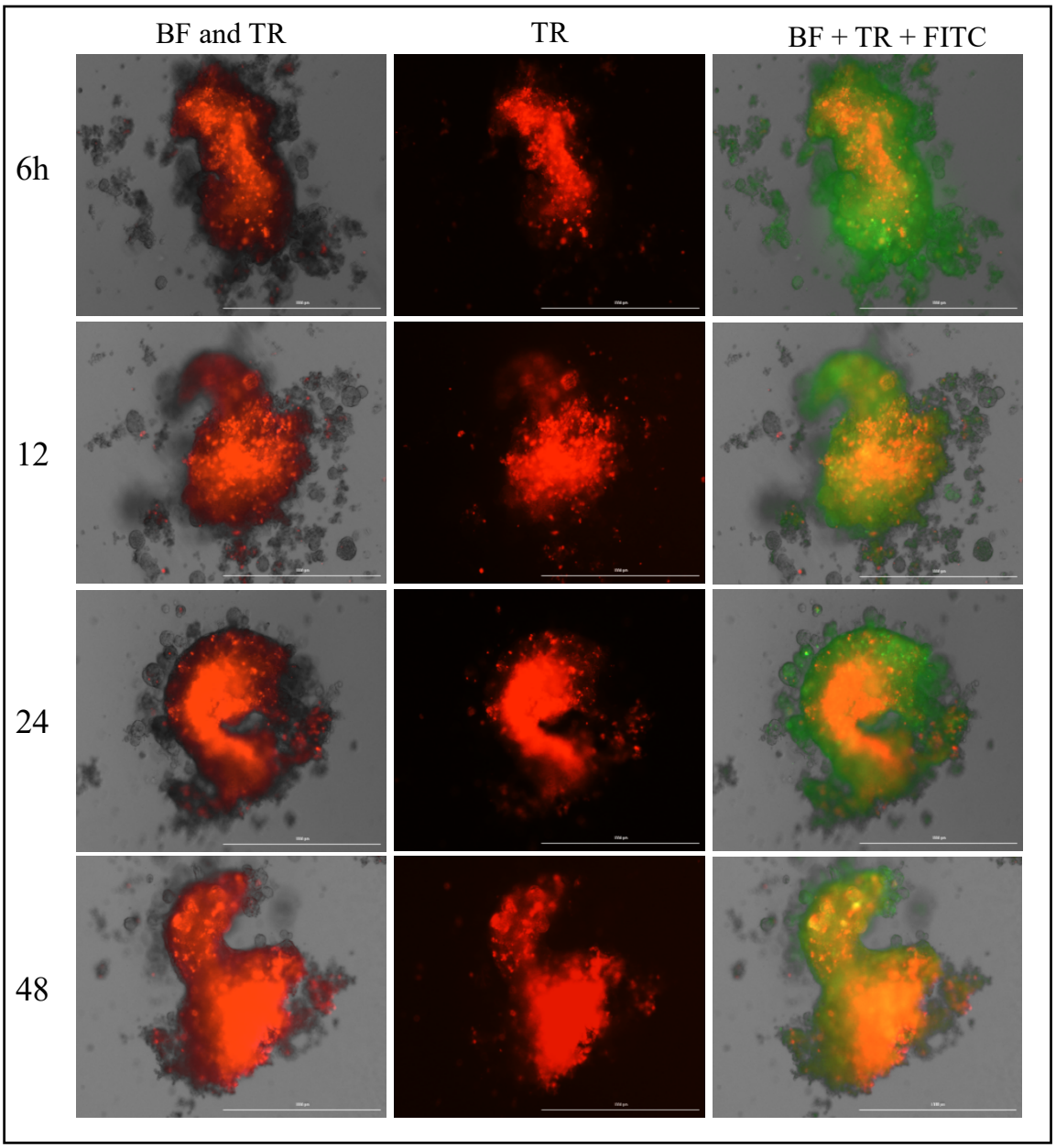

Figure 3.14

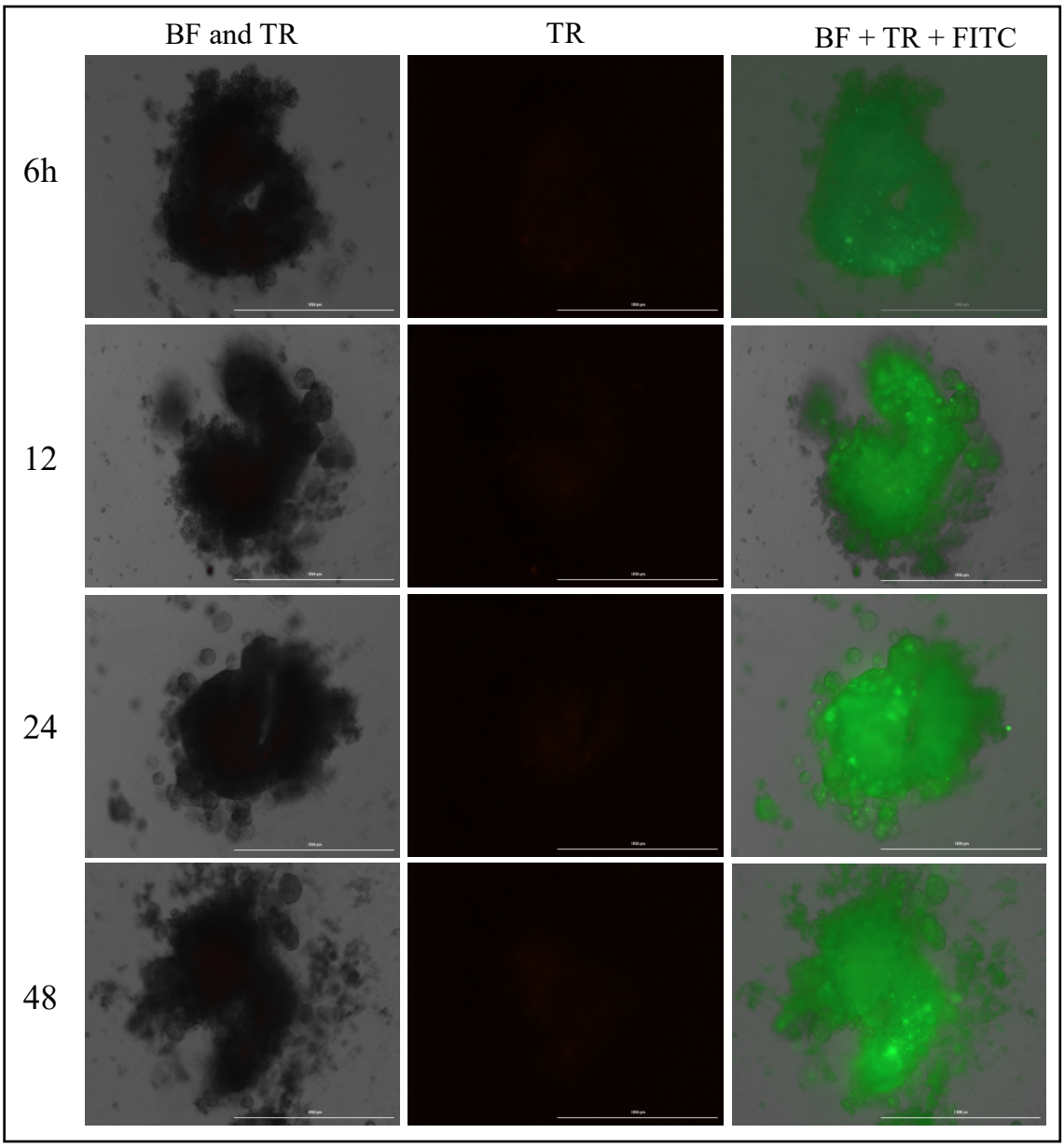

Figure 3.15

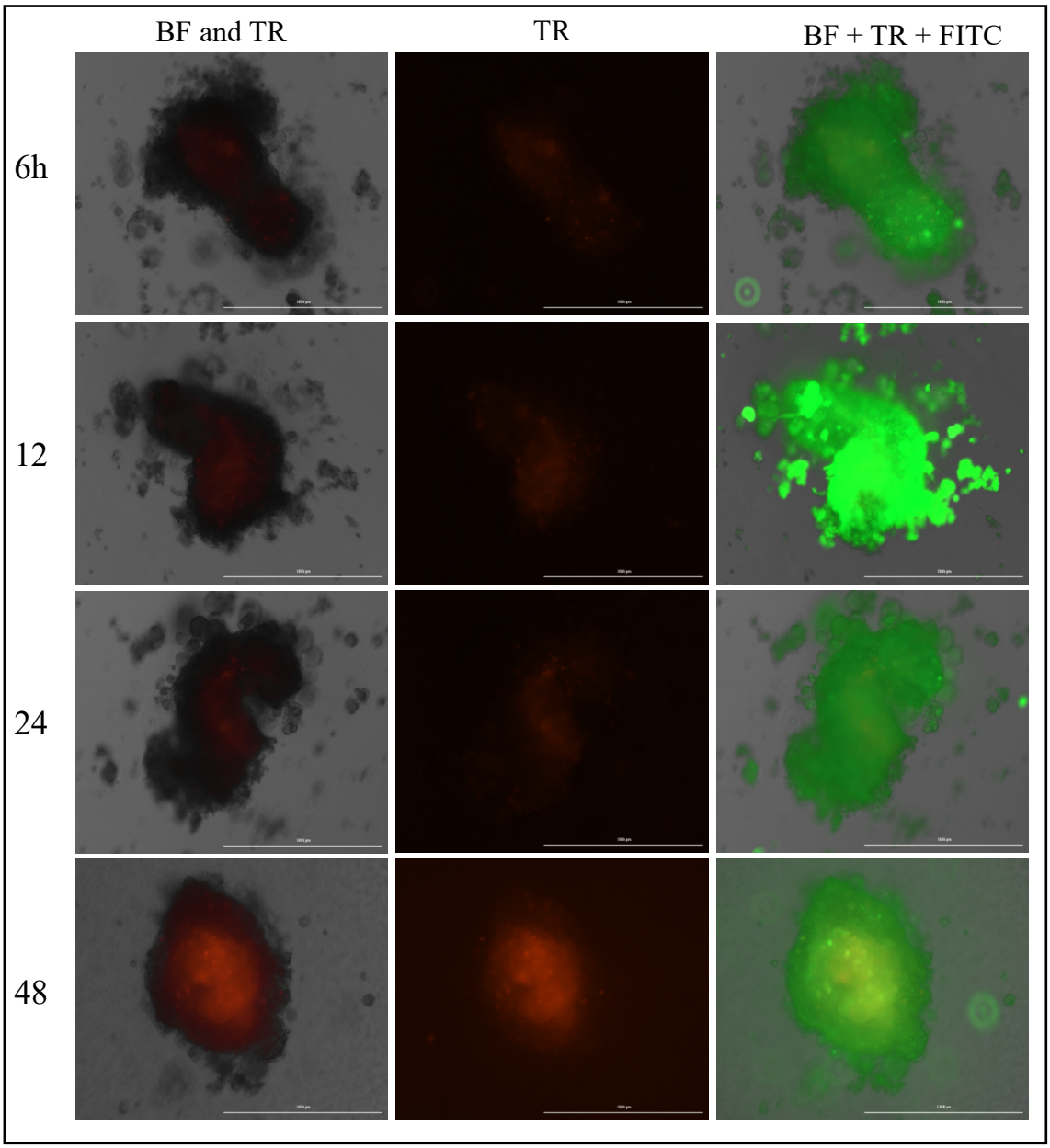

Figure 3.16

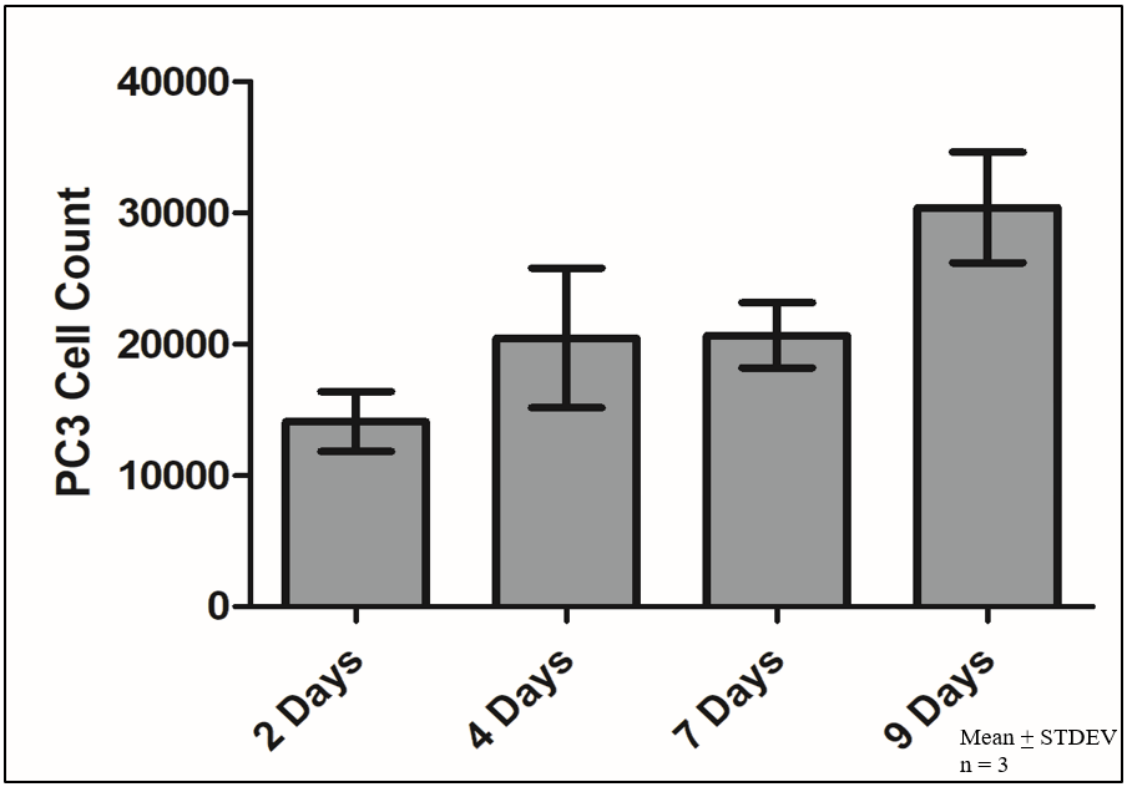
40000
30000
20000
10000
0
PC3 Cell Count
2 Days
4 Days
7 Days
9 Days
Mean ± STDEV
n = 3

Figure 3.17

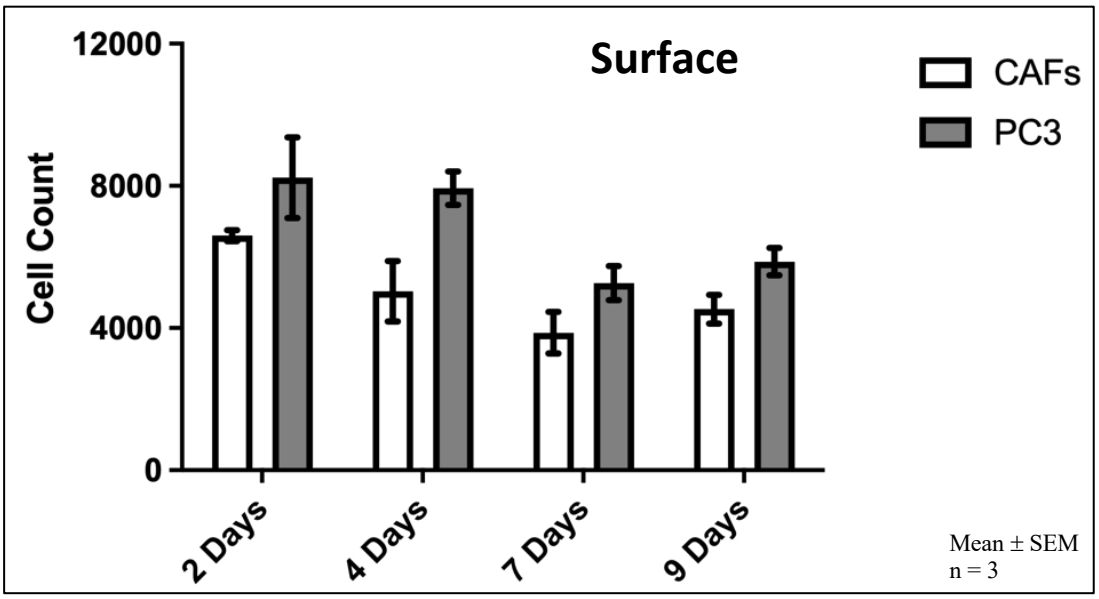
Surface
CAFs
PC3
Cell Count
12000
8000
4000
0
2 Days
4 Days
7 Days
9 Days
Mean ± SEM
n = 3

Figure 3.18

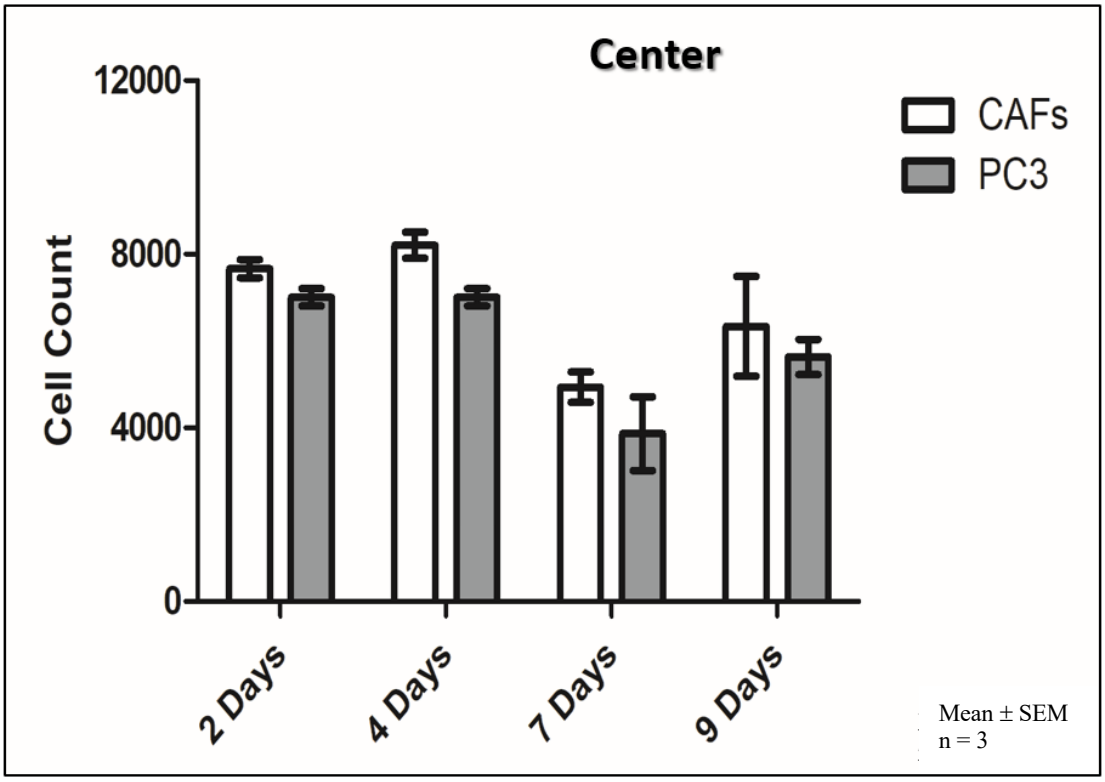
Center
12000
8000
4000
0
Cell Count
CAFs
PC3
2 Days
4 Days
7 Days
9 Days
Mean ± SEM
n = 3

Figure 3.19

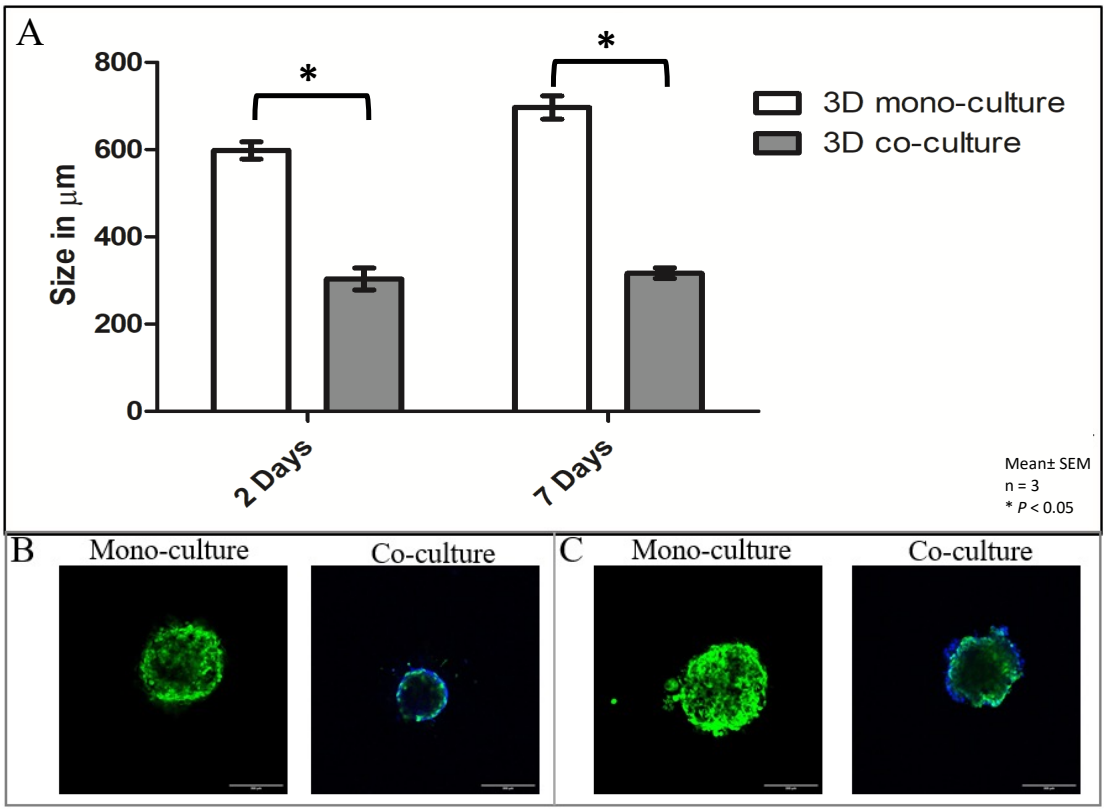
A
800
600
400
200
0
Size in μm
*
*
2 Days
7 Days
3D mono-culture
3D co-culture
Mean± SEM
n = 3
* P < 0.05
B
Mono-culture
Co-culture
C
Mono-culture
Co-culture

Figure 3.20

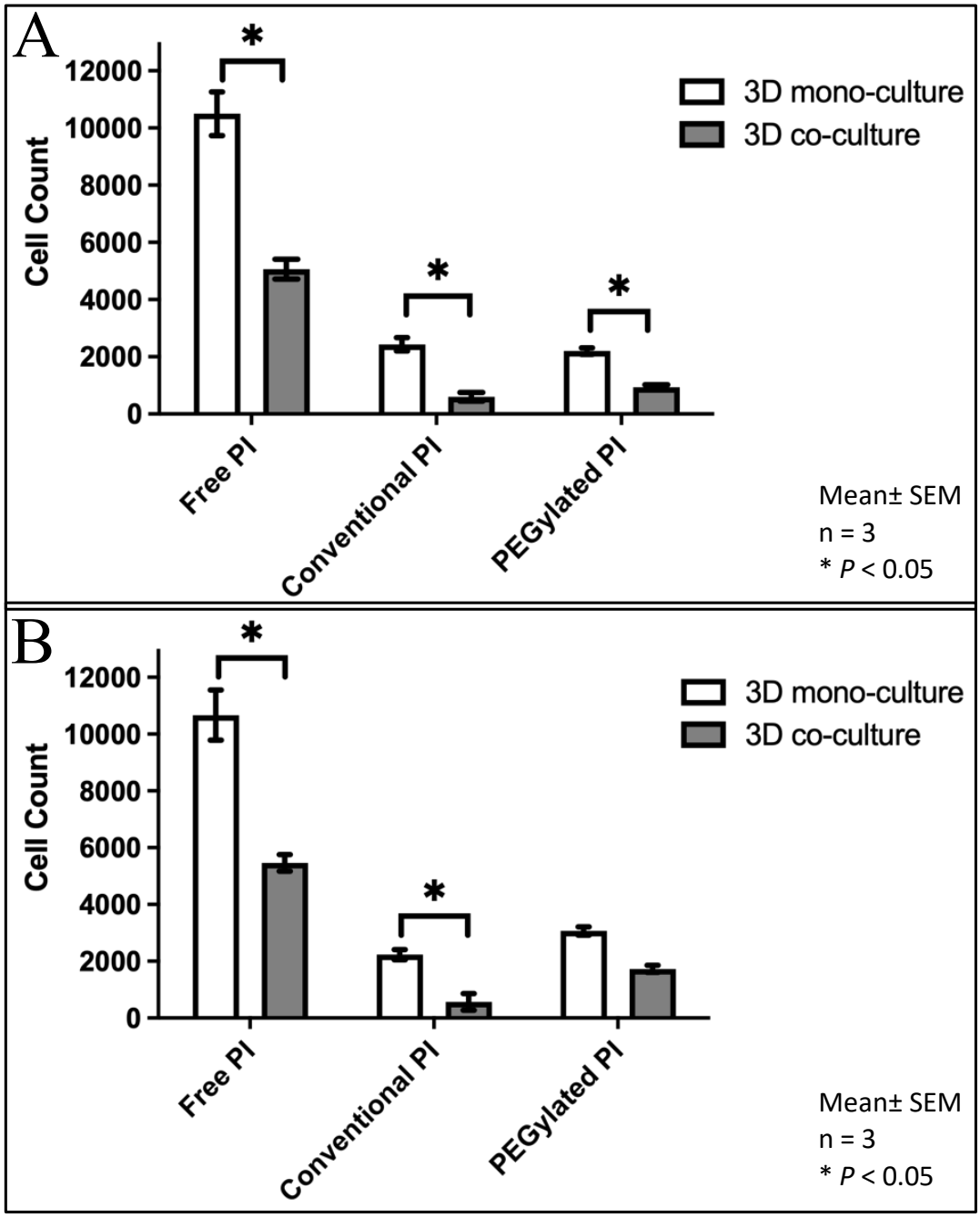
A
Cell Count
12000
10000
8000
6000
4000
2000
0
*
*
*
3D mono-culture
3D co-culture
Free PI
Conventional PI
PEGylated PI
Mean± SEM
n = 3
* P < 0.05
B
Cell Count
12000
10000
8000
6000
4000
2000
0
*
*
3D mono-culture
3D co-culture
Free PI
Conventional PI
PEGylated PI
Mean± SEM
n = 3
* P < 0.05

Figure 3.21

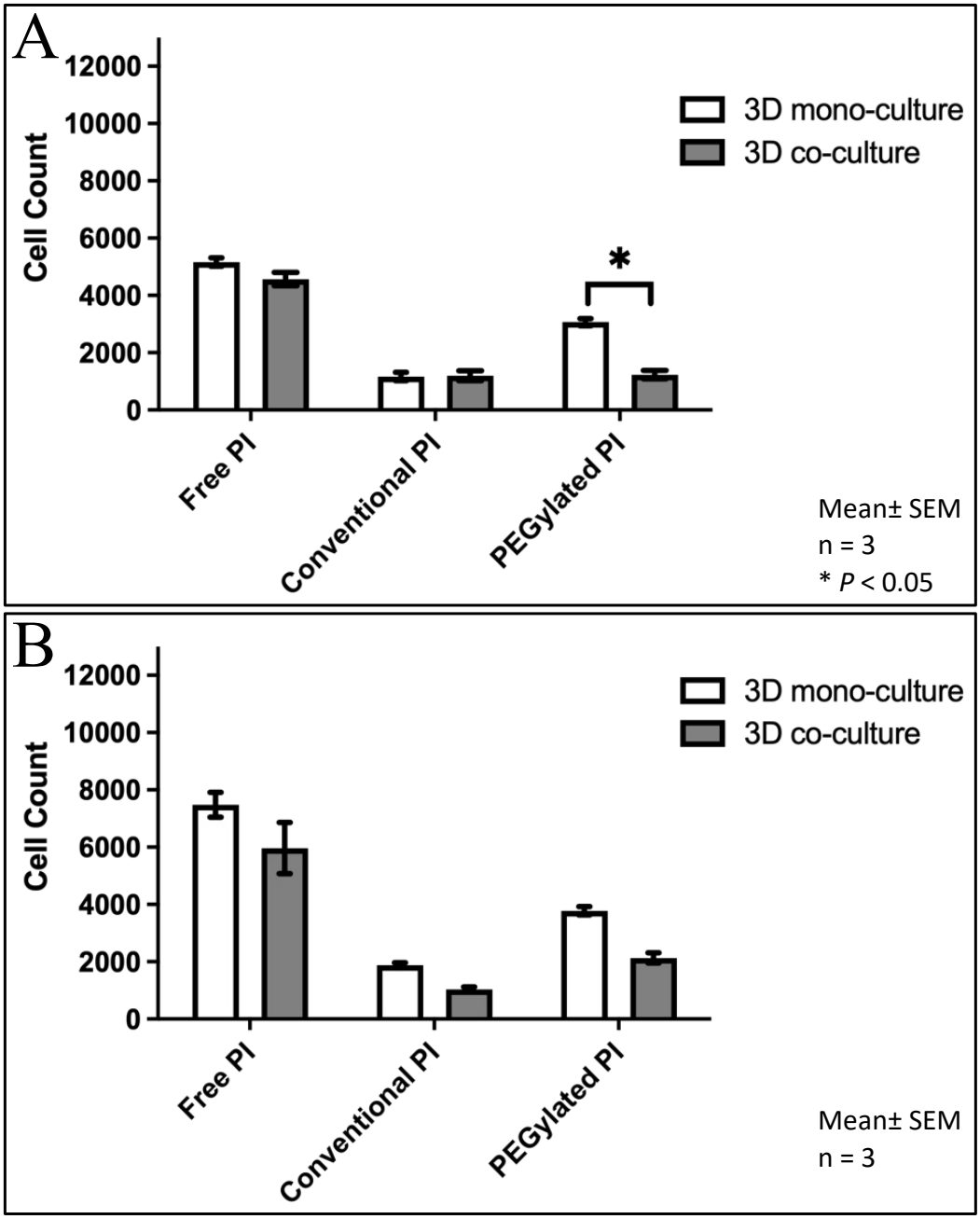
A
12000
10000
8000
6000
4000
2000
0
Cell Count
3D mono-culture
3D co-culture
*
Free PI
Conventional PI
PEGylated PI
Mean± SEM
n = 3
* P < 0.05
B
12000
10000
8000
6000
4000
2000
0
Cell Count
3D mono-culture
3D co-culture
Free PI
Conventional PI
PEGylated PI
Mean± SEM
n = 3

Figure 3.22

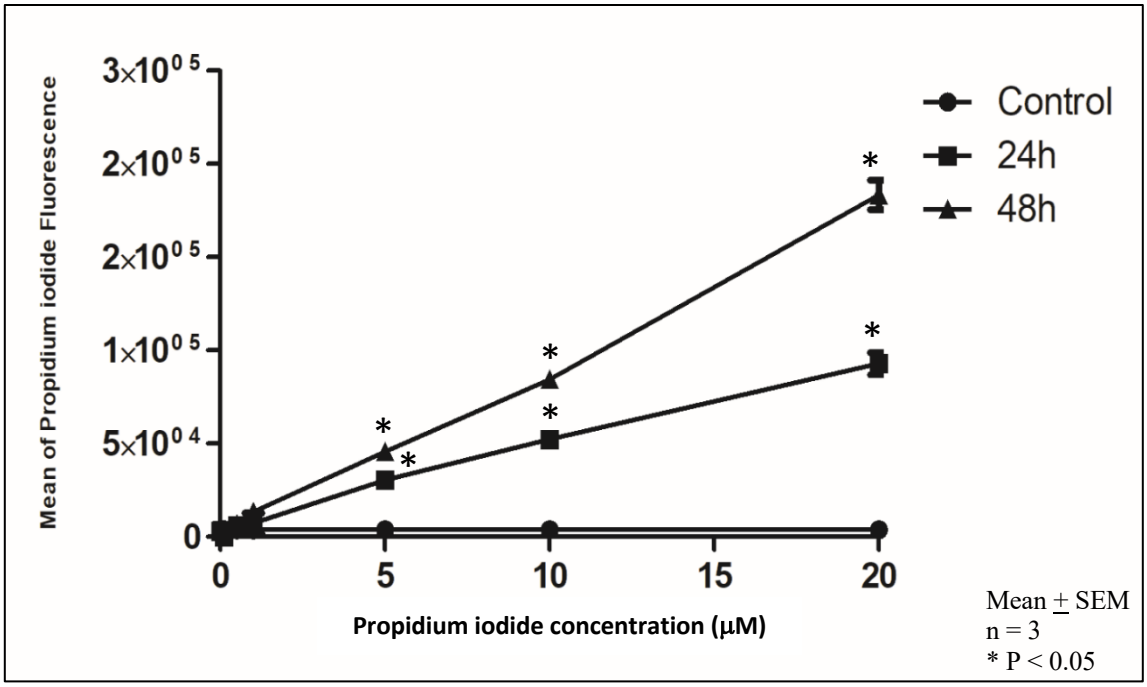
Mean of Propidium iodide Fluorescence
3×10^05
2×10^05
2×10^05
1×10^05
5×10^04
0
0
5
10
15
20
Propidium iodide concentration (μM)
Control
24h
48h
*
Mean ± SEM
n = 3
* P < 0.05

Figure 3.23

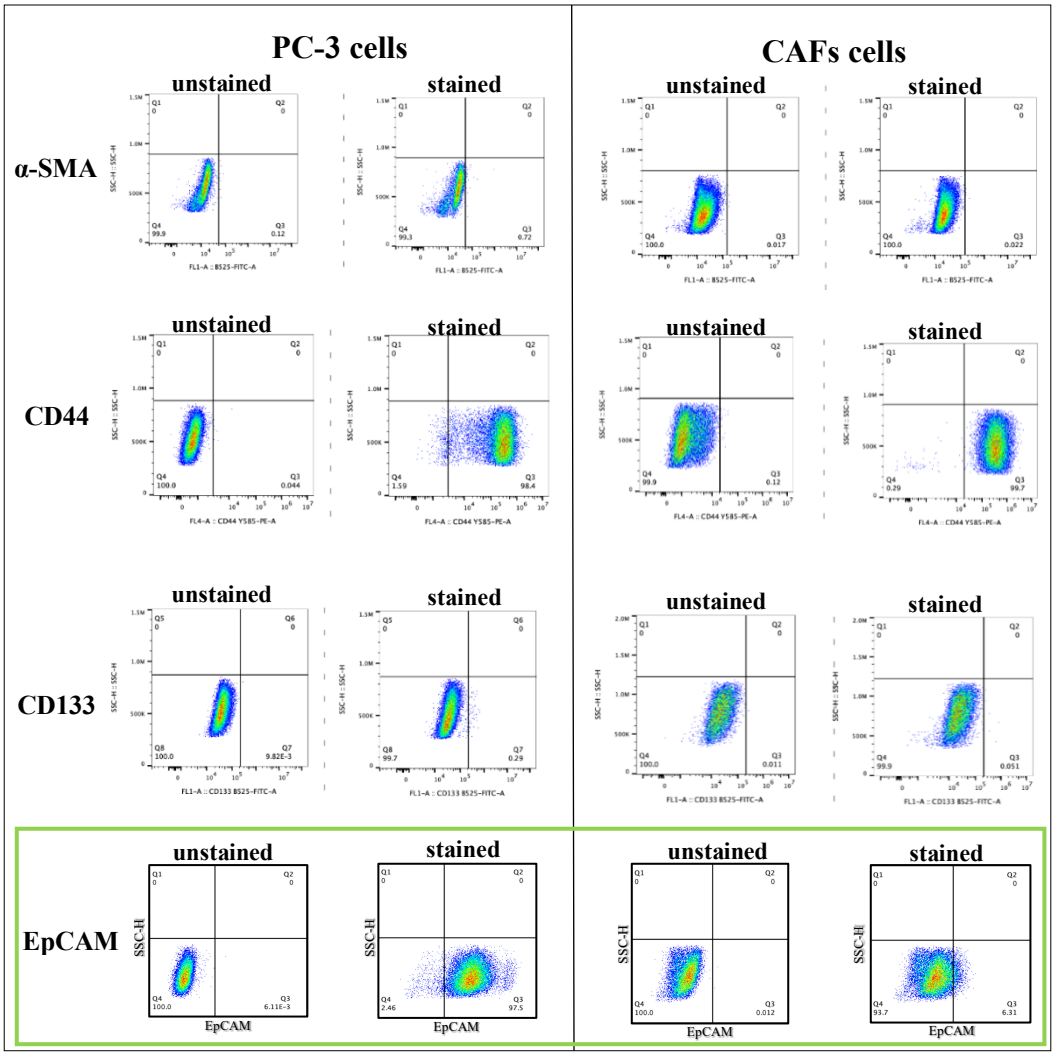
PC-3 cells
CAFs cells
unstained
stained
α-SMA
CD44
CD133
EpCAM
SSC-H
EpCAM

Figure 3.24

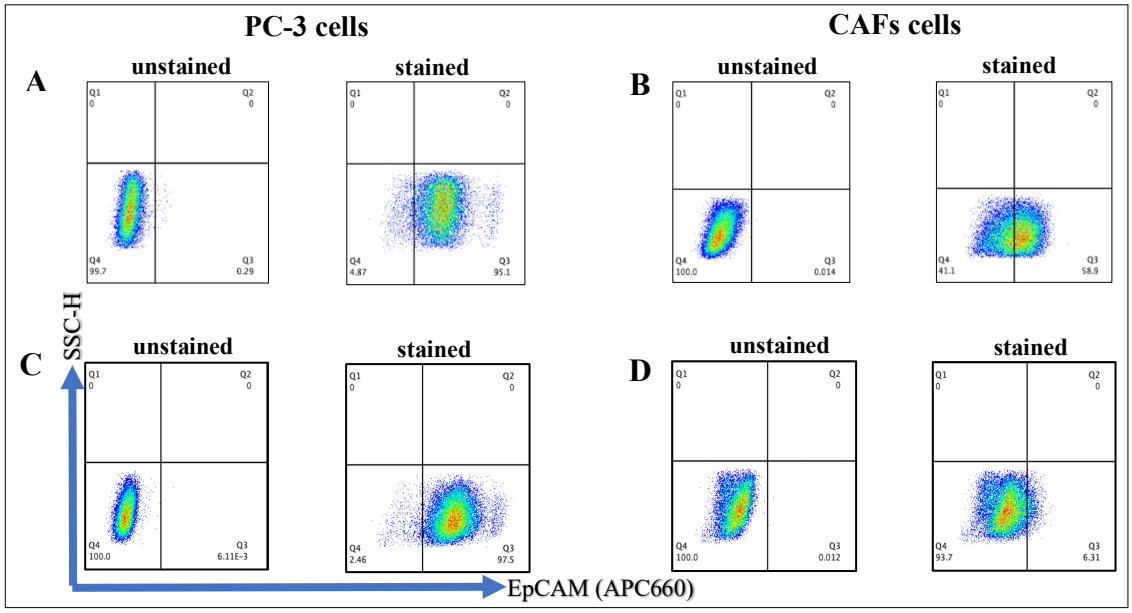
PC-3 cells
CAFs cells
A
unstained
stained
B
unstained
stained
C
unstained
stained
D
unstained
stained
SSC-H
EpCAM (APC660)

Figure 3.25

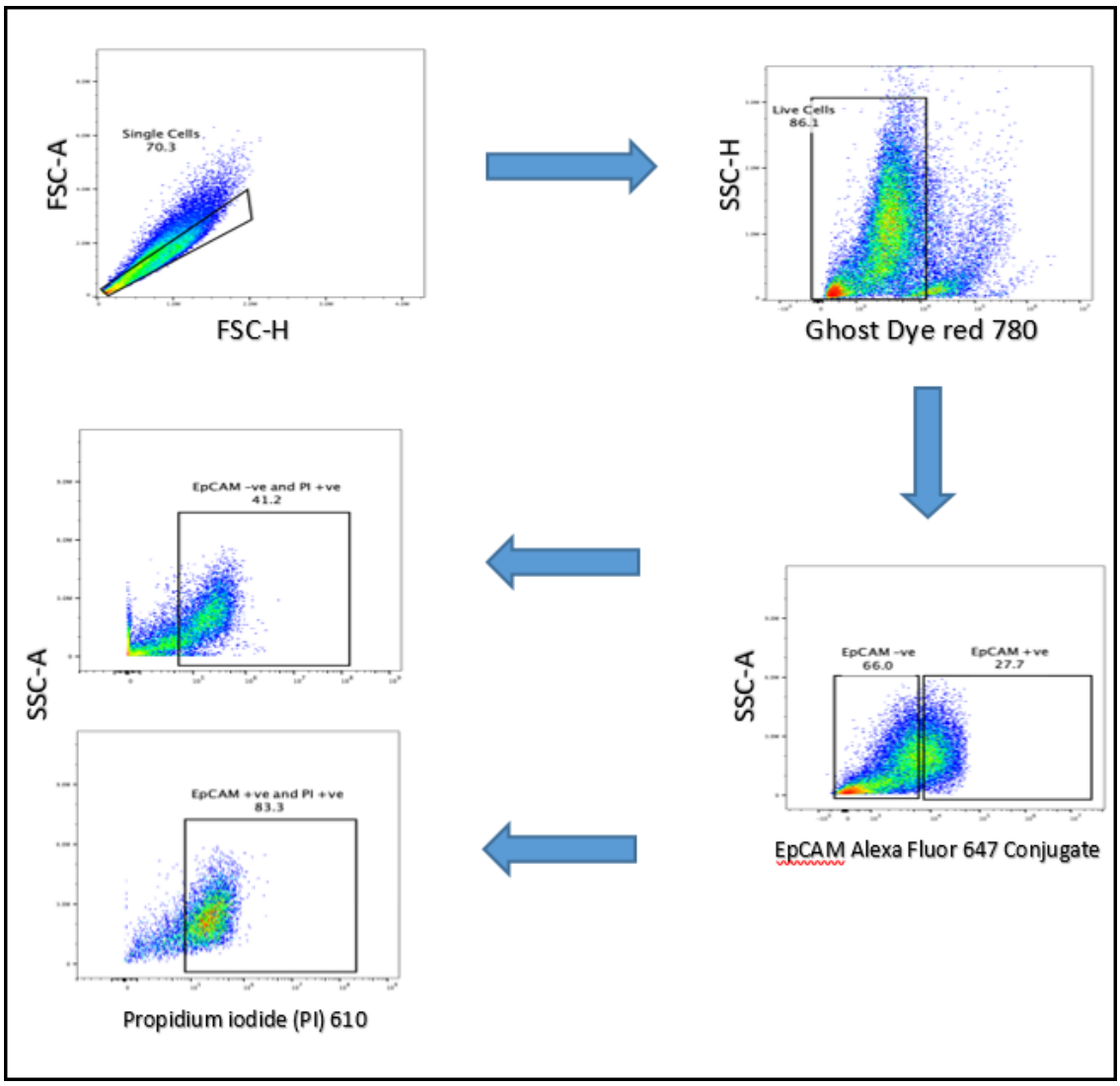
FSC-A
Single Cells
70.3
FSC-H
SSC-H
Live Cells
86.1
Ghost Dye red 780
SSC-A
EpCAM -ve
66.0
EpCAM +ve
27.7
EpCAM Alexa Fluor 647 Conjugate
SSC-A
EpCAM -ve and PI +ve
41.2
EpCAM +ve and PI +ve
83.3
Propidium iodide (PI) 610

Figure 3.26

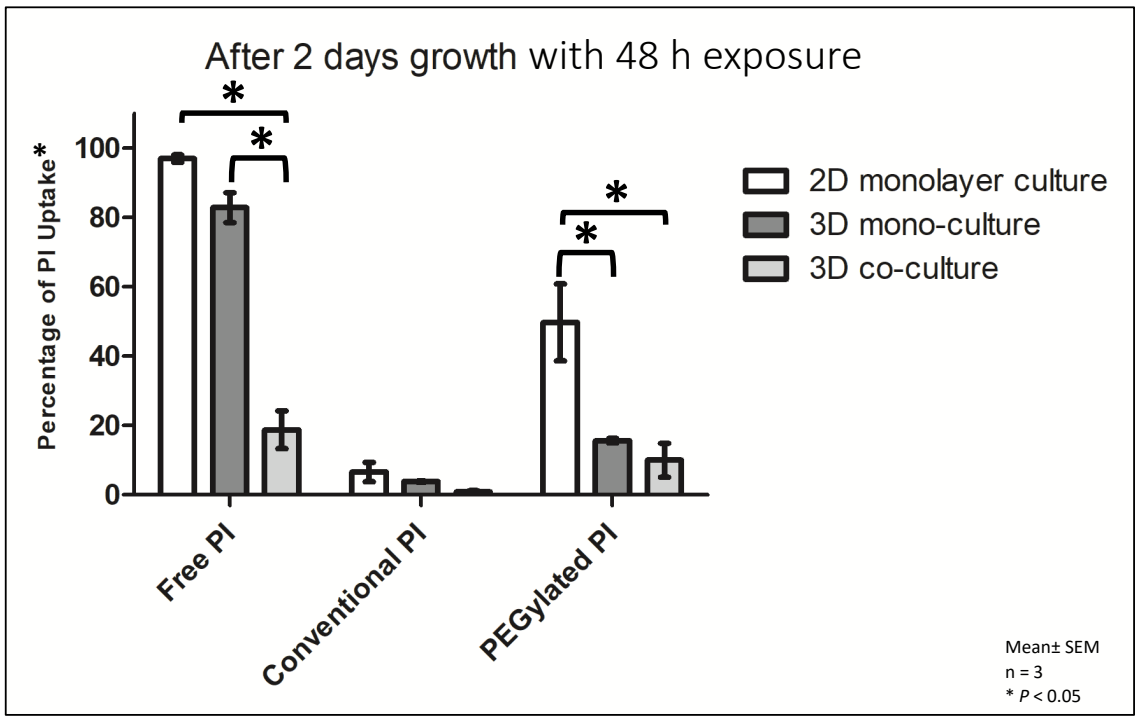
After 2 days growth with 48 h exposure
Percentage of PI Uptake*
100
80
60
40
20
0
*
*
*
*
2D monolayer culture
3D mono-culture
3D co-culture
Free PI
Conventional PI
PEGylated PI
Mean± SEM
n = 3
* P < 0.05

Figure 3.27

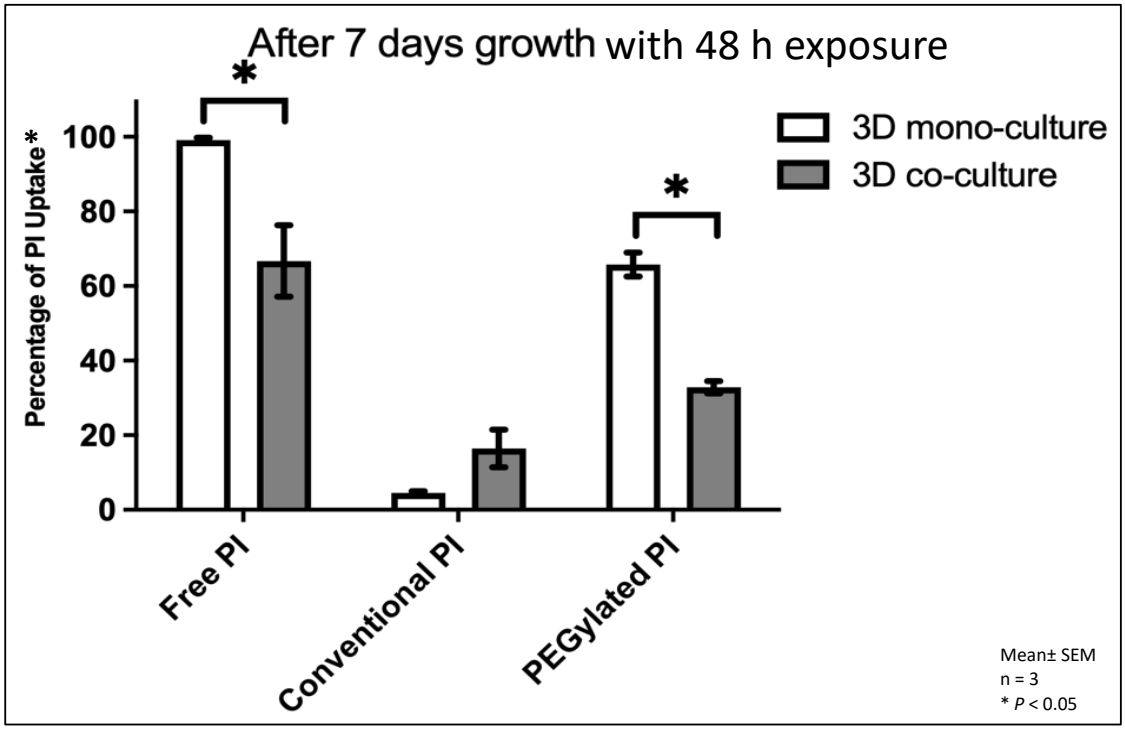
After 7 days growth with 48 h exposure
Percentage of PI Uptake*
100
80
60
40
20
0
*
*
3D mono-culture
3D co-culture
Free PI
Conventional PI
PEGylated PI
Mean± SEM
n = 3
* P < 0.05

Figure 3.28

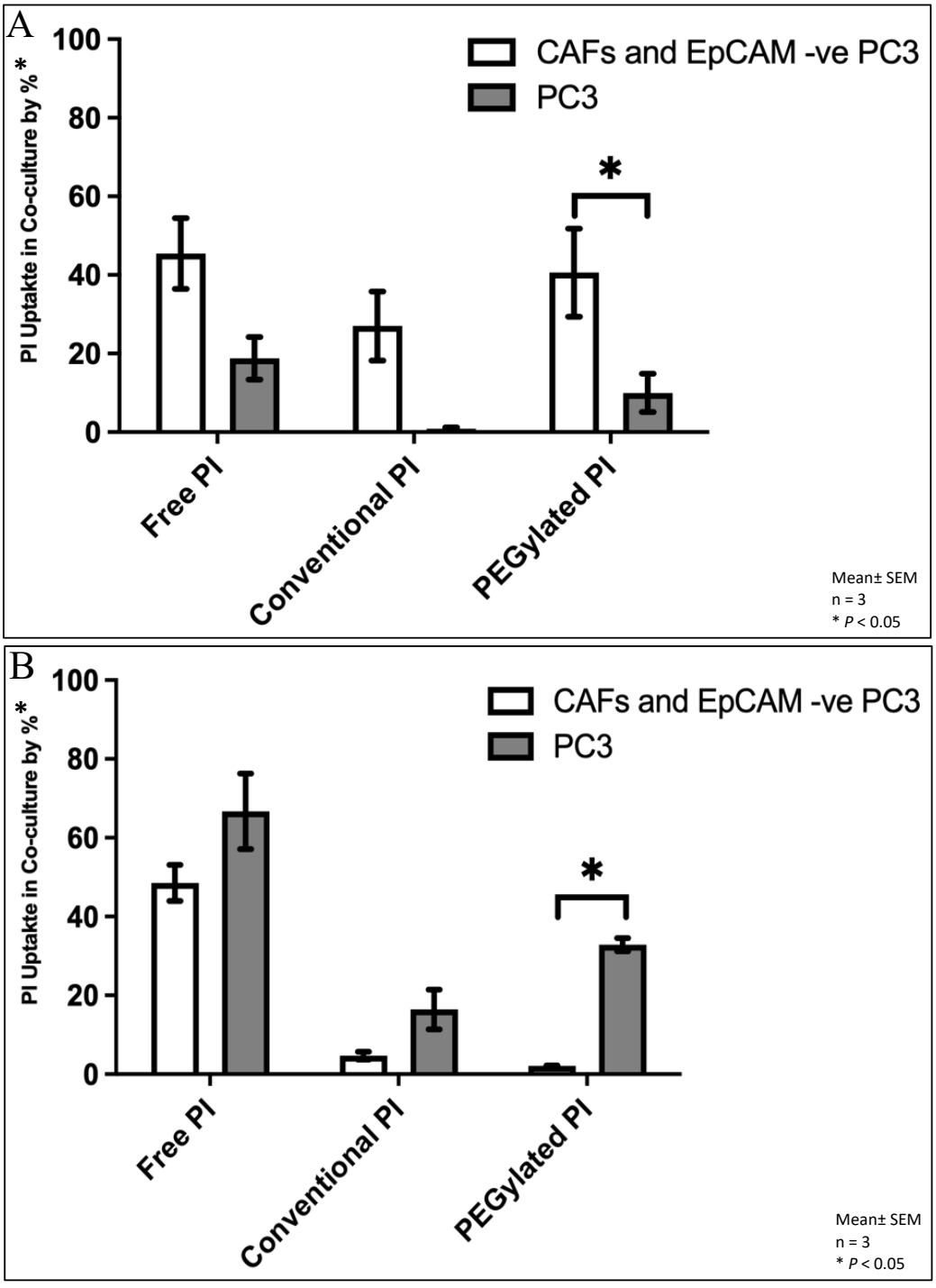
A
PI Uptakte in Co-culture by %*
100
80
60
40
20
0
CAFs and EpCAM -ve PC3
PC3
*
Free PI
Conventional PI
PEGylated PI
Mean± SEM
n = 3
* P < 0.05
B
PI Uptakte in Co-culture by %*
100
80
60
40
20
0
CAFs and EpCAM -ve PC3
PC3
*
Free PI
Conventional PI
PEGylated PI
Mean± SEM
n = 3
* P < 0.05

Figure 3.29

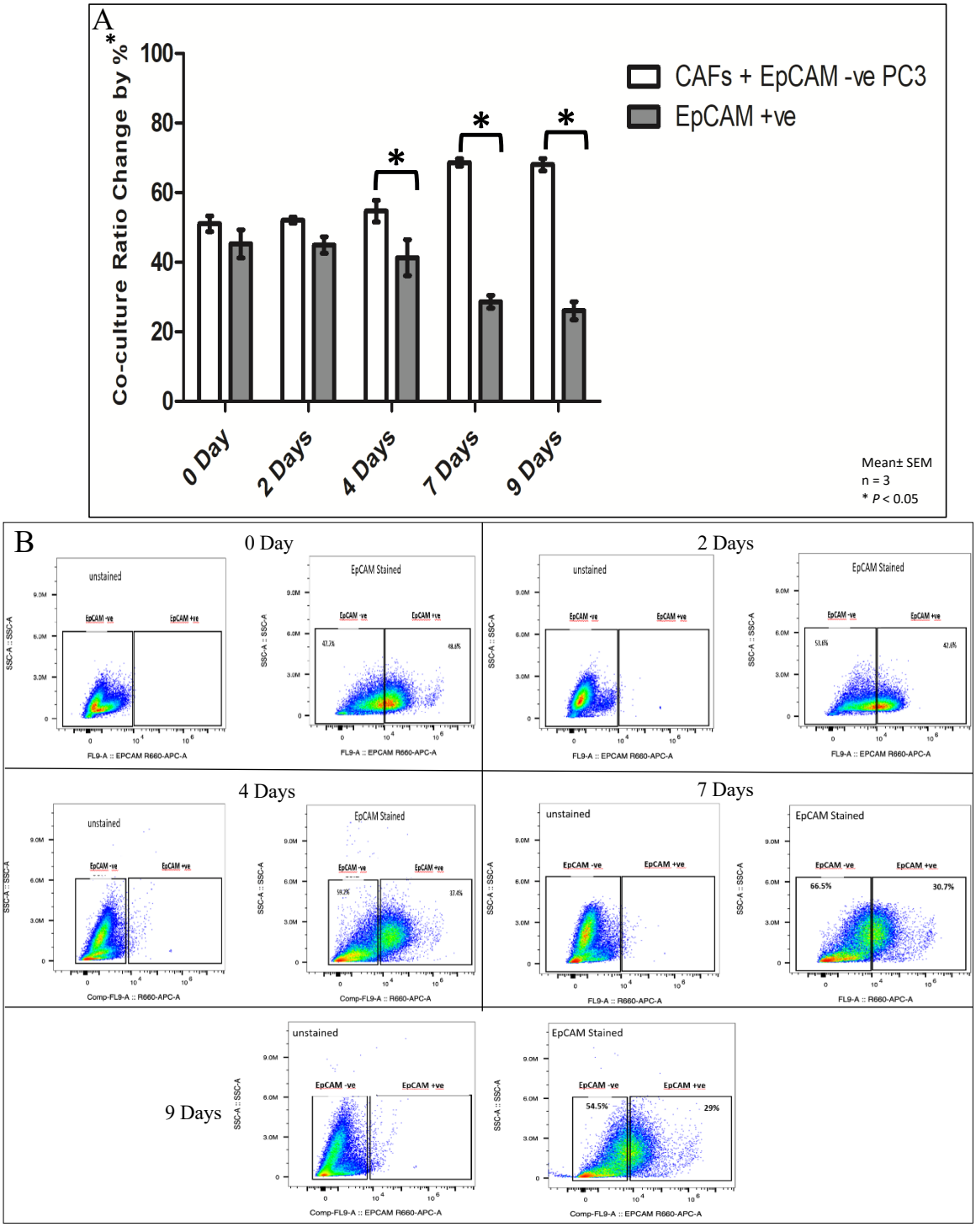
A
Co-culture Ratio Change by %
100
80
60
40
20
0
*
*
*
CAFs + EpCAM -ve PC3
EpCAM +ve
0 Day
2 Days
4 Days
7 Days
9 Days
Mean± SEM
n = 3
* P < 0.05
B
0 Day
unstained
EpCAM Stained
2 Days
4 Days
7 Days
9 Days
EpCAM -ve
EpCAM +ve
47.7%
49.6%
53.6%
42.6%
59.2%
37.4%
66.5%
30.7%
54.5%
29%

Figure 3.30


Z-score
-1.59
0
1.86
CTRL (control) spheroid day 0
CTRL spheroid day 3
CTRL spheroid day 7
Untreated
Untreated
HAS3
CD55
ANXA2P2
CD44
TGFBR2
AHNAK2
CD109
LOXL2
EPCAM
UCHL1
ANXA3
VIM
FSCN1
S100A6
ANXA2
TGFB1

Figure 3.31

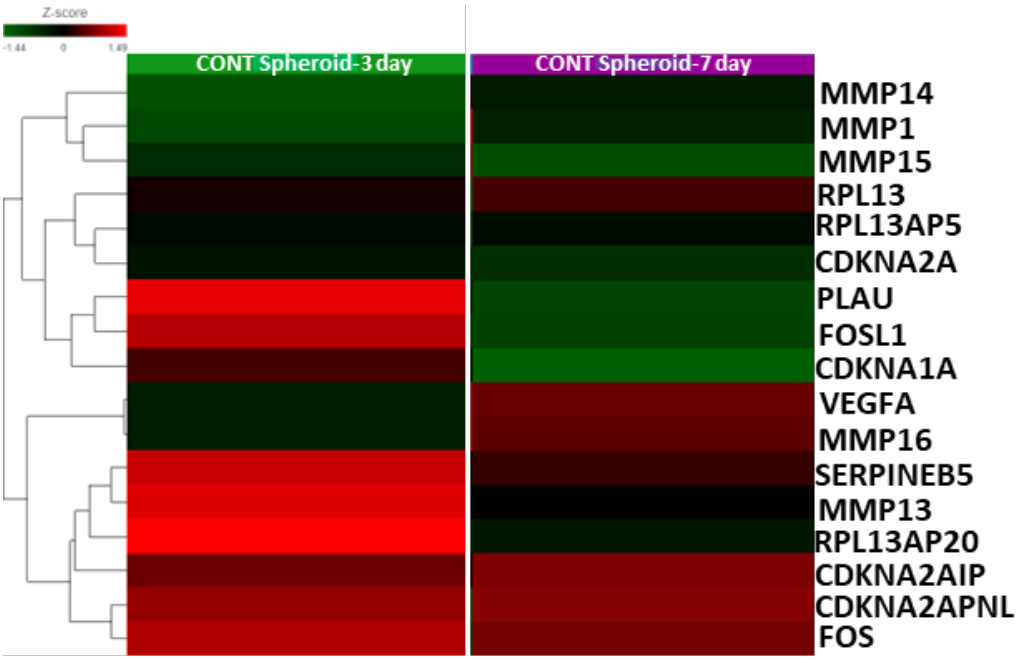
Z-score
-1.44
0
1.49
CONT Spheroid-3 day
CONT Spheroid-7 day
MMP14
MMP1
MMP15
RPL13
RPL13AP5
CDKNA2A
PLAU
FOSL1
CDKNA1A
VEGFA
MMP16
SERPINEB5
MMP13
RPL13AP20
CDKNA2AIP
CDKNA2APNL
FOS

Figure 3.32

3.13 References

1. Liu Y, Peterson DA, Kimura H, Schubert D. Mechanism of cellular 3-(4,5-dimethylthiazol-2-yl)-2,5-diphenyltetrazolium bromide (MTT) reduction. *J Neurochem*. 1997;69(2):581-593. doi:10.1046/j.1471-4159.1997.69020581.x
2. Aljuffali IA, Mock JN, Costyn LJ, et al. Enhanced antitumor activity of low-dose continuous administration schedules of topotecan in prostate cancer. *Cancer Biol Ther*. 2011;12(5):407-420. doi:10.4161/cbt.12.5.15950
3. Mitra Ghosh T, White J, Davis J, et al. Identification and Characterization of Key Differentially Expressed Genes Associated With Metronomic Dosing of Topotecan in Human Prostate Cancer. *Front Pharmacol*. 2021;12(December):1-19. doi:10.3389/fphar.2021.736951
4. Leary E, Rhee C, Wilks BT, Morgan JR. Quantitative Live-Cell Confocal Imaging of 3D Spheroids in a High-Throughput Format. *SLAS Technol*. 2018;23(3):231-242. doi:10.1177/2472630318756058
5. Quach ND, Mock JN, Scholpa NE, et al. Role of the phospholipase A2 receptor in liposome drug delivery in prostate cancer cells. *Mol Pharm*. 2014;11(10):3443-3451. doi:10.1021/mp500174p
6. Gopal S, Kwon SJ, Ku B, Lee DW, Kim J, Dordick JS. 3D tumor spheroid microarray for high-throughput, high-content natural killer cell-mediated cytotoxicity. *Commun Biol*. 2021;4(1):1-14. doi:10.1038/s42003-021-02417-2
7. Manohar SM, Shah P, Nair A. Flow cytometry: principles, applications and recent advances. *Bioanalysis*. 2021;13(3):181-198. doi:10.4155/bio-2020-0267
8. Canals Hernaez D, Hughes MR, Li Y, et al. Targeting a Tumor-Specific Epitope

on Podocalyxin Increases Survival in Human Tumor Preclinical Models. *Front Oncol*. 2022;12(May):1-14. doi:10.3389/fonc.2022.856424

9. Kuonen F, Touvrey C, Laurent J, Ruegg C. Fc block treatment, dead cells exclusion, and cell aggregates discrimination concur to prevent phenotypical artifacts in the analysis of subpopulations of tumor-infiltrating CD11b(+) myelomonocytic cells. *Cytom Part A J Int Soc Anal Cytol*. 2010;77(11):1082-1090. doi:10.1002/cyto.a.20969

CHAPTER 4

DISCUSSION, FUTURE DIRECTIONS, AND CONCLUSION

4.1 Discussion

There has been a number of clinically approved nano products since the 1990s. While they have shown clinical utility, their overall promise has not been fully realized. While there has been an exponential growth in the numbers and types of nanoparticles that are being prepared, there are still fundamental gaps in knowledge related to how they accumulate and distribute within solid tumors, and how the tumor microenvironment can alter their performance.

Our goal was to gain insights into the role of the nanoparticle and not a specific anticancer drug. In these studies, we were not interested in looking at cytotoxic effects on the cancer cells, rather, we desired to use a fluorescent dye that is relatively not toxic, at least at the concentration we used in these studies. We also aimed to provide a stable entrapment of the fluorescent dye in the formulations, so we could anticipate the distribution and uptake of those formulations. Further, we investigated a fluorescent dye that if it released from the formulations, it cannot be easily taken up by the cells. Earlier, our lab and others have encapsulated and used 6-carboxyfluorescein (6-CF) as a probe within liposome[1]; however, when 6-CF is released it is taken up by cells quickly, and it showed concentration and environment effects. While its release has been used as a marker of liposome membrane integrity, its ability to track the intracellular uptake of liposomes was limited.

Propidium iodide (PI) is a red fluorescent dye that binds to DNA, and it is widely described in the literature as a probe that cannot passively cross intact cell membranes, and for that reason, it only stains dead cells that have compromised cell membrane[2]. We hypothesized that PI could be used to track the intracellular distribution of liposomes. If a

liposome membrane was compromised, for example, degraded by enzymes or proteins secreted by cancer cells or in the tumor microenviomrent[3], and PI was released, then, we believed the PI would not cross live cells' membrane and no intercellular PI staining would be observed in live cells. If PI staining was observed in live cells, this would suggest that liposomes were taken up into the cells as a whole and intact particles, and later they degraded and released the PI inside the live cells.

To verify the PI's ability to be used in our study, we determined its cytotoxicity in the PC-3 cells using the MTT assay. In our study, after 48 h of the incubating different concentration of the PI, we found that up to 15 μM of the PI there was no change in MTT staining, but higher concentrations decreased the MTT staining suggesting the presence of toxicity. Based on these data, we choose to use a concentration of 10 μM PI that was not toxic when it was incubated for 48 h in PC-3 cells. Furthermore, we wanted to verify that our empty (drug free) liposomes were not introducing any toxicity when dosed over the cells for 48 h. Based on the MTT assay and examining high and low concentrations of our liposome formulations, we did not observe any cytotoxicity.

Ethanol is an organic solvent and known to dissolve lipids in liposomes at concentrations over 50-60%[4]. We have used pure ethanol to dissolve liposomes and release the PI so we can quantify its concentration. We determined that it can take up to an hour and may require sonication to fully dissolve the lipids and yield a clear solution. We added 200 μl of ethanol to 50 μl of liposomes with PI and liposomes free of PI to ensure the lipids do not interfere with the readings. This resulted in a final alcohol concentration of 80% (v/v) with 10 mM of lipid. While PI has been used widely as a live/dead stain, there were no assays that described its quantification in organic solvents,

such as absolute alcohol. Though we had a clear solution to quantify the PI concentration, we had to develop a method to quantify the PI in ethanol and demonstrate that lipids in the sample would not interfere with the assay. Accordingly, we dissolved different high to low PI concentrations in ethanol and determined the excitation and emission using a SpectraMax iD3 plate reader with SoftMax Pro 7.1 software. The results showed that the PI excitation/emission maxima were obtained at 545/650 nm. Additionally, we showed the overall linear range of the assay and identified the limit of quantification (LOQ) of the PI is 7.8 μM, with +/-10% accuracy and CV% <15%. We used the assay to optimize PI-liposome formulations. We examined the recovery and EE of PI in a conventional and PEGylated liposome formulation. First, we loaded different concentrations of the PI into the liposomes using the aqueous capture method. The results showed that the PI-recovery % was similar (12±3%) when we loaded 1 and 0.5 mM of the PI. This means that 1 mM of the PI resulted in 0.12 mM, and 0.5 mM of the PI resulted in 0.6 mM. Moreover, the encapsulation efficiency (EE) was 8.3±2.42% for 1 mM PI and 10.18±4.63% for the 0.5 mM; therefore, as the EE is too low, we preferred to use the higher PI concentration (1 mM). We desired to use higher concentrations of the PI, but the PI solubility is very low (1 mg/ml = 1.5 mM) in normal saline (0.9 % NaCl). We also tried lower concentrations, but they were below the LOQ. The goal is to enable detecting the PI uptake when the liposomes are taken up. Our study showed that the free PI is significantly (P<0.05) taken up by the cells at the concentration 5 μM after 24 and 48 h. Since the encapsulated PI (10 μM) leaks at most 15%, it would not significantly be quantified as uptake in the cells. Therefore, identifying the PI inside the cells when encapsulated in liposomes, means that the liposomes were taken up and released ≥5 μM of the encapsulated PI in the cells.

After verifying the PI and the liposomes' non-toxicity at the concentrations we used in our study and knowing how much PI we can encapsulate in the liposomes, we studied the PI stability in the liposomes when exposed to biological conditions (serum-supplemented media at 37°C) for 72 h. Jan Karlsen et al. introduced the dialysis method to study the drug release from liposomes in 1995, called fractional dialysis[5]. Prior to beginning the stability experiments we determined we were not able to measure leaked, free PI in the dialysate, because it was below the LOQ for our assay. Therefore, we adapted the assay and measure the change in PI from within the dialysis bags due to leakage. We collected samples at different time points, and the first time point after the study started was at 5 h. We used one of the controls as a free PI in the dialysis bags, and we could not detect any PI in the bag after the first time point (5 h), meaning that the PI could leak from the dialysis bags if released from the liposomes. The study showed that the conventional and the PEGylated liposomes stably entrapped the PI, and the total leak of the PI after 72 h did not exceed 15%. This suggests that if the formulations were dosed with PI final concentration at 10 μM, it would leak only 1.5 μM at maximum release cases. As we described earlier, the lowest concentration of the PI that can show significant uptake in the cells is 5 μM; accordingly, if we see the uptake of the PI that is encapsulated in liposomes, this indicates that the formulations are taken up by the cells and released the PI.

While the uptake of PI is generally thought to only occur in dead cells, we conducted a variety of control studies in our system. Unfortunately, when we incubated the free PI with the cells, we showed that the free PI (at what concentration) is taken up by live cells when incubated for more than 6 h. While the goal of this research was not to delineate the

mechanism of PI uptake, Marlon J. Hinner, et. al., has described how small molecules are able to traverse the cell membrane, as non-specific internalization of fluid occurs in all cells, called pinocytosis[6]. However, since our formulations stably entrapped the PI, it was possible to consider using the free PI as a positive control for internalizing the dye after 48 h exposure.

Liposome characterization assays are essential to demonstrate our ability to reproducibly prepare different liposomes formulations. Characteristics, such as size distributions, zeta potentials, electrophoretic mobility (charge), and phosphate concentration were used after each liposome preparation.

The size distributions of the liposomes were measured using the dynamic light scattering (DLS), which measures the size distribution of the nanoparticles based on time-dependent intensity fluctuations in scattered laser light. It calculates the particle's size according to the rate of fluctuation of scatted light intensity, where the small particles diffuse more rapidly than large particles[7]. Different parameters can be acquired from the DLS to express the size distribution of the NPs, such as intensity and volume. However, it has been known that when the polydispersity index (PDI) is narrow (<0.1); then, both parameters (intensity and volume) would be close to each other because the samples are monodisperse[8]. Our study showed that the conventional liposome size distribution by volume was 105-125 nm, and the PEGylated liposomes were 110-130 nm. These sizes are important because they provide an advantage of EPR and re similar to those that clinically used.

The zeta potential of the NPs is an important parameter since it shows the stability of the particles in a suspension. The zeta potential depends on the particle's charge

(electrophoretic mobility), which is the potential difference between the stationary layer (dispersion medium attached to dispersion particles) and the mobile dispersion medium[9]. The higher charge values (≥ 30 or ≤ -30), the lower particles coalescence. Our formulations showed -29±2 mV for the PEGylated liposomes and 20±2 mV for the conventional liposomes, meaning we expected higher stability of the PEGylated liposomes than the conventional liposomes. The reason behind having the higher stability of the PEGylated liposomes has the PEG chain that reduces the interactions between the surfaces. Andreas et al. explained how the high zeta potential brought more stability and showed how the PEG increased stability to the NPs[10]. The electrophoretic mobility is the particles' response to the applied electrical field (anions move toward the positively charged anode, cations move toward the negatively charged anode, and neutral species remain stationary) and, therefore, it can express the particles' actual charge[11]. The PEGylated liposomes charge showed as -2±0.15 μmcm/Vs, and the conventional liposomes charge showed as 1.5±0.15 μmcm/Vs. The net negative charge in the PEGylated liposomes is due to the conjugation of PEG-DSPE [10 mole percent (based on lipid)] to DSPC.

Further, we performed stability studies of the formulations after 72 h exposure to biological conditions (serum-supplemented media at 37°C). We found that the conventional liposomes' size distributions increased by around 22%, the charge was changed from 1.5±0.15 to -0.3±0.25 μmcm/Vs and the zeta potential dropped from 20±2 to -4.5±2.6 mV. On the other hand, the PEGylated liposomes showed greater stability where their size distributions increased only 0.6%, the charge changed from -2±0.15 to -1.5±0.2 μmcm/Vs and the zeta potential dropped from -29±2 to -19.4±2 mV. As the

conventional liposomes exposed higher changes in their characteristics, such as the high increase of size and reduce of zeta potential, it indicated that the particles are not stable in the solution compared to the PEGylated liposomes, which they exposed lower changes.

Recent studies demonstrate that the tumor microenvironment (TME) plays an important role in altering the barrier properties of solid tumors that affect the therapeutic response[12]. TME comprises different stromal cells (CAFs, immune cells, endothelial cells (ECs), etc.) and extracellular matrix (ECM) components (growth factors, cytokines, hormones, etc.)[13]. All these components surround the tumor cells and support their progression and metastasis. All stromal cells are not malignant; however, due to their interactions with the cancer cells, they acquire protumor functionality[14].

CAFs are one of the major stromal cells that provide many protumor functionalities to the tumor, such as increased tumor growth by changing metabolic effects (lactate, alanine, and aspartate shuttling and amino acid depletion), increased cancer cells invasion by remodeling the matrix (matrix crosslinking, proteolysis, force-mediated matrix remodeling, and matrix production), and involved in macrophage and endothelial crosstalk through the secretion of soluble factors (exosomes and vascular endothelial growth factor (VEGF))[15]. All these functionalities that are mediated by CAFs can contribute to the failure of NPs and their payloads from effectively reaching and acting on cancer cells[16].

One challenge in accessing effect of nanoparticles and TME is the diversity of cell types. Here we chose to use flow cytometry because it is capable of measuring multiple markers in a large number of cells rapidly. Furthermore, specificity can be achieved by using labeled antibodies that are specifically generated against different biological

molecules (markers), such as proteins, cytokines, glycolipids, *etc.* In flow cytometry, antibodies are developed to help detect a specific marker in a sample[17]. As our study has a co-culture model combining PC-3 with CAFs cells, we needed to separate these cells for further analysis. Hence, we investigated different antibody markers. Since PC-3 cells are epithelial cells, and CAFs are known for their negative consist of epithelial proteins[18], we examined EpCAM (epithelial Cell Adhesion Molecule) antibody. Our study showed that the EpCAM is highly conjugating with PC-3 cells, but it has some conjugation with the CAFs cells. We revised our staining protocol to minimize non-specific binding. As the antibodies have the Y shape, their specific binding sites are meant to be with light chains; yet they can non-specifically bind through their heavy chain and produce false-positive[19]. To avoid that, protein blocking reagents such as bovine serum albumin (BSA), fetal bovine serum (FBS), and Fc blocker[20]. In our older protocol, we used a 10 % (v/v) FBS buffer in a 0.5 % (w/v) BSA buffer to block the non-specific binding sites in the cells. When we used 2.5 % (v/v) Fc blocker in a 0.5 % (w/v) BSA buffer, it reduced the non-specific binding, making the EpCAM a good candidate as a specific marker for PC-3 cells. We also investigated different antibody markers, such as α-SMA (alpha-smooth muscle actin), which is known to be expressed in CAFs cells.[21] However, in our studies we showed no significant staining using two different antibodies for α-SMA. We also tested CD44, an aggregation and migration marker known to be expressed on the surface of the PC-3 cells[22], yet it showed significant binding in both cell types. CD133 is a stem cell marker also known to be expressed on the surface of the PC-3 cells[23], but no significant binding was shown. Accordingly, we used the EpCAM as a marker for the PC-3 cells, and the CAFs cells were identified as the –ve stain population of EpCAM. In

our study, we found that a fraction of the PC-3 cells lost EpCAM staining and became EpCAM negative after 4 days of the co-culture (PC-3 + CAFs) formation. This could indicate epithelial-mesenchymal transition (EMT). C.P. Hu et al. showed that CAFs induced EMT in lung cancer cells[63]. Accordingly, this is one of the future directions to study the EMT caused by CAFs when co-culture with cancer cells.

In our confocal studies, we used PC-3 cells that are GFP tagged and CAFs without fluorescent tag. To capture the CAFs cells, we had to search for an appropriate fluorescent dye that could stain the cells. After capturing the images with GFP and Hoechst 33342, we analyzed the GFP as the PC-3 cells and the Hoechst 33342 as PC-3 + CAFs. At the end of the analysis, we deducted the GFP cell number from the Hoechst33342 total to obtain the CAFs' cell number. This study aims to evaluate the role of CAFs when co-culturing with cancer cells (PC-3) and how they might affect the uptake or the distribution of the liposome NPs. Therefore, we have grown the co-cultured spheroids for 2 days and the others for 7 days to identify the uptake difference between them. We aimed to see how more prolonged interactions between CAFs and PC-3 cells would affect the uptake or distribution of the liposome NPs. We also compared the uptake of the liposomes NPs in the co-culture spheroids with mono-culture spheroids that had been treated the same as the co-culture spheroids. By using flow cytometry analysis after 2 days of the spheroids' growth, we noticed that both the co-culture and mono-culture spheroids had low uptake of the conventional-PI and PEGylated-PI liposomes. However, when spheroids were grown for 7 days, the PEGylated-PI liposomes showed significantly higher uptake in the 3D mono-culture spheroids compared to the 3D co-culture spheroids. This finding supports the literature claims that the CAFs hinder the

NPs and treatment uptake. This also suggests that when the CAFs had more prolonged exposure to the cancer cells, the CAFs showed their protumor functionalities. To validate these results, we used confocal imaging microscopy. However, since we could distinguish between each layer of the spheroids, we determined the uptake of the liposomes NPs in the surface and center of the spheroids. In the spheroids' surfaces, we found that the conventional-PI liposomes showed significantly higher uptake in the mono-culture spheroids after 2 and 7 days of the spheroids' growth compared to the co-culture spheroids. The PEGylated-PI liposomes also showed higher uptake in the mono-culture spheroids than the co-culture spheroids, but it was insignificant. In the center, we identified that the PEGylated-PI liposomes showed higher uptake in the mono-culture spheroids compared to the co-culture spheroids, but the significant measurement was when the spheroids were grown for 2 days. Therefore, the confocal imaging studies successfully validated the flow cytometry studies. Ultimately, the co-culture spheroids model showed lower uptake of the liposome NPs compared to the mono-culture spheroids model. This is also in agreement with clinical literature that suggests that the EPR effect is not as prevalent and intratumor distribution and cellular uptake are limited.

An interesting finding from this study is that when we co-cultured the CAFs with the PC-3 cells in spheroids, the growth of the spheroids was slower than the mono-cultured spheroids with only the PC-3 cells. This finding contradicts some of the literature claims. Guillaume Vogin et al. showed that when they co-cultured MCF-7 (luminal breast cancer) cells with MRC-5 (human embryonic fibroblasts) cells in the same ratio we used in our studies, the growth of their co-culture spheroids was higher than their mono-culture spheroids[24]. On the other hand, Chuaning Bao, et. al., co-cultured HCT-116

(human colorectal cancer) cells with SW620 (human colorectal CAFs) and showed that the CAFs caused reduce in the growth of the cancer cells[25]. Another study by Walnu Cao, et. al., concurs with our finding that they co-cultured FaDu (human pharynx squamous cell carcinoma) cells with MeWo (granular fibroblasts derived from human melanoma) cells in different ratios. None of the co-culture ratios showed an increase in the tumor growth compared to the mono-culture spheroids[26]. This is important because many anticancer agents target rapidly diving cells. The use of 2D and 3D models of tumor cells may not accurately recapitulate the temporal growth characteristics. Furthermore, NP formulations may not be prepared with optimal release rates based on tumor growth. Therefore, our study is aiming to mimic the actual tumor and identify the role of the TME factors in affecting the tumor growth and the delivery system.

Within this field, it is common to hear investigators state that *in-vitro* performance of nanoparticles does not represent *in-vivo* and clinical performance. *In-vitro* approaches for identifying the uptake or distribution of NPs in 2D models are not the actual comparable representation of the *in-vivo* patient tumor scenario[27]. The direct exposure of the NPs to the cancer cells in the monolayer model does not express how the cancer cells interact with the NPs when they are in the tissue model. The cells in the 2D monolayer model differ in many ways from those in the 3D model, such as drug susceptibility, apoptosis, survival, gene expression, protein expression, and differentiation[28]. Therefore, we aimed to compare the 2D and 3D models when incubated with liposome NPs and identify the uptake difference. We showed in our flow cytometry results that the PEGylated-PI liposomes had significantly greater uptake in the 2D monolayer model compared to both 3D mono-culture and co-culture spheroids models. This data suggests that the 2D

monolayers do not capture the physiological and architectural barriers and provide a mechanistic understanding of liposome NPs uptake as in 3D and *in-vivo* models.

As the 3D models better represent solid tumors than the 2D models, there have been different systems to optimize proper 3D models, such as organoids and spheroids. Organoids are an *in-vitro* model that can be derived from embryonic or adult stem cells (SCs). They are featured by having multiple cell lineages and the ability to recapitulate organ physiological parameters. Spheroids are an *in-vitro* model that can be derived from a mono-culture cell line, multicellular mixtures, primary cells, tumor cells, and tissues. The 3D spheroids can represent single or partial tissue components and transiently resemble cell organization[29]. Although organoids are derived from patients and are most clinically relevant, their heterogeneity limits our ability to control factors and identify specific determinants of drug delivery. Alternatively, spheroids are a flexible system that allows us to make spheroids rapidly in different configurations, such as monoculture and co-culture, which permits us to evaluate each of the TME factors and determine their influence on the delivery systems. Furthermore, the impact of different extracellular matrices (described below) can also be easily examined using more homogenous 3D spheroid systems. Therefore, we used a spheroid system instead of the organoids in our study, and we successfully developed mono-culture and co-culture models that permitted us to identify the effect of CAFs on the uptake of our delivery systems.

The literature provides many methods to develop a 3D spheroid model. One of the primary elements is choosing the base membrane in which the spheroids will be formed. For example, there are hydrogel-based (soft) 3D and solid 3D scaffolds. The solid scaffolds include metal, ceramics, glass, and polymers. However, since the solid scaffolds

have some drawbacks that limit our end goal of the study, such as difficulty in recovering cells from the matrix and limited scope for cell imaging, we did not consider them as a choice. The soft 3D scaffolds involve components derived from hydrogels, such as Corning Matrigel® matrix (low concentration), collagen, hyaluronic acid, *etc.* The reason for using a hydrogel-based membrane is its highly porous and hydrated nature that resembles the physiology of different cell types and allows the application of different tumorigenicity and drug development studies. Matthias Nees et al. compared Matrigel® matrix and collagen to identify the 3D spheroids formation and growth in PC-3 cells. They showed that the collagen spheroids formed loose aggregates and poor cell-to-cell contact, whereas the Matrigel showed a greater ability to support solid tumor growth and differentiation of PC-3 cells in the spheroids. Therefore, we used in our study the Matrigel matrix as a base for our spheroids, and it provided suitable cell-to-cell contact and aggregation. After choosing the spheroids' base membrane, we looked for the method to form the spheroids. There are a variety of methods for forming the spheroids, such as pellet culture (which requires centrifugation that might cause shear stress that can damage the cells), hanging drop (commonly used, but physical parameters such as drop volume and suspension density can affect the size of the spheroids), liquid overlay (static suspension is a simple technique that uses coated surfaces to prevent the cell adhesion to the surface to allow the cells to form spheroids spontaneously, and it provides heterogeneous spheroids in size and shape), and spinner culture(many physical parameters, such as high or low speed of stirring that can affect the spheroids). Hence, we chose the liquid overlay technique that provided a quick spheroids formation (overnight) and allowed us to easily monitor the spheroids' growth since we used 96-well plates.

Many recent studies that used fibroblasts in the co-culture spheroids used foreskin fibroblast[30–32]. The question is, are all fibroblasts the same? Eric G. Neilson, et. al., explained how the origin of the fibroblasts contributes to heterogeneous functions in various organs. They also clarified that the fibroblasts could be better characterized based on their mesenchymal state, which involves different molecular marker profiles[33]. Thus, we ensured using fibroblasts in our study that originated from the same organ (bone marrow) as the cancer cells. It should be noted that PC-3 were prostate cancer cells that had metastasized and were isolated from bone.

To more accurately mimic the TME, a goal of this study was to convert normal bone fibroblasts into cancer-associated fibroblasts (CAFs). In the human body, CAFs are believed to originate from local fibroblasts that are in proximity to cancer cells within a solid tumor[34]. Although different methods of generating CAF are described in the literature, such as using growth factors or microRNAs (miRNAs) to activate fibroblast conversion[35], we followed a methods that involved exposing normal fibroblasts to a culture conditioned media (CCM) that had been incubated with the cancer cells. CCM is obtained by incubating serum-free media with the cancer cells for 24 h. Media is collected after 24 h, centrifuged for 10 min at 1,000 rcf, and passed through a 0.22 μm filter to eliminate debris. Then, FBS was added at 10% (v/v), and CCM was ready to be used in culture. CCM principle collects secreted proteins, including hormones, cytokines, enzymes, growth factors, and other soluble mediators, from cancer cells. These proteins are essential in cell differentiation, growth, invasion, *etc.*[36]. To our knowledge, this method represents the activation of fibroblasts to be CAFs. Brian S. Cummings, et. al., used the same fibroblasts cells (HS-5) and cancer cells (PC-3) we used in our study, and

they followed the CCM to convert the fibroblasts into CAFs[37]. The Cummings's paper followed Yoshiki Sugimura, et. al., study that demonstrated the time required for the fibroblasts to convert into CAFs, which is as they suggested 3 days of incubation with the CCM[38]. In our study, we cultured the fibroblasts with the CCM for more than a month before starting our experiments to ensure their conversion into CAFs.

The growth change in our 3D models was investigated to identify the effect of the CAFs cells introduced to the PC-3 cells. Using the confocal imaging, we noticed that 3D mono-culture spheroids grew faster than the co-culture spheroids. We wanted to understand this growth difference further and, by using flow cytometry, observed that the EpCAM +ve populations (PC-3 cells) started to reduce after day 4 of the co-culture. The EpCAM –ve population was increasing, on the other hand. Hence, we aimed to study the EpCAM –ve populations. CAFs cells are autofluorescent in the FITC channel. This autofluorescence is detected in some cells, which contain different compounds that excite by the 488 nm laser and emit in the FITC channel[39]. After examining the EpCAM –ve populations based on the autofluorescence, we found an increase in the cells with no autofluorescence, suggesting that the PC-3 cells grown in presence of CAF were losing their sensitivity to the EpCAM marker after 4 days of the co-culture. Hyo-Jeong Kuh et al. co-cultured HT-29 (human colorectal cancer) cells with CCD-18Co (normal human colon fibroblasts). They used a ratio of cancer cells to fibroblasts at 1:1.2, and they tracked the immunofluorescence of Ki-67 (a protein associated with cellular proliferation highly expressed by the HT-29 cells) and fibronectin (an ECM glycoprotein that is expressed by both HT-29 and CCD-18Co cells). This study showed that the fibronectin expression was significantly greater in the co-culture spheroids compared to the mono-

culture spheroids; however, the Ki-67 expression was significantly lower in the co-culture spheroids compared to the mono-culture spheroids. They hypothesized the reason behind the reduction of the cellular proliferation marker was the epithelial-mesenchymal transition (EMT). Accordingly, we have collected samples from our co-culture spheroids to run an RNA-seq to identify EMT markers and other gene expression changes.

Drug development for aggressive and/or lethal treatment-resistant PCa poses a significant challenge with very few therapeutic successes[40,41]. Notably, we used bulk RNAseq in 2D mCRPC (PC-3) cell line model and as well as 3D mCRPC (PC-3) mono-culture spheroid as an innovative approach to demonstrate that signatures of EMT, MMPs, cancer hallmark genes, and cancer 'stemness' are major key pathways to developing metastatic aggressive PCa, including castration-resistant and taxane-resistant tumors. Further, we identified a plenty of "stem-like" cell population (EpCAM-ve) in aggressive metastatic PCa (PC-3) 2D and 3D cell line model by using a flow cytometry study, which was supported by RNAseq over-expression of several EMT markers, including VIM, HAS3, S100A6, ANXA2P2, ANXA2, ANXA3, AHNAK2, LOXL2, TGFB1, TGFBR2, UCHL1, CD44, CD55, CD109. Moreover, our 3D co-culture (PC-3 + CAFs) spheroids model showed that the EpCAM expression started reducing after 4 days of the co-culture. Therefore, it is essential to extend this study, in the future, with comprehensive RNAseq analysis for 3D co-culture (PC-3 + CAFs) spheroids and identify and validate key gene signatures for PCa aggressiveness.

Importantly, we identified HAS3 as one of the top EMT markers for aggressive PCa. Hyaluronan (HA) is an essential constituent of the stem cell niche. High expression of HAS3 (2.78-fold upregulation in the 3D co-culture compared to the 2D culture) secretes

large amounts of HA and is bound to CD44 (CD44 is the major HA receptor) “stem-like” cells population and plays a critical role development CSCs by regulating cell adhesion, migration, proliferation, differentiation, cancer metastasis and multidrug-resistant[42,43]. Further, previous studies have reported that CD44 expression is greater in PCa and involved in cancer cell proliferation, invasion, migration, and drug resistance[44]. Moreover, few studies also mentioned that CD44 played a vital role in cancer stemness in PCa[45,46]. We observed in our study using flow cytometry that CD44 is highly expressed (98.4%) in 2D mCRPC (PC-3) cell lines. In the future, our lab proposes to perform a flow cytometry study of 3D mono-culture (PC-3) and co-culture (PC-3 + CAFs) with the CD44 cell population to evaluate and validate its role in PCa aggressiveness.

Further, CD55 is also known to promote PCa cell survival and metastatic spread[47,48]. CD109 is another new marker for invasive prostate carcinoma[49]. Our RNAseq data reported elevated expression of CD55 and CD109 (1.13 and 1.13-fold upregulation, respectively) in aggressive mCRPC/NEPC PCa (PC-3) 3D mono-culture after 7 days of growth compared to day 0. Recent studies identified FSCN1 as taxane-resistant markers in other solid tumors, including PCa[50,51]. We identified FSCN1 as a key upregulated gene (2.51-fold) for taxane-resistance in aggressive PCa (PC-3) mCRPC/NEPC 3D mono-culture compared to 2D culture. Resistant cancers are common; however, models that represent those types of cancers are limited, and they are needed to better predict drug resistant.

Since our goal was to identify *in-vitro* model systems (2D and 3D-tumor models) that better represent *in vivo* tumor and TME, further preclinical validation and single-cell multi-omics strategies using xenograft models and patient-derived organoids are

necessary for future studies. Further, this will allow the understanding of sub-clonal molecular pathways underlying differential patterns of PCa aggressiveness and drug response among various PCa subtypes.

4.2 Future Directions

The growth and development of nanoparticles and nanotechnology is expanding rapidly. However, challenges have limited a substantial number of novel particles from going into the market, based on lack of successful clinical trials of nanoparticles formulations described in clinicaltrials.gov. One of these reasons is the inability of classical *in vitro* models to study the performance and efficacy of NPs. Applying a newer models such as the 3D mono-culture and co-culture spheroids, that better mimic tumor complexity and TME we believe can improve the development and optimization of the NPs. A targeted delivery system is one of the future goals that our lab is pursuing and progressing to develop. For all that, RNAseq and Single-cell RNAseq (scRNAseq) are necessary to identify gene expression signatures at the sub-clonal level. Further, Flow cytometry studies in the future will validate EMT markers, CD44, CD133, and both. All in all, the goal is to identify gene(s) that can be utilized as a targeted marker to increase the efficacy and lower the toxicity of the NP's delivery system. Knockout experiments can examine the targeted gene to evaluate its role in the NPs delivery system and the PCa development and aggressiveness.

There are many types of NPs, and every type owns advantages and disadvantages; nevertheless, the literature showed that much research was toward combing two NPs aiming to use each of these NPs' advantages to provide better outcomes. Hyde Vergara

et al. developed a genistein-PEGylated silica nanocomposite system to enhance the antioxidant and antiproliferative properties of human colon cancer cells[52]. Applying this kind of particles to a 3D multicellular model, for example, would bring higher knowledge about these particles' interactions with cancer cells.

Our study's 3D co-culture spheroids model had a 1:1 ratio (PC-3 to CAFs cells). Future studies will investigate different ratios and how that would affect the NPs uptake or distribution. Hossein Tavana, et. al., co-cultured breast cancer cells with fibroblast cells and used different ratios; however, they have not seen any growth difference between all ratios[53]. Fibroblasts are not from a single origin which makes them express different markers, secrete different proteins, and provide different interactions with the cancer cells[33]. Hence, future directions will identify how different ratios affect the gene expressions in cancer cells. Further, studies that take normal fibroblasts and determine their ability to form CAF when co-encapsulated with PC-3 and other prostate cancer cells is needed. The interplay between fibroblasts and different tumors may provide insights into the sensitivity and failure of existing therapies.

Finally, for future studies, preclinical validation and single-cell multi-omics strategies that include other cells (e.g., macrophages and tumor endothelial cells), or patient-derived organoids (PDO) and patient derived xenografts (PDX) are necessary. Based on data obtained in controlled spheroid studies can be used to identify specific markers that can be identified in more diverse patient derived samples.

4.3 Conclusion

To study the uptake or distribution of LNPs, we used a non-toxic fluorescent dye that can be entrapped in the LNPs through exposure to the cells. Rather than using existing drugs and liposome markers we wanted to locate liposomes without killing the cells to understand if they get uptake into the cells as intact particles or if they degrade out of the cells and release the drug to be uptake by the cells. Previously the lab has used doxorubicin (Dox) in the LNPs[3]. However, that could not explain if the particles degraded or uptake as intact particles because released and liposome-encapsulated doxorubicin were known to be taken up and kill cells. We aimed to test the live cell populations with an intact cell membrane. Fortunately, we found a suitable fluorescent dye that can be used with a specific concentration that is not toxic to the cells and cannot cross intact cell membranes, which is propidium iodide (PI). PI is a known fluorescent dye that has been well established as it cannot cross intact cell membranes (live cells) but only interrupted cell membranes (dead cells) and bind double-stranded DNA[54]. It should be noted that the lab had also examined fluorescent membrane markers often described as non-exchangeable, such as DiO, DiD, and DiR, however, incubation studies found similar issues associated with non-specific uptake and marking of tumor membranes.

Nevertheless, we identified that the PI crosses the intact cell membranes when incubated for over six hours with the cells. We also found that the PI uptake is time and concentration-dependent. Thus, we considered the PI uptake a positive control, and we excluded the dead cells using Calcein AM (live cells) and Ghost Dye (dead cells). We successfully entrapped the PI by the passive aqueous capture method[55]. While the overall encapsulation efficiency was low (8.3±2.42%), but it showed remarkable stability in

biological conditions until 72 h, and the limited release (maximum, ~15%) was below the limit for detecting uptake.

The liposome nanoparticles (LNPs) we used in our study were based on well-established, clinically used formulations that have been published in the literature[1]. We used a variety of assays to characterize the formulations and confirm their stability and reproducibility. One of the significant differences between the formulations was the zeta potential. Zeta potential is a physical property that measures the potential stability of a colloidal system, where the large positive or negative indicates increased repelling interaction between particles and provides a stable system[56]. As expected, the PEGylated liposomes showed a more negative zeta potential of -28±2 mV compared to the conventional liposomes, 20±2 mV. Following the stability experiments we ran in biological conditions for 72 h, the zeta potential decreased to -19.4±2 mV for the PEGylated liposomes and shifted negative (-4.5±2.6 mV) for the conventional liposomes. The conventional liposomes charge (electrophoretic mobility) also switched from 1.5±0.15 μmcm/Vs into -0.3±0.25 μmcm/Vs after the stability experiment, where the PEGylated liposomes were considered stable (-2±0.15 μmcm/Vs and -1.5±0.2 μmcm/Vs after the experiment). Consequently, we recognized that the size distributions had changed too after the experiment. The conventional liposome size distribution increased by 22%, whereas the PEGylated liposome size distribution increased by only 0.6%. Thus, we identified that the anionic PEG played an important role in increasing the zeta potential parameter and the particles' stability.

Recent studies have demonstrated the importance of CAFs in tumor growth and response to drugs and nanomedicines. CAFs are responsible for modulating a number of

TME factors such as collagen, fibronectin, and proteoglycan, which play an essential role in hindering the penetration of the NPs and treatment within solid tumors[57]. Our 3D co-culture model showed lower LNPs and free dye uptake than the 2D monolayer culture and the 3D mono-culture models, and this finding complements literature findings[58]. However, TME is not only CAFs but also many other stromal cells, ECM, proteins, enzymes, chemokines…etc., which create a complex system to promote tumor growth, spread, and resistance. Many literature publications have used simple models such as 2D monolayer culture, tested the drug delivery efficacy, and then moved into very complex models such as the *in-vivo* mice model[59,60]. There are many factors, such as TME stromal cells and other factors involve in *in-vivo* models, which they contribute to lower delivery systems distribution and uptake into the cancer cells; therefore, current and future directions will determine these factors influence over the delivery systems and treatment efficacy.

Our results showed that the older (day 7) spheroids provide higher uptake chances than the younger (day 2) spheroids. Danijela Matic Vignjevic, et. al., showed that when CAFs were co-cultured with colon cancer cells, CAFs induced cancer cell invasion by breaching the matrix, making the cancer cells ready to travel and more accessible for the treatment[61]. Normal and cancer-associated fibroblasts are known for matrix remodeling, explaining the higher uptake in older spheroids. The spatial and temporal roles need to be further examined.

Moreover, our results showed that co-culturing only CAFs into the PC-3 cells (1:1) in spheroids made the growth slower than the 3D mono-culture with only PC-3 cells. We believe this is more realistic and better mimics actual tumor growth, but this finding

contradicts most literature claims. Guillauma Vogin, et. al., showed that adding the CAFs into human mammary adenocarcinoma cells (MCF-7) in the same ratio (1:1) we used in our experiments made the growth higher than the 3D mono-culture with only MCF-7 cells. However, there are many variables to consider, such as the origin of the fibroblasts they used (human embryonic fibroblasts (MRC-5)), normal or cancer-associated fibroblasts, and the stage of cancer cells used in the model (adenocarcinoma metastasis), and many others[24]. We used fibroblasts cells (HS-5) from the exact origin (bone marrow) that the cancer cells (PC-3) were collected from, we also converted the fibroblasts into cancer-associated fibroblasts before the co-culture was initiated, and the PC-3 cells are highly aggressive and neuroendocrine differentiated. Another study by Chuanqing Bao, et. al., concurs with our findings. It indicates that CAFs secrete circEIF3K exosomes that cause reduce in colorectal cancer cells proliferation *in-vitro* and *in-vivo*[62]. Therefore, tumors and their environments are different in each cancer type and stage, and how they grow and develop is unpredictable.

One of the findings of our results is that we noticed the PC-3 lose their sensitivity significantly to the EpCAM antibody when they are co-cultured with the CAFs after four days. Therefore, we have studied the populations that were not stained with EpCAM after four days and further, and we noticed that some of the PC-3 cells were there with the CAFs cells. This could indicate epithelial-mesenchymal transition (EMT). C.P. Hu et al. showed that CAFs induced EMT in lung cancer cells[63]. Accordingly, this is one of the future directions to study the EMT caused by CAFs when co-culture with cancer cells.

RNAseq is an innovative approach that demonstrates gene expression differences by comparing 2D culture (PC-3) with 3D mono-culture (PC-3) and comparing 0 days, 3

days, and 7 days of 3D mono-culture. EMT, MMPs, cancer hallmark genes, and cancer 'stemness' are major key pathways to developing metastatic aggressive PCa. RNAseq over-expression of several EMT markers, including VIM, HAS3, S100A6, ANXA2P2, ANXA2, ANXA3, AHNAK2, LOXL2, TGFB1, TGFBR2, UCHL1, CD44, CD55, CD109.

In conclusion, we developed a 3D multicellular co-culture platform that allowed us to examine the impact of the CAFs cells on the performance of the LNPs, and that platform showed lower uptake of the LNPs compared to the 3D mono-cellular platform. Moreover, we identified the gene expression difference between the 2D and 3D models, and demonstrated that genes associated with EMT and resistance were increase in 3D and co-culture systems. This study broadens our understanding of the TME effect on the cancer cells and over the delivery system, and this allows us to gain additional mechanistic insights.

4.4 References:

1. Zhu G, Mock JN, Aljuffali I, Cummings BS, Arnold RD. Secretory phospholipase A_2 responsive liposomes. *J Pharm Sci*. 2011;100(8):3146-3159. doi:10.1002/jps.22530
2. Crowley LC, Scott AP, Marfell BJ, Boughaba JA, Chojnowski G, Waterhouse NJ. Measuring Cell Death by Propidium Iodide Uptake and Flow Cytometry. *Cold Spring Harb Protoc*. 2016;2016(7). doi:10.1101/pdb.prot087163
3. Mock JN, Costyn LJ, Wilding SL, Arnold RD, Cummings BS. Evidence for distinct mechanisms of uptake and antitumor activity of secretory phospholipase A_2 responsive liposome in prostate cancer. *Integr Biol*. 2013;5(1):172-182. doi:10.1039/C2IB20108A
4. Webb C, Khadke S, Schmidt ST, et al. The Impact of Solvent Selection: Strategies to Guide the Manufacturing of Liposomes Using Microfluidics. *Pharmaceutics*. 2019;11(12). doi:10.3390/pharmaceutics11120653
5. Henriksen I, Sande SA, Smistad G, Ågren T, Karlsen J. In vitro evaluation of drug release kinetics from liposomes by fractional dialysis. *Int J Pharm*. 1995;119(2):231-238. doi:10.1016/0378-5173(94)00403-R
6. Yang NJ, Hinner MJ. Getting across the cell membrane: an overview for small molecules, peptides, and proteins. *Methods Mol Biol*. 2015;1266:29-53. doi:10.1007/978-1-4939-2272-7_3
7. Ohue K, Ohtake K. Malvern Zetasizer ZS DLS user manual. *Electron Commun Japan (Part I Commun*. 1984;67(5):37-46.
8. Raval N, Maheshwari R, Kalyane D, Youngren-Ortiz SR, Chougule MB, Tekade

RK. Chapter 10 - Importance of Physicochemical Characterization of Nanoparticles in Pharmaceutical Product Development. In: Tekade RKBT-BF of DD, ed. *Advances in Pharmaceutical Product Development and Research*. Academic Press; 2019:369-400. doi:https://doi.org/10.1016/B978-0-12-817909-3.00010-8

9. Lu GW, Gao P. CHAPTER 3 - Emulsions and Microemulsions for Topical and Transdermal Drug Delivery. In: Kulkarni VSBT-H of N-IDDS, ed. *Personal Care & Cosmetic Technology*. Boston: William Andrew Publishing; 2010:59-94. doi:https://doi.org/10.1016/B978-0-8155-2025-2.10003-4
10. Zaichik S, Steinbring C, Jelkmann M, Bernkop-Schnürch A. Zeta potential changing nanoemulsions: Impact of PEG-corona on phosphate cleavage. *Int J Pharm*. 2020;581:119299. doi:10.1016/j.ijpharm.2020.119299
11. Tiselius A. Capillary Electrophoresis Capillary Electrophoresis Electrophoretic Mobility. 1960:1-7.
12. Wu T, Dai Y. Tumor microenvironment and therapeutic response. *Cancer Lett*. 2017;387:61-68. doi:10.1016/j.canlet.2016.01.043
13. Li H, Fan X, Houghton JM. Tumor microenvironment: The role of the tumor stroma in cancer. *J Cell Biochem*. 2007;101(4):805-815. doi:10.1002/jcb.21159
14. Brizzi MF, Tarone G, Defilippi P. Extracellular matrix, integrins, and growth factors as tailors of the stem cell niche. *Curr Opin Cell Biol*. 2012;24(5):645-651. doi:10.1016/j.ceb.2012.07.001
15. Sahai E, Astsaturov I, Cukierman E, et al. A framework for advancing our understanding of cancer-associated fibroblasts. *Nat Rev Cancer*. 2020;20(3):174-

186. doi:10.1038/s41568-019-0238-1

16. Von Ahrens D, Bhagat TD, Nagrath D, Maitra A, Verma A. The role of stromal cancer-associated fibroblasts in pancreatic cancer. *J Hematol Oncol*. 2017;10(1):1-8. doi:10.1186/s13045-017-0448-5

17. McKinnon KM. Flow Cytometry: An Overview. *Curr Protoc Immunol*. 2018;120:5.1.1-5.1.11. doi:10.1002/cpim.40

18. An Y, Liu F, Chen Y, Yang Q. Crosstalk between cancer-associated fibroblasts and immune cells in cancer. *J Cell Mol Med*. 2020;24(1):13-24. doi:10.1111/jcmm.14745

19. Buchwalow I, Samoilova V, Boecker W, Tiemann M. Non-specific binding of antibodies in immunohistochemistry: fallacies and facts. *Sci Rep*. 2011;1(1):28. doi:10.1038/srep00028

20. Canals Hernaez D, Hughes MR, Li Y, et al. Targeting a Tumor-Specific Epitope on Podocalyxin Increases Survival in Human Tumor Preclinical Models. *Front Oncol*. 2022;12(May):1-14. doi:10.3389/fonc.2022.856424

21. Lau EYT, Lo J, Cheng BYL, et al. Cancer-Associated Fibroblasts Regulate Tumor-Initiating Cell Plasticity in Hepatocellular Carcinoma through c-Met/FRA1/HEY1 Signaling. *Cell Rep*. 2016;15(6):1175-1189. doi:10.1016/j.celrep.2016.04.019

22. Draffin JE, McFarlane S, Hill A, Johnston PG, Waugh DJJ. CD44 potentiates the adherence of metastatic prostate and breast cancer cells to bone marrow endothelial cells. *Cancer Res*. 2004;64(16):5702-5711. doi:10.1158/0008-5472.CAN-04-0389

23. Sheng X, Li Z, Wang DL, et al. Isolation and enrichment of PC-3 prostate cancer stem-like cells using MACS and serum-free medium. *Oncol Lett*. 2013;5(3):787-792. doi:10.3892/ol.2012.1090

24. Yakavets I, Francois A, Benoit A, Merlin JL, Bezdetnaya L, Vogin G. Advanced co-culture 3D breast cancer model for investigation of fibrosis induced by external stimuli: optimization study. *Sci Rep*. 2020;10(1):1-11. doi:10.1038/s41598-020-78087-7

25. Jeong S, Lee J, Shin Y, Chung S, Kuh H. Co-Culture of Tumor Spheroids and Fibroblasts in a Collagen Matrix-Incorporated Microfluidic Chip Mimics Reciprocal Activation in Solid Tumor Microenvironment. 2016:1-17. doi:10.1371/journal.pone.0159013

26. Yakavets I, Jenard S, Francois A, et al. Stroma-rich co-culture multicellular tumor spheroids as a tool for photoactive drugs screening. *J Clin Med*. 2019;8(10):1-19. doi:10.3390/jcm8101686

27. Su T, Yang B, Gao T, Liu T, Li J. Polymer nanoparticle-assisted chemotherapy of pancreatic cancer. *Ther Adv Med Oncol*. 2020;12:1-33. doi:10.1177/1758835920915978

28. Ravi M, Paramesh V, Kaviya SR, Anuradha E, Paul Solomon FD. 3D cell culture systems: Advantages and applications. *J Cell Physiol*. 2015;230(1):16-26. doi:10.1002/jcp.24683

29. Gunti S, Hoke ATK, Vu KP, London NR. Organoid and spheroid tumor models: Techniques and applications. *Cancers (Basel)*. 2021;13(4):1-18. doi:10.3390/cancers13040874

30. Tsai CW, Wang JH, Young TH. Core/shell multicellular spheroids on chitosan as in vitro 3D coculture tumor models. *Artif Cells, Nanomedicine Biotechnol*. 2018;46(sup3):S651-S660. doi:10.1080/21691401.2018.1505744

31. Rustamov V, Keller F, Klicks J, Hafner M, Rudolf R. Bone sialoprotein shows enhanced expression in early, high- proliferation stages of three-dimensional spheroid cell cultures of breast cancer cell line MDA-MB-231. *Front Oncol*. 2019;9(FEB). doi:10.3389/fonc.2019.00036

32. Henrique RBL, Lima RRM, Monteiro CAP, et al. Advances in the study of spheroids as versatile models to evaluate biological interactions of inorganic nanoparticles. *Life Sci*. 2022;302(March):120657. doi:10.1016/j.lfs.2022.120657

33. LeBleu VS, Neilson EG. Origin and functional heterogeneity of fibroblasts. *FASEB J*. 2020;34(3):3519-3536. doi:10.1096/fj.201903188R

34. Öhlund D, Handly-Santana A, Biffi G, et al. Distinct populations of inflammatory fibroblasts and myofibroblasts in pancreatic cancer. *J Exp Med*. 2017;214(3):579-596. doi:10.1084/jem.20162024

35. Shen H, Yu X, Yang F, et al. Reprogramming of Normal Fibroblasts into Cancer-Associated Fibroblasts by miRNAs-Mediated CCL2/VEGFA Signaling. *PLoS Genet*. 2016;12(8):1-20. doi:10.1371/journal.pgen.1006244

36. Dowling P, Clynes M. Conditioned media from cell lines: a complementary model to clinical specimens for the discovery of disease-specific biomarkers. *Proteomics*. 2011;11(4):794-804. doi:10.1002/pmic.201000530

37. Kaur SP, Verma A, Lee HK, Barnett LM, Somanath PR, Cummings BS. Inhibition of glypican-1 expression induces an activated fibroblast phenotype in a human

bone marrow-derived stromal cell-line. *Sci Rep*. 2021;11(1):1-14. doi:10.1038/s41598-021-88519-7

38. Ishii K, Mizokami A, Tsunoda T, et al. Heterogenous induction of carcinoma-associated fibroblast-like differentiation in normal human prostatic fibroblasts by co-culturing with prostate cancer cells. *J Cell Biochem*. 2011;112(12):3604-3611. doi:10.1002/jcb.23291

39. Mosiman VL, Patterson BK, Canterero L, Goolsby CL. Reducing cellular autofluorescence in flow cytometry: An in situ method. *Commun Clin Cytom*. 1997;30(3):151-156. doi:10.1002/(SICI)1097-0320(19970615)30:3<151::AID-CYTO6>3.0.CO;2-O

40. Scher HI, Solo K, Valant J, Todd MB, Mehra M. Prevalence of Prostate Cancer Clinical States and Mortality in the United States: Estimates Using a Dynamic Progression Model. *PLoS One*. 2015;10(10):e0139440. doi:10.1371/journal.pone.0139440

41. Wang Y, Chen J, Wu Z, et al. Mechanisms of enzalutamide resistance in castration-resistant prostate cancer and therapeutic strategies to overcome it. *Br J Pharmacol*. 2021;178(2):239-261. doi:10.1111/bph.15300

42. Qu C, Rilla K, Tammi R, Tammi M, Kröger H, Lammi MJ. Extensive CD44-dependent hyaluronan coats on human bone marrow-derived mesenchymal stem cells produced by hyaluronan synthases HAS1, HAS2 and HAS3. *Int J Biochem Cell Biol*. 2014;48:45-54. doi:10.1016/j.biocel.2013.12.016

43. Chanmee T, Ontong P, Kimata K, Itano N. Key Roles of Hyaluronan and Its CD44 Receptor in the Stemness and Survival of Cancer Stem Cells. *Front Oncol*.

2015;5:180. doi:10.3389/fonc.2015.00180

44. Li W, Qian L, Lin J, et al. CD44 regulates prostate cancer proliferation, invasion and migration via PDK1 and PFKFB4. *Oncotarget*. 2017;8(39):65143-65151. doi:10.18632/oncotarget.17821

45. Palapattu GS, Wu C, Silvers CR, et al. Selective expression of CD44, a putative prostate cancer stem cell marker, in neuroendocrine tumor cells of human prostate cancer. *Prostate*. 2009;69(7):787-798. doi:10.1002/pros.20928

46. Stefano C Di, Grazioli P, Fontanella RA, et al. Stem-like and highly invasive prostate cancer cells expressing CD44v8-10 marker originate from CD44-negative cells. *Oncotarget*. 2018;9(56):30905-30918. doi:10.18632/oncotarget.25773

47. Loberg RD, Day LL, Dunn R, Kalikin LM, Pienta KJ. Inhibition of decay-accelerating factor (CD55) attenuates prostate cancer growth and survival in vivo. *Neoplasia*. 2006;8(1):69-78. doi:10.1593/neo.05679

48. Loberg RD, Wojno KJ, Day LL, Pienta KJ. Analysis of membrane-bound complement regulatory proteins in prostate cancer. *Urology*. 2005;66(6):1321-1326. doi:10.1016/j.urology.2005.06.094

49. Mo XT, Leung THY, Tang HWM, et al. CD109 mediates tumorigenicity and cancer aggressiveness via regulation of EGFR and STAT3 signalling in cervical squamous cell carcinoma. *Br J Cancer*. 2020;123(5):833-843. doi:10.1038/s41416-020-0922-7

50. Xiao Z-S, Zhao L, Zhang X-N, Li H-X, Yin Z-H. Effect of rs67085638 in long non-coding RNA (CCAT1) on colon cancer chemoresistance to paclitaxel through modulating the microRNA-24-3p and FSCN1. *J Cell Mol Med*. 2021;25(8):3744-

3753. doi:10.1111/jcmm.16210

51. Pan Y, Chen J, Tao L, et al. Long noncoding RNA ROR regulates chemoresistance in docetaxel-resistant lung adenocarcinoma cells via epithelial mesenchymal transition pathway. *Oncotarget*. 2017;8(20):33144-33158. doi:10.18632/oncotarget.16562

52. Pool H, Campos-Vega R, Herrera-Hernández MG, et al. Development of genistein-PEGylated silica hybrid nanomaterials with enhanced antioxidant and antiproliferative properties on HT29 human colon cancer cells. *Am J Transl Res*. 2018;10(8):2306-2323.

53. Ham SL, Thakuri PS, Plaster M, et al. Three-dimensional tumor model mimics stromal - breast cancer cells signaling. *Oncotarget*. 2018;9(1):249-267. doi:10.18632/oncotarget.22922

54. Nicoletti I, Migliorati G, Pagliacci MC, Grignani F, Riccardi C. A rapid and simple method for measuring thymocyte apoptosis by propidium iodide staining and flow cytometry. *J Immunol Methods*. 1991;139(2):271-279. doi:10.1016/0022-1759(91)90198-O

55. Maja L, Željko K, Mateja P. Sustainable technologies for liposome preparation. *J Supercrit Fluids*. 2020;165. doi:10.1016/j.supflu.2020.104984

56. Limited MI. Zeta potential: An Introduction in 30 minutes. *Zetasizer Nano Serles Tech Note MRK654-01*. 2011;2:1-6. http://scholar.google.com/scholar?hl=en&btnG=Search&q=intitle:Zeta+Potential+An+Introduction+in+30+Minutes#0.

57. Guo J, Zeng H, Shi X, et al. A CFH peptide-decorated liposomal oxymatrine

inactivates cancer-associated fibroblasts of hepatocellular carcinoma through epithelial–mesenchymal transition reversion. *J Nanobiotechnology*. 2022;20(1):1-19. doi:10.1186/s12951-022-01311-1

58. Junttila MR, De Sauvage FJ. Influence of tumour micro-environment heterogeneity on therapeutic response. *Nature*. 2013;501(7467):346-354. doi:10.1038/nature12626

59. Ghaferi M, Asadollahzadeh MJ, Akbarzadeh A, Ebrahimi Shahmabadi H, Alavi SE. Enhanced Efficacy of PEGylated Liposomal Cisplatin: In Vitro and In Vivo Evaluation. *Int J Mol Sci*. 2020;21(2). doi:10.3390/ijms21020559

60. Mirzavi F, Barati M, Vakili-Ghartavol R, et al. Pegylated liposomal encapsulation improves the antitumor efficacy of combretastatin A4 in murine 4T1 triple-negative breast cancer model. *Int J Pharm*. 2022;613(December 2021):121396. doi:10.1016/j.ijpharm.2021.121396

61. Glentis A, Oertle P, Mariani P, et al. Cancer-associated fibroblasts induce metalloprotease-independent cancer cell invasion of the basement membrane. *Nat Commun*. 2017;8(1):1-13. doi:10.1038/s41467-017-00985-8

62. Yang K, Zhang J, Bao C. Exosomal circEIF3K from cancer-associated fibroblast promotes colorectal cancer (CRC) progression via miR-214/PD-L1 axis. *BMC Cancer*. 2021;21(1):1-9. doi:10.1186/s12885-021-08669-9

63. You J, Li M, Cao LM, et al. Snail1-dependent cancer-associated fibroblasts induce epithelial-mesenchymal transition in lung cancer cells via exosomes. *Qjm*. 2019;112(8):581-590. doi:10.1093/qjmed/hcz093